Network-level Pavement Evaluation Utilizing Traffic Speed Deflectometer

A Dissertation Presented for the
Doctor of Philosophy
Degree
The University of Tennessee, Knoxville

Miaomiao Zhang
December 2022

DEDICATION

To Yuanchang Zhang, my father, for his endless love, support and encouragement even from Heaven.

ACKNOWLEDGEMENTS

First and foremost, I am in debt to my advisor, Dr. Baoshan Huang, for his motivation and guidance in helping me complete this dissertation. Without his leadership and patience, this study could not be finished.

Special thanks go to my committee members, Dr. Timothy Truster, Dr. Shuai Li, and Dr. Xiaoyang Jia, whose perceptive advice and constructive criticism are helpful during the doctoral study.

Many thanks are due to my colleagues for their friendship, Yuetan Ma, Xi Jiang, Rui Xiao, Pawel Polazyk, Jingtao Zhong, and Guantao Cheng. I am especially grateful to Dr. Yongchao Xie for his editorial suggestions in refining my papers.

Last, I would like to thank my family for their great support. Dad, I miss you so much.

ABSTRACT

The Traffic Speed Deflectometer (TSD) overcomes the Falling Weight Deflectometer (FWD) limitations in terms of traffic interruption and testing inefficiency, which has been used for network-level pavement structural evaluation. However, some challenges exist as applying the TSD for routine survey works. This study proposed an effective temperature correction method to achieve the speed and temperature correction of TSD deflections simultaneously based on the time-temperature superposition principle. To match the existing FWD-based pavement structure number (SN) records, an enhanced AASHTO method was proposed for calibrating TSD-based SN by the asphalt thickness. In addition, this study discussed potential uses of TSD slopes in terms of replacing deflection indices, estimating the inflection point location, and calculating the deflection lag distance. The feasibility of estimating pavement fatigue conditions from TSD lag distance was also evaluated. Finally, this study proposed an autoencoder to extract crack features and performed structure classification based on pavement crack images. Results from the present analyses suggest that TSD deflections are more sensitive to test temperatures than to test speeds. For normal TSD operating speeds, a 10 mph increase in test speed is approximately equivalent to a 1°C drop in temperature. The difference in AASHTO SN between TSD and FWD essentially came from the difference in the equivalent loading frequency, and the asphalt layer exhibited lower stiffness under TSD than under FWD. The lag distance can be used as an implicit indicator of the fatigue condition of the pavement to predict the initiation and growth of fatigue cracks. Fatigue cracking is expected to occur where the lag distance is relatively large. For crack images with more than 20% cracks, longitudinal cracks on wheel paths play the most important role in the structure classification, and their presence indicates potential pavement structural weakness.

TABLE OF CONTENTS

LIST OF TABLES

LIST OF FIGURES

CHAPTER 1

INTRODUCTION

Traffic Speed Deflectometer

Pavement evaluation is an essential step in assessing the functional and structural conditions of existing pavements, guiding routine data monitoring, and selecting appropriate maintenance measures. The functional conditions are related to pavement distress and driving quality, such as roughness, rut depth, and fatigue cracks. The structural conditions deal with the pavement's ability to withstand traffic loads and climate conditions [1].

The incompleteness of construction history and the resulting inaccurate estimates of pavement structural capacity necessitates the use of innovative techniques to obtain accurate network-level pavement structural data. Traditional methods of estimating the pavement structural strength through layer thickness and laboratory-determined material properties are destructive and costly. Currently, deflection measurements remain the only reliable non-destructive method for determining the structural strength of flexible pavements. The stationary Falling Weight Deflectometer (FWD) is the most prevailing method of deflection measurement. As of 2008, more than 90% of states in the United States routinely conducted FWD testing for pavement assessment [2].

The FWD is a trailer-mounted device that operates by dropping a weight onto the pavement and measures the resulting vertical pavement surface deflections using geophones placed at fixed radial distances (Figure 1-1, all tables and figures are located in the Appendix). FWD has a wide range of applications because it collects various information. For example, the maximum pavement deflection indicates the overall pavement structural capacity [3]. The 1993 AASHTO design guide introduced an approach to estimate pavement structural number (SN) through FWD deflections [4]. In addition, pavement deflections can be used to back-calculate the related layer modulus given the pavement structure [5]. Upon testing, FWD must remain stationary at each test point, so lane closures are required, which interrupts traffic and limits the productivity of FWD. Typical FWD productivity is approximately 20-25 lane miles per day if FWD data are collected every 0.2 miles [6]. Therefore, issues of time, expenses, and traffic control hinder FWD testing at network-level, and FWD is the preferred device for project-level structural evaluation.

Recent technological advancements have led to the development of continuous deflection measurement devices, including the traffic speed deflectometer (TSD), which is capable of performing deflection measurements at traffic speeds [7,8]. Since the first prototype device was developed in Denmark in the late 1990s, TSD has been constantly evolving with new features, but the concept remains the same [9]. As shown in Figure 1-2, TSD uses a set of Doppler lasers mounted on a servo-hydraulic beam near the rear axle (at the centerline of right dual tires) to measure the deflection velocity (horizontal and vertical) of the pavement surface [7]. The horizontal proportion of the deflection velocity is related to the TSD moving speed. To eliminate the dependence on the moving speed, the measured deflection velocity is divided by the instantaneous moving speed to obtain the deflection slope [10]. The deflection slope is the first-order derivative of the deflection, which is converted to actual pavement deflection by curve fitting and numerical integration [11]. The last sensor is located at about 138 inches in front of the rear axle. This laser is located outside the deflection bowl and is primarily used as a reference laser, so its response can be used to eliminate unwanted measurements [12].

TSD can provide better spatial coverage and efficiency than FWD. The findings of a Federal Highway Administration (FHWA) research project confirmed that TSD measurements meet the accuracy requirements for pavement structural assessment at network-level [13]. However, some challenges exist in applying TSD for routine survey works. The accuracy and precision of TSD measurements can be influenced by several internal and external factors. Therefore, there is a need to develop a reliable TSD deflection correction procedure, which may include the load or temperature correction for TSD deflections, so that TSD deflections collected at different trips or under different conditions will be comparable.

Comparison of TSD and FWD

Since TSD is a relatively new device, it is imperative to compare it with the existing measurement devices to validate its applicability and reliability [12]. In addition, the more widely used one (FWD) usually has sufficiently comprehensive and detailed evaluation systems and methods, but the applicability of the new device (TSD) is yet to verify [6]. Simple replications usually lead to discrepancies. Therefore, a detailed comparison of FWD and TSD is required to determine their underlying different mechanisms.

Table 1-1 illustrates the comparison between TSD and FWD. The deflection measuring techniques for FWD and TSD are quite different, and the measured deflection is conceptually different even if the load magnitudes are the same. Since most of the current deflection tests are performed using FWD, FWD is used as a reference device to evaluate the accuracy of TSD. However, given the difference in the pavement responses under TSD and FWD, FWD may not be a true reference. Previous studies have shown that although the deflection of FWD and TSD are different, it is clear from the visual inspection that the two measurements follow the same trend and have the same peak points [12].

Applications of TSD

Many studies have been conducted to improve and expand the application of TSD. These studies were mainly inherited from FWD, such as using TSD deflections to calibrate the FWD-based equations [6,14,15]. Therefore, studies on TSD have mainly focused on the deflection itself and ignored the potentially useful information in the TSD slope. Since the TSD slope is the raw measurement, the intensive use of deflection may accumulate errors caused by curve fitting. The potential use of TSD slope in pavement structural evaluation should be explored.

In addition, the viscoelasticity of the asphalt concrete (AC) and the inertial damping of the pavement structure could result in a lag between the time when the TSD crosses over the point and the time when the maximum response occurs [13]. Figure 1-3(a) shows that there is a lag between the load center and the maximum deflection point in the deflection basin. A similar lag phenomenon between load and response, i.e., phase angle, is observed in the dynamic modulus tests of asphalt (viscoelastic) materials, as shown in Figure 1-3(b). According to the cyclic fatigue test specified in AASHTO TP 133-21, the phase angle gradually increases with increasing loading cycles, indicating that the phase angle has the potential to indicate the fatigue condition of the asphalt material. The TSD deflection lag may be closely related to phase angle and may also be served as an index to indicate pavement crack conditions.

An accurate assessment of existing pavements provides essential inputs to maintenance and rehabilitation (M&R) strategies makers, thereby helping optimize the use of limited funds. However, the current pavement management system (PMS) focuses mainly on the pavement functional conditions and fails to identify the underlying reasons for pavement deterioration. Pavement structural conditions are rarely incorporated into the PMS. With the development of measurement technology, in addition to deflection, the TSD is also equipped with an Automatic Crack Detection (ACD) system that collects high-quality images of pavement surface cracks, as shown in Figure 1-4. The combination of pavement functional and structural information allows for a more comprehensive and accurate assessment of pavement performance, thereby facilitating more appropriate decisions on M&R strategies and more accurate predictions of pavement conditions. Therefore, a framework that integrates TSD deflection with the pavement functional condition should be developed.

Numerical Simulation

There is currently no TSD database of various pavement structures available, so mechanical-based approaches are preferred to simulate load configurations and obtain theoretical pavement responses. In the early 1960s, mechanistic procedures were introduced to estimate the pavement response caused by traffic loads and have been evolving ever since. The 3D-Move program developed by the University of Nevada, Reno [16] is ideally suitable for simulating pavement responses under moving loads. The applicability and accuracy of the 3D-Move program have been verified in the literature [10,13,16]. In addition, the 3D-Move is a versatile program that comprehensively considers material viscoelasticity, non-uniform contact pressure, and variable vehicle speed, making it suitable for FWD and TSD simulations [9].

The 3D-Move program uses the finite layer method and Fourier transform technology to simulate pavement responses under moving loads [10]. The finite layer method takes advantage of the layered characteristics of the pavement structure, so it is an efficient tool for simulating pavement responses compared to the more complicated and general-purpose finite-element programs such as ABAQUS [17]. In addition, traditional multi-layer elastic programs such as BISAR are easy to use, but they cannot accurately simulate pavement responses associated with moving loads. Most of them are limited to static uniform circular loads, while TSD loads need to be defined as moving dual tires loads. Therefore, the 3D-Move program allows a more efficient and practical consideration of the interaction between the load and the pavement [18]. In addition, 3D-Move allows the incorporation of viscoelastic materials, so that the asphalt layer can be simulated as either linear elastic or viscoelastic. To characterize the viscoelastic behavior of the AC layer, the dynamic modulus curve needs to be fed into the 3D-Move program.

The main input parameters of the 3D-Move program include analysis type (static or dynamic), loading configuration (load magnitude, tire contact shape, and vehicle speed), and material properties (thickness and modulus). The 3D-Move program outputs critical pavement responses such as stress, strain, and displacement. In static analysis, the 3D-Move calculates the pavement responses at the specified locations. For dynamic analysis, the 3D-Move will output a continuous pavement response over time. By multiplying the time by the moving speed, the pavement response at the specified locations can be calculated from the time-varying curves [19].

In this study, the TSD loading configurations were based on the Intelligent Pavement Assessment Vehicle (iPAVe) operated by the Australian Road Research Board (ARRB) group Inc.

Objectives

The overall objective of the proposed doctoral study is to investigate the use of TSD deflection in network-level pavement evaluation. The research scopes are to (1) provide a reliable TSD deflection correction procedure considering the effects of load magnitude, test temperature, and test speed; (2) assess the applicability and substitutability of existing

FWD-based methods for TSD; (3) develop TSD-oriented evaluation methods and applications; (4) correlate TSD deflections with pavement functional conditions.

References

[1] Elseifi, M. A., Gaspard, K., Wilke, P. W., Zhang, Z., & Hegab, A. (2015). Evaluation and validation of a model for predicting pavement structural number with rolling wheel deflectometer data. Transportation Research Record, 2525(1), 13-19.

[2] Alavi, S., LeCates, J. F., & Tavares, M. P. (2008). Falling weight deflectometer usage (No. Project 20-5 (Topic 38-15)).

[3] Elbagalati, O., Elseifi, M., Gaspard, K., & Zhang, Z. (2018). Development of the pavement structural health index based on falling weight deflectometer testing. International Journal of Pavement Engineering, 19(1), 1-8.

[4] Transportation Officials. (1993). AASHTO Guide for Design of Pavement Structures, 1993 (Vol. 1). Aashto.

[5] Lytton, R. L. (1989). Backcalculation of pavement layer properties (pp. 7-38). ASTM International.

[6] Flintsch, G., Katicha, S., Bryce, J., Ferne, B., Nell, S., & Diefenderfer, B. (2013). Assessment of continuous pavement deflection measuring technologies (No. SHRP 2 Report S2-R06F-RW-1).

[7] Flintsch, G. W., Ferne, B., Diefenderfer, B., Katicha, S., Bryce, J., & Nell, S. (2012). Evaluation of traffic-speed deflectometers. Transportation research record, 2304(1), 37-46.

[8] Zhang, M., Zhang, J., Gong, H., Jia, X., Xiao, R., Huang, H., & Huang, B. (2022). Numerical investigation of pavement responses under TSD and FWD loading. Construction and Building Materials, 318, 126014.

[9] Nasimifar, M., Thyagarajan, S., & Sivaneswaran, N. (2017). Backcalculation of flexible pavement layer moduli from traffic speed deflectometer data. Transportation Research Record, 2641(1), 66-74.

[10] Elseifi, M. A., Zihan, Z. U., & Icenogle, P. (2019). A Mechanistic Approach to Utilize Traffic Speed Deflectometer (TSD) Measurements into Backcalculation Analysis (No. FHWA/LA. 17/612). Louisiana State University. Department of Civil and Environmental Engieering.

[11] Nasimifar, M., Thyagarajan, S., & Sivaneswaran, N. (2018). Computation of pavement vertical surface deflections from traffic speed deflectometer data: evaluation of current methods. Journal of Transportation Engineering, Part B: Pavements, 144(1), 04018001.

[12] Katicha, S. W., Flintsch, G. W., Ferne, B., & Bryce, J. (2014). Limits of agreement method for comparing TSD and FWD measurements. International Journal of Pavement Engineering, 15(6), 532-541.

[13] Rada, G. R., Nazarian, S., Visintine, B. A., Siddharthan, R. V., & Thyagarajan, S. (2016). Pavement structural evaluation at the network level (No. FHWA-HRT-15-074). United States. Federal Highway Administration. Office of Infrastructure Research and Development.

[14] Zhang, M., Gong, H., Jia, X., Jiang, X., Feng, N., & Huang, B. (2022). Determining pavement structural number with traffic speed deflectometer measurements. Transportation Geotechnics, 35, 100774.

[15] Elbagalati, O., Mousa, M., Elseifi, M. A., Gaspard, K., & Zhang, Z. (2018). Development of a methodology to backcalculate pavement layer moduli using the traffic speed deflectometer. Canadian Journal of Civil Engineering, 45(5), 377-385.

[16] Nasimifar, M., Siddharthan, R. V., Rada, G. R., & Nazarian, S. (2017). Dynamic analyses of traffic speed deflection devices. International Journal of Pavement Engineering, 18(5), 381-390.

[17] Huhtala, M., & Pihlajamaki, J. (1992). New concepts on load equivalency measurements. In International Conference on Asphalt Pavements, 7th, 1992, Nottingham, United Kingdom (Vol. 3).

[18] Siddharthan, R. V., Yao, J., & Sebaaly, P. E. (1998). Pavement strain from moving dynamic 3 D load distribution. Journal of Transportation Engineering, 124(6), 557-566.

[19] Nitharsan, R. (2011). Development of windows-based version of the 3d-move analysis software for pavement response analysis. University of Nevada, Reno.

Appendix

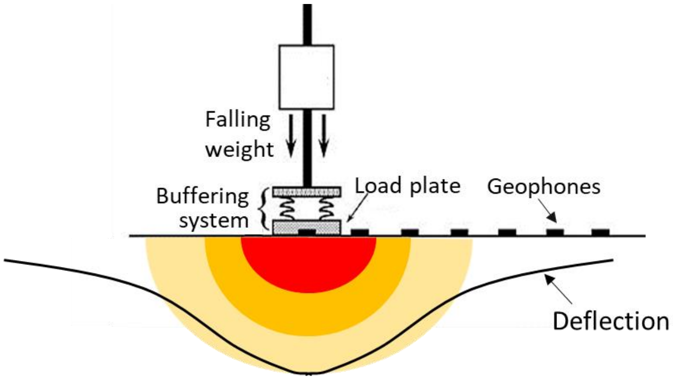

Figure 1-1. Schematic of FWD

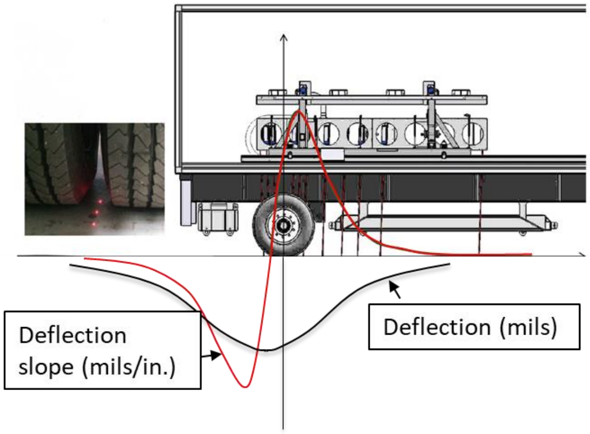

Figure 1-2. Schematic of TSD

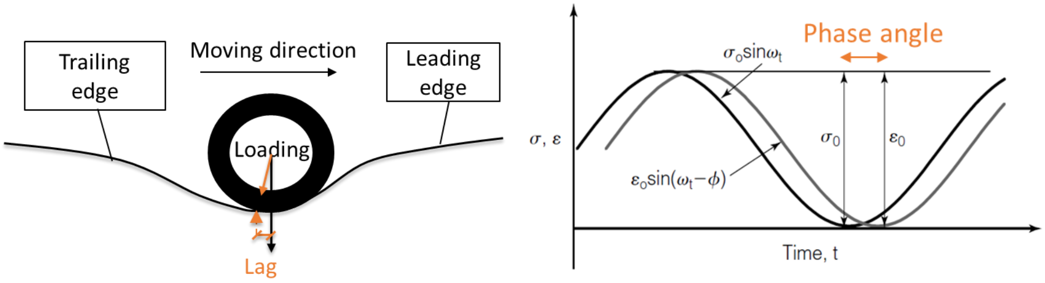

(a) (b)

Figure 1-3. Lag: (a) in TSD deflection basin; (b) in dynamic modulus (phase angle) test

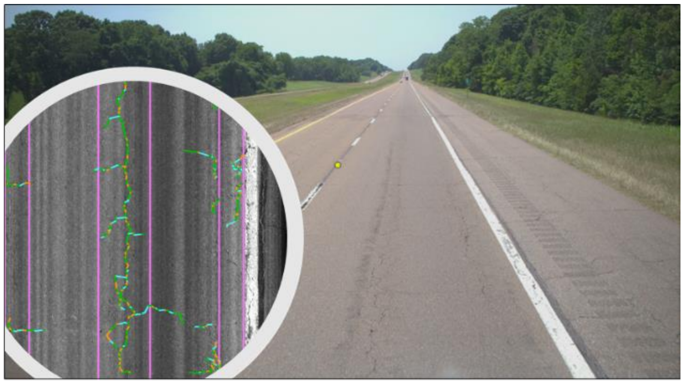

Figure 1-4. Automatic crack detection system

Table 1-1. Comparison between TSD and FWD

	TSD	FWD
Load	moving load	impact load
Measurement	deflection velocity	deflection
Social benefit	• non-destructive • time saving • little or no traffic control	• non-destructive • time-consuming • traffic closure
Test scope	network-level (preferred)	project-level (preferred)

CHAPTER 2

SPEED AND TEMPERATURE SUPERPOSITION ON TRAFFIC SPEED DEFLECTOMETER MEASUREMENTS

A version of this chapter was recently submitted for possible publication by Miaomiao Zhang, Guozhi Fu, Yuetan Ma, Rui Xiao, and Baoshan Huang to Transportation Geotechnics.

My contributions were conducting the literature review, performing the theoretical analysis and derivation of formulas, developing numerical simulation models, and writing the text contained in the paper. Dr. Guozhi Fu, Dr. Yuetan Ma, Dr. Rui Xiao, and Dr. Baoshan Huang provided ideas, guidance, and comments throughout the whole research and offered editorial assistance with the text.

Abstract

The traffic speed deflectometer (TSD) is capable of conducting deflection surveys at traffic speeds and is an efficient tool for collecting network-level pavement structural data. Due to the viscoelastic nature of asphalt concrete (AC), the raw TSD deflections need to be corrected to the reference temperature and speed so that data from different tests can be comparable. Although the topic of temperature correction for deflections has been extensively discussed, however, the correction of traffic speed on pavement deflection has rarely been investigated. According to the principle of time-temperature superposition, the time (speed) effect on pavement responses can be evaluated by the concept of “pseudo temperature”. Combined with the test temperature, the time and temperature dependence of AC materials can be integrated into a single factor, the effective temperature. By correcting raw TSD deflections from the effective temperature to the reference temperature, speed correction and temperature correction can be achieved simultaneously. It also provides some insights into eliminating the need for temperature correction by artificially presetting the TSD speed so that the TSD deflection collected at the preset speed and test temperature is equal to the TSD deflection at the reference speed and reference temperature. Results from the present analysis suggest that TSD deflections are more sensitive to test temperatures than to test speeds. The equivalence between speed and temperature depends on the activation energy of the AC material. For normal TSD operating speeds, a 10 mph increase in test speed is approximately equivalent to a 1°C drop

in temperature. In general, a practical preset speed range of 20-60mph can accommodate temperature variations of approximately 4°C.

Introduction

The incompleteness of construction history and the resulting inaccurate estimates of pavement structural capacity necessitates the use of innovative techniques to obtain accurate network-level pavement structural data. Currently, deflection measurements remain the only reliable non-destructive method for determining the structural strength of flexible pavements. The stationary Falling Weight Deflectometer (FWD) is the most prevailing method of deflection measurement [1]. However, FWD is the preferred device for project-level structural evaluation, but issues such as time, expenses, and traffic control hinder FWD testing at the network-level. Recent technological advancements have led to the development of continuous deflection measurement devices, including traffic speed deflectometer (TSD) [2], to overcome the limitations of FWD.

Unlike static measurement devices, TSD is capable of performing deflection surveys at traffic speeds, which provides a safe and efficient tool for collecting network-level pavement structural data [3]. However, some challenges exist in applying TSD for routine survey works. The accuracy and precision of TSD measurements can be influenced by several internal and external factors, e.g., calibration procedures, travel speed, wind and temperature during the test, and tire-pavement interaction [4,5]. Therefore, it is necessary to develop a reliable TSD deflection correction procedure so that TSD deflections collected at different trips or under different conditions can be comparable.

The load magnitude directly affects pavement deflections. TSD nominally applies a load of approximately 50kN to the pavement, while the actual dynamic load varies continuously due to changes in pavement conditions. TSD continuously records the applied axle load during the test. According to the homogeneity of linear viscoelastic materials, the pavement response is proportional to the load magnitude. Therefore, TSD deflections can be corrected to a standard load level (reference load) by load correction [6].

In addition, due to the viscoelastic nature of the asphalt concrete (AC) layer, the TSD deflection is influenced by temperature and test speed. The temperature correction for FWD deflection has been widely discussed. The 1993 AASHTO Pavement Design Guide proposed a general temperature correction procedure for the FWD deflection at the loading point (D0) [7]. Chen et al. showed that only FWD deflections with radial distances of 0 (D0) and 8 inches (D8) were strongly affected by temperature, and they developed temperature correction equations for D0 and D8 for flexible pavements in Texas [8]. Mun Park et al. developed temperature correction equations for FWD deflections at varying radial distances from the loading point based on deflections measured on flexible pavements in North Carolina [9]. Subsequent related studies focused on the local calibration of the temperature correction factor [10,11]. The temperature correction equations for TSD deflections are still under investigation. Nasimifar et al. proposed a temperature correction equation for adjusting the TSD-based surface curvature index (SCI, the deflection difference between D0 and D12 (the deflection at a radial distance of 12 inches)) based on numerical simulation results [12].

Since the FWD must remain stationary at each test point, the speed correction for deflections, unlike the temperature correction, has rarely been investigated. The TSD speed varies depending on the road grades and traffic conditions. In addition, the TSD may move slowly due to traffic jams or even stop due to traffic signals. Elseifi et al. conducted TSD tests at 30 mph, 45 mph, and 60 mph to investigate the effect of TSD speed on TSD measurements [13]. The COV (coefficient of variation) of the deflection slope collected at 30 mph was approximately 24% lower than the 45 mph measurement, while the COV at 60 mph was approximately 38% higher than the 45 mph measurement. The results suggested that the deflection was sensitive to the TSD moving speed. Therefore, it is necessary to set a reference speed for the TSD deflection and to develop a speed correction method. TSD deflections should be corrected to the same reference speed so that raw TSD measurements collected at different speeds can be compared.

According to the equivalence of time (speed) and temperature on the AC dynamic modulus, the speed correction can also be equivalent to the temperature correction, i.e., the speed correction for deflections can be achieved by means of temperature correction. The objective of this study was to introduce a single factor that combines both temperature and time (speed) effects based on the time-temperature superposition principle. This single factor is referred to as “effective temperature”. With only one factor (effective temperature) instead of two (test temperature and test speed), the speed correction and temperature correction can be performed simultaneously. In addition, the possibility of eliminating the need for temperature correction by artificially presetting the test speed can be assessed.

Since deflection measurements of concrete pavements are almost negligible [14] and almost independent of test temperatures and speeds [4], this study focused only on asphalt pavements and concrete pavements were not included.

Speed Correction Method

Effective temperature

The AC dynamic modulus master curve can be mathematically modeled by a sigmoidal function [15,16]:

$$\log|E^*| = \log(Min) + \frac{\log(Max) - \log(Min)}{1 + e^{\beta + \gamma \log w_r}} \tag{1}$$

where: $|E^*|$ = dynamic modulus, ksi; w_r = reduced frequency, Hz; Max = limiting maximum modulus, ksi; Min = limiting minimum modulus, ksi; β, γ = fitting shape parameters.

It is well known that the AC dynamic modulus master curve is developed based on the time-temperature superposition principle. Dynamic modulus data tested at different temperatures can be “shifted” relative to the loading frequency (time) so that the different curves can be aligned to form the master curve [17]. The shift factor $a(T_t)$ defines the required shift at a given temperature T_t and can be calculated using the Arrhenius equation.

$$log w_r = log w_t + \log[a(T_t)] \tag{2}$$

$$\log[a(T_t)] = \frac{\Delta E_a}{19.14714}\left(\frac{1}{T_t} - \frac{1}{T_{ref}}\right) \tag{3}$$

where: w_r = reduced frequency, Hz; w_t = loading frequency at the test speed, Hz; $a(T_t)$ = shift factor at temperature T_t; T_t = test temperature, Kelvin; T_{ref} = reference temperature, Kelvin; ΔE_a = activation energy (treated as a fitting parameter), J/mol.

According to the time-temperature superposition principle, the effects of loading time (speed) and temperature on the AC dynamic modulus are equivalent. Therefore, the effect of time (speed) on the AC dynamic modulus can be evaluated by the concept of "pseudo temperature". Combined with the test temperature, the time and temperature dependence of the AC material can be integrated into a single factor known as the "effective temperature". The dynamic modulus at the test speed and test temperature can be equated to the dynamic modulus at the reference speed and effective temperature. Equation (2) can be rewritten as:

$$log w_r = log w_t + \log[a(T_t)] = log w_{ref} + \log\left[a\left(T_{eff}\right)\right] \quad (4)$$

where: w_r = reduced frequency, Hz; w_t = loading frequency at the test speed, Hz; T_t = test temperature, Kelvin; w_{ref} = loading frequency at the reference speed, Hz; T_{eff} = effective temperature, Kelvin. Substituting Equation (3) into Equation (4), the following equation can be obtained to calculate the effective temperature:

$$\frac{1}{T_{eff}} = \frac{1}{T_t} + \left(log\frac{w_t}{w_{ref}}\right) * \frac{19.14714}{\Delta E_a} \quad (5)$$

Determining the loading frequency from the loading time (speed) has been a controversial topic [18]. There are several different time-to-frequency conversion methods [18–20], and choosing an appropriate one can be very difficult. However, the effective temperature is not directly related to the loading frequency but rather to the ratio of w_t to w_{ref}, which can be calculated from the following form:

$$\frac{w_t}{w_{ref}} = \frac{V_t}{V_{ref}} \quad (6)$$

where: w_t = loading frequency at the test speed, Hz; w_{ref} = loading frequency at the reference speed, Hz; V_t = test speed; V_{ref} = reference speed. Therefore, the effective temperature can be calculated from:

$$\frac{1}{T_{eff}} = \frac{1}{T_t} + \left(log\frac{V_t}{V_{ref}}\right) * \frac{19.14714}{\Delta E_a} \quad (7)$$

where: V_t = test speed; V_{ref} = reference speed; T_t = test temperature, Kelvin; T_{eff} = effective temperature, Kelvin; ΔE_a = activation energy, J/mol.

The pseudo temperature (T_s) is the difference between the effective temperature and the test temperature:

$$T_s = T_{eff} - T_t \tag{8}$$

The calculation of the effective temperature and pseudo temperature avoids the common errors caused by time-to-frequency conversion and is therefore concise and trustworthy. According to Equation (7), the effective temperature for any TSD speed at any test temperature can be calculated. The effective temperature combines the effects of both the test speed and the test temperature. On this basis, only the (effective) temperature correction is needed to achieve both temperature and speed correction for raw TSD deflections.

Influencing factors

From Equations (7) and (8), it can be found that the effective (or pseudo) temperature is not related to the reference temperature, but to the reference speed. In addition, the effective (or pseudo) temperature is also associated with the test temperature and the activation energy of the asphalt mixture. Pellinen et al. measured an average activation energy of 205,000 J/mol for unmodified AC mixtures and 202,000 J/mol for modified AC mixtures [16]. The effects of the following different reference speeds, test temperatures, and activation energies on the effective (or pseudo) temperature were investigated:

- Reference speed: 20, 40, 60 mph.
- Test temperature: 10, 20, 30 °C.
- Activation energy: 150,000, 200,000, 250,000 J/mol.

The default value for the reference speed, test temperature, and activation energy in this study is 40 mph, 20 °C, and 200,000 J/mol, respectively.

The AC dynamic modulus increases with decreasing temperature or increasing loading frequency. The effects of temperature and loading frequency are equivalent but opposite. Therefore, a larger test speed (loading frequency) is expected to imply a smaller effective (or pseudo) temperature. The results in Figures. 1-3 (all tables and figures are located in the Appendix) confirm this expectation that the effective (or pseudo) temperature decreases as the test speed increases. The pseudo temperature (Figures. 1-3 (b)) is a translation (minus the test temperature) of the effective temperature (Figures. 1-3 (a)). When the test speed is exactly equal to the reference speed, the pseudo temperature is zero and the effective temperature is the test temperature. When the test speed is lower than the reference speed, the pseudo temperature is greater than zero, and the effective temperature is greater than the test temperature. Conversely, when the test speed is greater than the reference speed, a negative pseudo temperature occurs, and the effective temperature is smaller than the test temperature. Therefore, it can be concluded that the pseudo temperature comes from the difference between the test speed and the reference speed.

The equivalence between speed and temperature is defined as the change in temperature corresponding to a unit change in test speed, i.e., the slope of the effective (or pseudo) temperature curve. The equivalence between speed and temperature is related to the test speed, because the slope of the effective (or pseudo) temperature curve is not constant but decreases with increasing test speed. Therefore, for smaller test speeds (0-20 mph), the unit change in speed corresponds to a great change in temperature. As the test speed increases (>20 mph), the slope of the effective (or pseudo) temperature curve tends to be constant, so that the equivalence between speed and temperature is nearly constant. Within the normal operating speed range of the TSD (20-60 mph), a speed change of 10 mph corresponds approximately to an effective (or pseudo) temperature change of 1°C. Therefore, for TSD deflections collected at normal TSD operating speeds, a 10 mph increase in test speed is approximately equivalent to a 1°C drop in test temperature.

Figure 2-1 shows the effect of the choice of the reference speed on the effective (or pseudo) temperature. For the same test speed, the lower the reference speed, the lower the pseudo temperature, and the lower the effective temperature. The slopes of different effective (or pseudo) temperature curves (within a test speed of 20-60 mph) are similar regardless of the reference speed, so the equivalence between speed and temperature is independent of the reference speed. Therefore, there is no preference for the choice of reference speed as far as the equivalence is concerned. However, it is recommended that the reference speed be the average test speed, which will always result in smaller absolute pseudo temperatures, thus reducing the need for temperature corrections.

Figure 2-2 shows the effect of the test temperature on the effective (or pseudo) temperature. It can be found that at the same test speed, the lower the test temperature, the lower the effective temperature. However, the pseudo temperature curves for different test temperatures are very close, indicating that the effect of test temperature on the pseudo temperature is negligible. In addition, the slopes of the different effective (or pseudo) temperature curves are similar, so the equivalence between speed and temperature is independent of the test temperature.

The effect of AC materials (activation energy) on the effective (or pseudo) temperature is shown in Figure 2-3. At the same test speed, the absolute pseudo temperature is greater for AC materials with lower activation energies. For different AC materials (activation energy), the slope of the effective (or pseudo) temperature curve is different, so the equivalence between speed and temperature depends on the activation energy of the AC material. For AC materials with smaller activation energy, the same speed change corresponds to a larger temperature change.

Validation of the Speed Correction Method

The numerical simulation method was employed in this study to verify the effectiveness of the proposed speed correction method. TSD models of a three-layer pavement structure were developed by the 3D-Move program [6,21], as shown in Table 2-1. A typical plant-produced AC was used as the AC layer with an activation energy of 215900.1 J/mol. The viscoelasticity of the AC layer was incorporated through the dynamic modulus (temperature- and frequency-dependent).

According to Equation (7), the test speed and test temperature are integrated into one single factor, i.e., the effective temperature. By correcting the TSD deflection from the effective temperature to the reference temperature, a double correction of both speed and temperature can be achieved. The TSD deflection collected at the test speed and test temperature can be corrected to the reference speed and reference temperature using the temperature correction method only. Therefore, the essence of speed correction is temperature correction.

Since there is no satisfactory temperature correction method for TSD deflections, the most commonly used FWD-based method, i.e., the AASHTO temperature correction method, was employed in this study. Therefore, the applicability of the AASHTO method to TSD deflections should first be verified. Then, develop TSD models at different test speeds. Finally, apply the proposed speed correction method to TSD deflections at different speeds to verify its effectiveness.

AASHTO temperature correction

The AASHTO temperature correction method is based on the FWD deflection and is for D0 only [7]. The temperature correction is achieved by applying an adjustment factor to the raw D0, as shown in Figure 2-4. When the test temperature is the reference temperature (20°C), no temperature correction is needed so the temperature adjustment factor is exactly 1.0. For test temperatures higher than the reference temperature, the AC layer tends to exhibit a lower stiffness than expected. As a result, the pavement deflection tends to be higher than expected and the adjustment factor will be less than 1.0. The opposite is true when the test temperature is lower than the reference temperature. In addition, the temperature adjustment factor is different for different AC thickness. Pavements with thicker asphalt layers are more affected by the test temperature and therefore require greater temperature adjustment.

To verify the applicability of the AASHTO method to TSD deflections, TSD models with different test temperatures were developed using the 3D-Move program. Nine test temperatures were considered: 0,10, 18, 19, 20, 21, 22, 30 and 40°C, and the theoretical TSD deflections at different test temperatures are shown in Figure 2-5. It can be found that the TSD deflection near the loading point increases with the increase in temperature. In addition, deflections near the loading point are more sensitive to temperature than deflections at distant locations. TSD models with higher temperatures have steeper deflection basins.

The results in Table 2-2 can be obtained by applying the AASHTO temperature correction method to the D0 of TSD. The D0 at reference temperature (20°C) is considered the reference D0. It can be found that the error of the corrected D0 is greatly reduced compared with the raw D0. The error in D0 is well corrected for temperatures close to 20°C and temperatures significantly different from 20°C. The closer the test temperature is to the reference temperature, the closer the corrected D0 will be to the reference D0, and the better the temperature correction will be. Overall, the FWD-based AASHTO temperature correction method is applicable to D0 of TSD.

TSD models at different speeds

TSD models with different test speeds were developed using the 3D-Move program. Seven test speeds were considered: 10, 20, 30, 40, 50, 60 and 70 mph, and the test temperature was set to 20°C. The theoretical TSD deflections at different speeds are shown in Figure 2-6. It can be found that D0 increases as the TSD speed decreases, while the opposite is true for the distant deflection. This can be explained by the fact that as the TSD speed increases, the loading frequency increases and the AC layer exhibits higher stiffness, so D0 decreases. In addition, TSD deflections are more sensitive to lower TSD speeds (10-20mph), while the difference between higher speeds (50-70mph) is relatively insignificant, implying a nonlinear effect of test speed on TSD deflection. Overall, TSD deflections are less sensitive to TSD speeds than to test temperatures.

Application of the speed correction method

As discussed above, the effective temperature combines the effects of both the test speed and the test temperature. Only the (effective) temperature correction is needed to correct the raw TSD deflections from the test temperature and test speed to the reference temperature and reference speed. The speed correction and temperature correction are achieved simultaneously rather than sequentially. The temperature correction method can be any method that is applicable to TSD deflections. In this study, the AASHTO temperature correction method was employed, and its applicability has been verified in the previous section. In addition, TSD deflections should first be normalized to the same reference load magnitude. The detailed procedure for TSD deflection correction is:

Step 1: Determine the reference load magnitude, reference speed, and reference temperature.

Step 2: Input the TSD deflections, load magnitude, test speed, and test temperature.

Step 3: Input the thickness of the AC layer. (Optional: Input the activation energy of the AC material, the default value is 200,000 J/mol.)

Step 4: Correct TSD deflections to the reference load magnitude.

Step 5: Calculate the effective temperature based on test speed and test temperature using Equation (7).

Step 6: Obtain the adjustment factor for the effective temperature based on AC thickness according to the AASHTO temperature correction method.

Step 7: Apply the adjustment factor to the load-corrected D0 of TSD to obtain the speed-and temperature-corrected D0.

To verify the effectiveness of the proposed speed correction method, it was applied to the theoretical deflections at different TSD speeds, including:

- Case 1: Constant test temperature (20°C, equal to the reference temperature). The test temperature is not expected to have an additional effect on TSD deflections, so no correction for the test temperature is actually needed. In this case, improvements from corrections for the test temperature can be excluded, so all possible improvements come from the speed correction. It should be noted that the speed correction is ultimately achieved by the AASHTO temperature correction method using the “effective temperature”.
- Case 2: Different test temperatures (0, 10, 19, 20, 21, 30, 40°C). Corrections for both test temperature and test speed are required, which can be achieved simultaneously with the effective temperature correction.

The activation energy of 215,900.1 J/mol was used in calculating the effective temperature. The D0 at the reference temperature (20°C) and the reference speed (40 mph) was considered as the reference D0 (15.91 mils). Table 2-3 shows the D0 results before and after the speed correction. When the test speed is exactly equal to the reference speed (40 mph), the effective temperature is equal to the test temperature, and the raw D0 is equal to the corrected D0 and the reference D0. For Case 1 (the constant test temperature), the error of the corrected D0 is greatly reduced compared with the raw D0. The closer the test speed is to the reference speed, the closer the corrected D0 will be to the reference D0, and the better the speed correction will be. Even taking into account the different test temperatures (Case 2), the deviation of the corrected D0 from the reference D0 is greatly reduced. Therefore, the proposed method is effective for cases where only speed correction is required as well as cases where both temperature and speed correction are required.

The effect of the activation energy estimation on the speed correction was also explored, as shown in Figure 2-7. It can be found that the difference between the effective temperature and the test temperature, i.e., the absolute pseudo temperature, decreases with increasing activation energy for the same test speed. The effectiveness of the speed correction is related to the estimation of the activation energy. The closer the estimate of the activation energy is to the actual activation energy (215,900.1 J/mol), the closer the corrected D0 is to the reference D0. The error of the corrected D0 is always smaller than the error of the raw D0, even if the estimate of the activation energy is far from its true value. Therefore, the default value of 200,000 J/mol is a safe estimate of the activation energy.

Preset Speed Method

Preset speed

The speed correction method combines the effects of test speed and test temperature by introducing the effective temperature, which is essentially temperature correction. The effectiveness of the speed correction depends on the effectiveness of the temperature correction method. However, there is no satisfactory temperature correction method for TSD deflection, especially for the whole TSD deflection basin.

During the TSD test, the test temperature is not subject to human interference, while the TSD speed can be controlled by humans. According to the time-temperature superposition principle, the TSD test speed can be artificially set so that the pavement response at the preset test speed and test temperature is equal to the pavement response at the reference speed and reference temperature. This eliminates the need for temperature correction of the TSD deflections, thus avoiding errors caused by temperature correction.

Based on the assumption that the AC dynamic modulus at the preset test speed and test temperature is equal to the AC dynamic modulus at the reference speed and reference temperature, Equation (4) can be rewritten as:

$$logw_r = logw_{ref} + \log\left[a\left(T_{ref}\right)\right] = logw_{set} + \log[a(T_t)] \tag{9}$$

where: w_r = reduced frequency, Hz; w_{ref} = loading frequency at the reference speed, Hz; T_{ref} = reference temperature, Kelvin; w_{set} = loading frequency at the preset test speed, Hz; T_t = test temperature, Kelvin.

Substituting Equations (3) and (6) into Equation (9), the preset test speed can be calculated by the following equation:

$$\frac{V_{ref}}{V_{set}} = \frac{w_{ref}}{w_{set}} = 10\hat{}[\frac{\Delta E_a}{19.14714}\left(\frac{1}{T_t} - \frac{1}{T_{ref}}\right)] \tag{10}$$

where: w_{ref} = loading frequency at the reference speed, Hz; T_{ref} = reference temperature, Kelvin; w_{set} = loading frequency at the preset speed, Hz; T_t = test temperature, Kelvin; ΔE_a = activation energy, J/mol; V_{set} = preset test speed; V_{ref} = reference speed. The effect of test temperature is evaluated by “pseudo speed”. The pseudo speed (V_s) is defined as the difference between the preset speed and the reference speed:

$$V_s = V_{set} - V_{ref} \tag{11}$$

Influencing factors

Similarly, the preset speed method avoids the time-to-frequency conversion. The preset test speed for different test temperatures can be calculated by Equation (10). In addition, the preset speed is related to the reference speed, reference temperature, and the activation energy of the AC material. The effects of the following different reference speeds, reference temperatures, and activation energies on the preset speed were investigated:

- Reference speed: 30, 40, 50 mph.
- Reference temperature: 15, 20, 25 °C.
- Activation energy: 150,000, 200,000, 250,000 J/mol.

The default value for the reference speed, reference temperature, and activation energy in this study is 40 mph, 20 °C, and 200,000 J/mol, respectively.

Since speed and temperature have opposite effects on AC dynamic modulus, the preset test speed should be increased to counteract the effect of increasing test temperature, as shown in Figures. 8-10. The pseudo speed (Figures. 8-10 (b)) is a translation (minus the reference speed) of the preset speed (Figures. 8-10 (a)). In contrast to the pseudo temperature, the pseudo speed comes from the difference between the test temperature and the reference temperature. When the test temperature is exactly equal to the reference temperature, the pseudo speed is zero and the preset speed is the reference speed. When the test temperature is lower than the reference temperature, the AC layer exhibits a higher stiffness than expected and the collected TSD deflection will be smaller than expected. Therefore, the preset test speed should be less than the reference speed (pseudo speed is negative) to offset the gain effect caused by low temperature. Conversely, a test temperature higher than the reference temperature corresponds to a positive pseudo speed, and the preset speed should be greater than the reference speed.

The slope of the preset speed curve is the change in preset speed caused by a unit change in test temperature, implying the ability to adapt to temperature variations by adjusting the preset speed. A small slope means that for the same temperature variation, only a small preset speed adjustment is needed to accommodate it, which is more beneficial for practical applications. In Figures. 8-10 (a), the slope of the preset speed curve increases with increasing test temperature. When the test temperature is very low (relative to the reference temperature), only small adjustments to the preset speed are needed to accommodate temperature variations. However, for higher test temperatures (relative to the reference temperature), a slight variation in test temperature will lead to a great change in the preset speed. In practice, the operating speed of the TSD is constrained by the performance of the TSD equipment, traffic conditions, and road speed limits. The preset test speed should be limited to a practical range of 20-60 mph, marked in red in Figures. 8-10 (a). In general, the preset speed range of 20-60mph can accommodate temperature variations of approximately 4°C. The annual average diurnal air temperature difference in the continental United States is about 13 °C [22], so the preset speed method is not sufficient to fully accommodate anticipated temperature changes in the field. Therefore, it is only recommended for short TSD trips.

Figure 2-8 shows the effect of the choice of the reference speed on the preset (or pseudo) speed. It can be found that at the same test temperature, the greater the reference speed, the greater the preset speed. Although the slopes of the different pseudo speed curves are obviously different, what is important is the slope at the preset speeds of 20-60mph, which are very close to each other. The choice of reference speed does not affect the ability to adapt to temperature variations by presetting the TSD speed. However, the reference speed will affect the acceptable temperature range. For example, when the reference speed is 30 mph, the acceptable temperature is limited to about (*reference temperature*-1°C, *reference temperature*+3°C); when the reference speed is 40 mph, the acceptable temperature is limited to about (*reference temperature*-2°C, *reference temperature*+2°C). When the reference speed is the median of the feasible preset speeds (40 mph), the acceptable temperature range is symmetrical to the reference temperature. Therefore, the recommended reference speed is 40 mph.

The effect of the choice of the reference temperature on the preset (or pseudo) speed is shown in Figure 2-9. At the same test temperature, the lower the reference temperature, the greater the pseudo speed, and the greater the preset speed. The slope of the preset speed curve (within 20-60mph) is also similar for different reference temperatures, showing no preference for the choice of reference temperature. When the reference speed is 40 mph, the acceptable temperature is within ±2°C of the reference temperature. Therefore, the recommended reference temperature is the average test temperature.

Figure 2-10 shows the effect of AC materials (activation energy) on the preset (or pseudo) speed. It can be found that at the same test temperature, the greater the activation energy, the greater the absolute pseudo speed. The slope of the preset speed curve (within 20-60mph) of different AC materials is different, so the AC materials will affect the ability to adapt to temperature variations by presetting the TSD speed. For AC materials with smaller activation energy (smaller slope), this method of presetting test speed can accommodate more temperature variations.

Validation of the Preset Speed Method

The detailed procedure for collecting TSD deflection at preset speeds is:

Step 1: Determine the reference speed and reference temperature.

Step 2: Input the test temperature. (Optional: Input the activation energy of the AC material, the default value is 200,000 J/mol.)

Step 3: Calculate the preset test speed based on test temperature using Equation (10).

Step 4: Collect TSD deflections at the preset test speed.

Step 5: Measure the test temperature continuously and adjust the test speed accordingly, then go to step 2.

Figure 2-11(a) shows the TSD deflections at different test temperatures (18-22°C) and the reference speed (40 mph). To verify the effectiveness of the proposed preset speed method, TSD models for different test temperatures (18-22°C) at different preset speeds were developed using the 3D-Move program, and the theoretical deflection results are shown in Figure 2-11(b). The activation energy of 215,900.1 J/mol was used in calculating the preset speed. The TSD deflection basin at 20°C (reference temperature) and 40 mph (reference speed) is considered the reference basin. Different TSD deflection basins were compared with the reference basin, and the errors were evaluated by the root mean square error (RMSE, in Equation (12)). It can be found that the TSD deflection basin collected at the preset speed is closer to the reference basin than the TSD deflection basin collected at the reference speed (40 mph). The closer the test temperature is to the reference temperature, the smaller the error of the preset speed method. When the test temperature is exactly equal to the reference temperature (20°C), the preset speed is equal to the reference speed, and the error of the TSD deflection basin is zero. TSD deflection basins at the preset speeds all essentially coincide with the reference basin, both in terms of deflections near the loading point and in terms of deflections at distant locations.

$$RMSE = \sqrt{\frac{1}{n}\sum_{k=1}^{n}(y_k - \hat{y}_k)^2} \tag{12}$$

where $\boldsymbol{y_k}$ is the reference value; $\boldsymbol{\hat{y}_k}$ is the predictions.

Table 2-4 explores the effect of the activation energy estimation on the validity of the preset speed method. For different activation energies, the preset speeds corresponding to different test temperatures were calculated separately. A total of 15 TSD models were developed for five different test temperatures (18-22°C) and corresponding preset speeds. Their theoretical deflection basins were all compared with the reference TSD basins. It can be found that for the same test temperature, the difference between the preset speed and the reference speed, i.e., absolute pseudo speed, increases with increasing activation energy. The closer the estimate of the activation energy is to the actual activation energy (215,900.1 J/mol), the smaller the error (evaluated by RMSE) of the preset speed method. The preset speed method always leads to a more accurate TSD basin, regardless of how much the activation energy estimation differs from its true value.

Conclusion

Due to the viscoelasticity of the AC layer, TSD deflections are affected by both test temperature and test speed. TSD deflections should be corrected to the reference temperature and reference speed so that deflections collected at different temperatures and different speeds can be compared. According to the time-temperature superposition principle, the test speed and test temperature can be integrated into a single factor, the effective temperature. On this basis, only the (effective) temperature correction is needed to achieve both temperature and speed correction for raw TSD deflections. In addition, this study also investigated the possibility of avoiding temperature correction by artificially presetting the TSD speed, i.e., the TSD deflection collected at the preset test speed and test temperature is equal to the TSD deflection at the reference speed and reference temperature. Based on the analyses presented, the following conclusions are drawn:

- TSD deflections are more sensitive to test temperatures than to test speeds. For normal TSD operating speeds (20-60 mph), a 10 mph increase in test speed is approximately equivalent to a 1°C drop in temperature.
- The essence of speed correction is temperature correction. The FWD-based AASHTO temperature correction method is applicable to D0 of TSD. The effectiveness of the speed correction depends on the estimation of the activation energy of the AC layer. The default value of 200,000 J/mol is a safe estimate of the activation energy.
- It is feasible to avoid temperature correction of TSD deflections by presetting the TSD speed. The activation energy of the AC layer will affect the ability to adapt to temperature variations by presetting the TSD speed. For AC materials with smaller activation energies, this method of presetting test speed can accommodate more temperature variations. In general, the practical preset speed range of 20-60mph can accommodate temperature variations of about 4°C. This is not sufficient to fully accommodate the expected temperature variations in the field. Therefore, the preset speed method is only recommended for short TSD trips.
- For the preset speed method, the recommended reference speed is the median of the feasible TSD speeds (40 mph in this study). In this case, the acceptable temperature is limited to about the reference temperature ± 2°C. The recommended reference temperature is the average test temperature.
- The accuracy of the preset speed method also relies on the estimation of the activation energy. However, the preset speed method always leads to a more accurate TSD basin regardless of how much the activation energy estimate differs from its true value.

References

[1] Alavi, S., LeCates, J. F., & Tavares, M. P. (2008). Falling weight deflectometer usage (No. Project 20-5 (Topic 38-15)).

[2] Flintsch, G. W., Ferne, B., Diefenderfer, B., Katicha, S., Bryce, J., & Nell, S. (2012). Evaluation of traffic-speed deflectometers. Transportation research record, 2304(1), 37-46.

[3] Flintsch, G., Katicha, S., Bryce, J., Ferne, B., Nell, S., & Diefenderfer, B. (2013). Assessment of continuous pavement deflection measuring technologies (No. SHRP 2 Report S2-R06F-RW-1).

[4] Ferne, B. W., Langdale, P., Round, N., & Fairclough, R. (2009). Development of a calibration procedure for the UK highways agency traffic-speed deflectometer. Transportation research record, 2093(1), 111-117.

[5] Muller, W. B., & Roberts, J. (2013). Revised approach to assessing traffic speed deflectometer data and field validation of deflection bowl predictions. International journal of pavement engineering, 14(4), 388-402.

[6] Zhang, M., Zhang, J., Gong, H., Jia, X., Xiao, R., Huang, H., & Huang, B. (2022). Numerical investigation of pavement responses under TSD and FWD loading. Construction and Building Materials, 318, 126014.

[7] Transportation Officials. (1993). AASHTO Guide for Design of Pavement Structures, 1993 (Vol. 1). Aashto.

[8] Chen, D. H., Bilyeu, J., Lin, H. H., & Murphy, M. (2000). Temperature correction on falling weight deflectometer measurements. Transportation research record, 1716(1), 30-39.

[9] Mun Park, H., Kim, Y. R., & Park, S. (2002). Temperature correction of multiload-level falling weight deflectometer deflections. Transportation Research Record, 1806(1), 3-8.

[10] Lukanen, E. O., Stubstad, R., Briggs, R. C., & Intertec, B. (2000). Temperature predictions and adjustment factors for asphalt pavement (No. FHWA-RD-98-085; DBNX94822-D; NTIS-PB2000107444). Turner-Fairbank Highway Research Center.

[11] Tutumluer, E., & Al-Qadi, I. L. (Eds.). (2009). Bearing Capacity of Roads, Railways and Airfields, Two Volume Set: Proceedings of the 8th International Conference (BCR2A'09), June 29-July 2 2009, Unversity of Illinois at Urbana-Champaign, Champaign, Illinois, USA. CRC Press.

[12] Nasimifar, M., Chaudhari, S., Thyagarajan, S., & Sivaneswaran, N. (2020). Temperature adjustment of surface curvature index from traffic speed deflectometer measurements. International Journal of Pavement Engineering, 21(11), 1408-1418.

[13] Elseifi, M. A., & Zihan, Z. U. (2018). Assessment of the traffic speed deflectometer in Louisiana for pavement structural evaluation (No. FHWA/LA. 18/590). Louisiana Transportation Research Center.

[14] Katicha, S., Flintsch, G., & Diefenderfer, B. (2022). Ten Years of Traffic Speed Deflectometer Research in the United States: A Review. Transportation Research Record, 03611981221094579.

[15] Pellinen, T. K. (2001). Investigation of the use of dynamic modulus as an indicator of hot-mix asphalt peformance. Arizona State University.

[16] Pellinen, T. K., Witczak, M. W., & Bonaquist, R. F. (2004). Asphalt mix master curve construction using sigmoidal fitting function with non-linear least squares optimization. In Recent advances in materials characterization and modeling of pavement systems (pp. 83-101).

[17] Francken, L. (1998). Bituminous binders and mixes. CRC Press.

[18] Al-Qadi, I. L., Xie, W., & Elseifi, M. A. (2008). Frequency determination from vehicular loading time pulse to predict appropriate complex modulus in MEPDG. Asphalt Paving Technology-Proceedings, 77, 739.

[19] ARA (Applied Research Associates). Guide for mechanistic- empirical design of new and rehabilitated pavement structures. Washington, DC: Transportation Research Board of the National Academies.; 2004.

[20] Fu, G., Zhao, Y., Zhou, C., & Liu, W. (2020). Determination of effective frequency range excited by falling weight deflectometer loading history for asphalt pavement. Construction and Building Materials, 235, 117792.

[21] Nitharsan, R. (2011). Development of windows-based version of the 3d-move analysis software for pavement response analysis. University of Nevada, Reno.

[22] Qu, M., Wan, J., & Hao, X. (2014). Analysis of diurnal air temperature range change in the continental United States. Weather and Climate Extremes, 4, 86-95.

Appendix

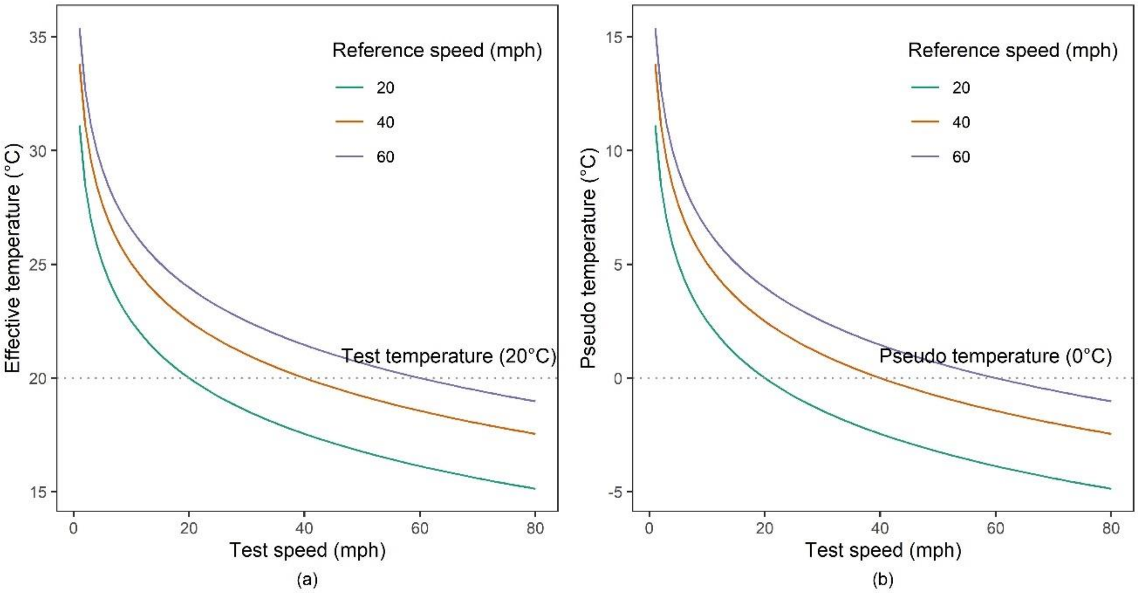

Figure 2-1. The effect of reference speed on: (a) effective temperature; (b) pseudo temperature

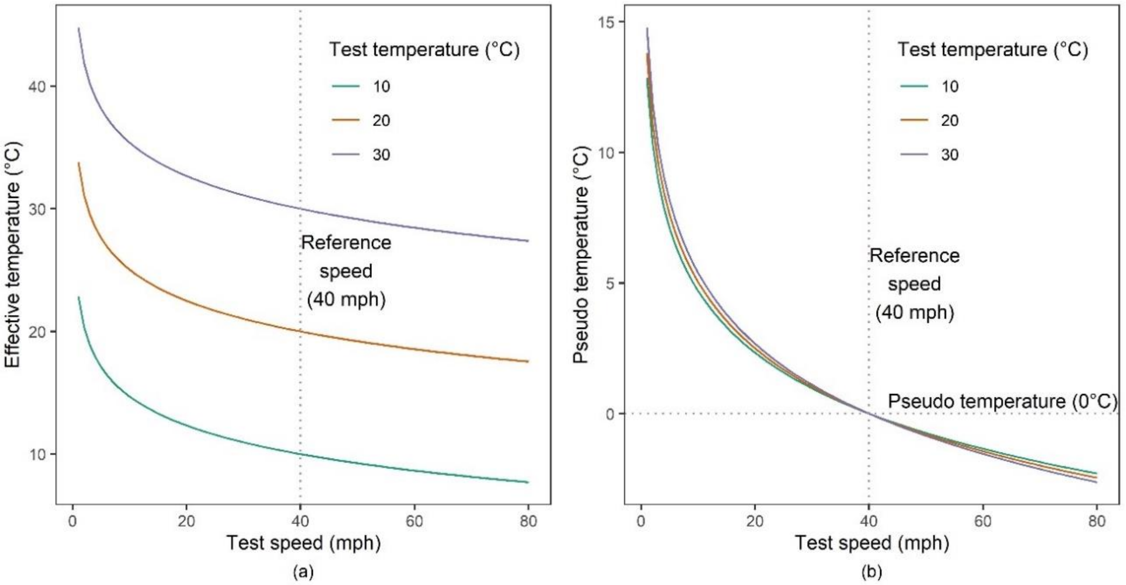

Figure 2-2. The effect of test temperature on: (a) effective temperature; (b) pseudo temperature

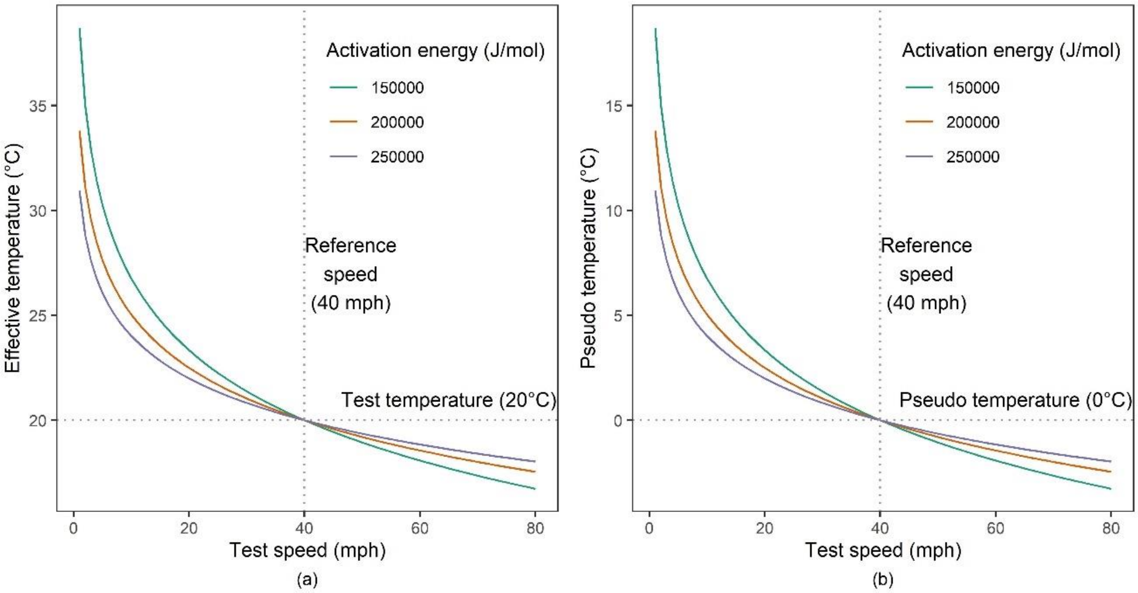

Figure 2-3. The effect of activation energy on: (a) effective temperature; (b) pseudo temperature

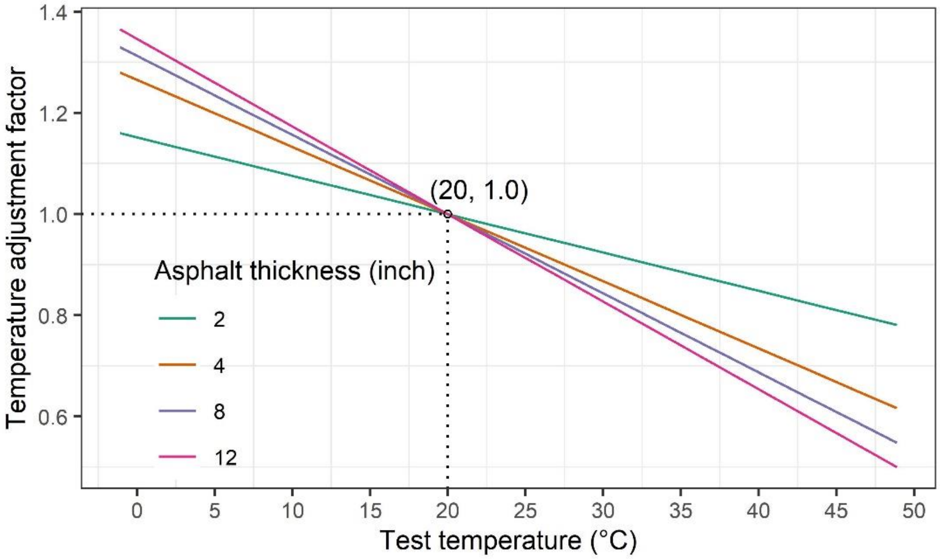

Figure 2-4. Temperature adjustment factor (AASHTO)

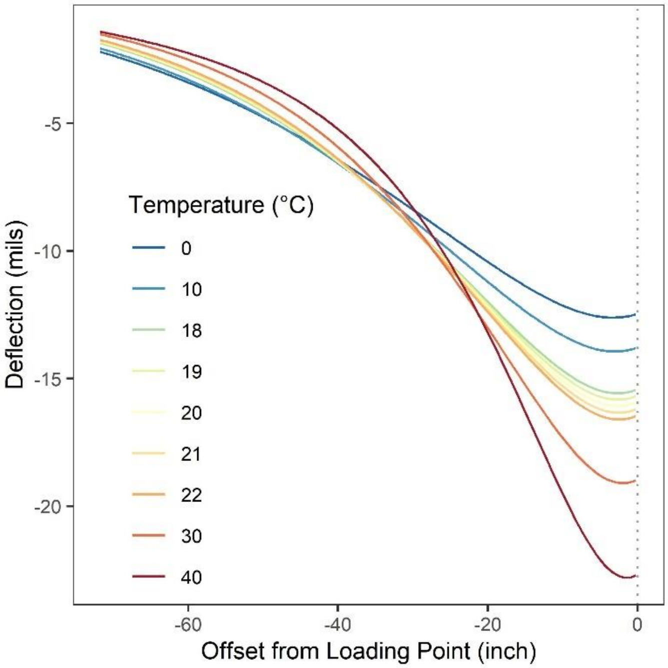

Figure 2-5. Theoretical TSD deflections at different test temperatures

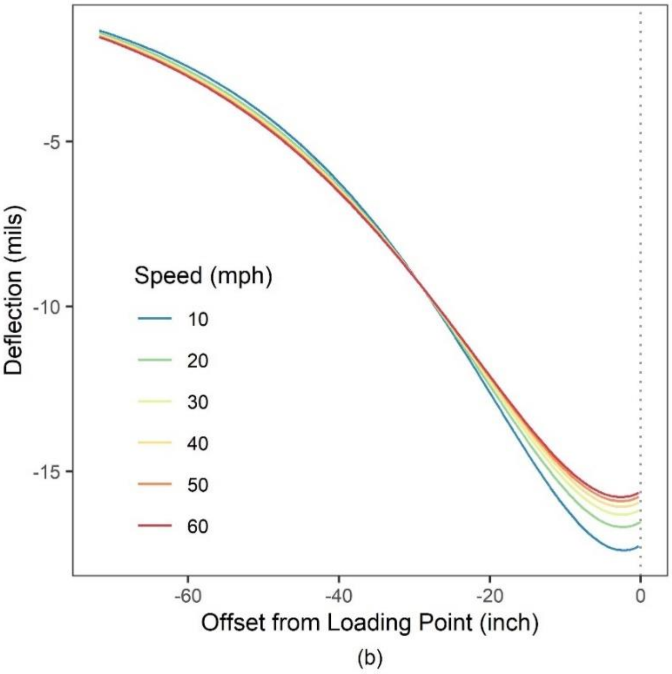

Figure 2-6. Theoretical TSD deflections at different test speeds

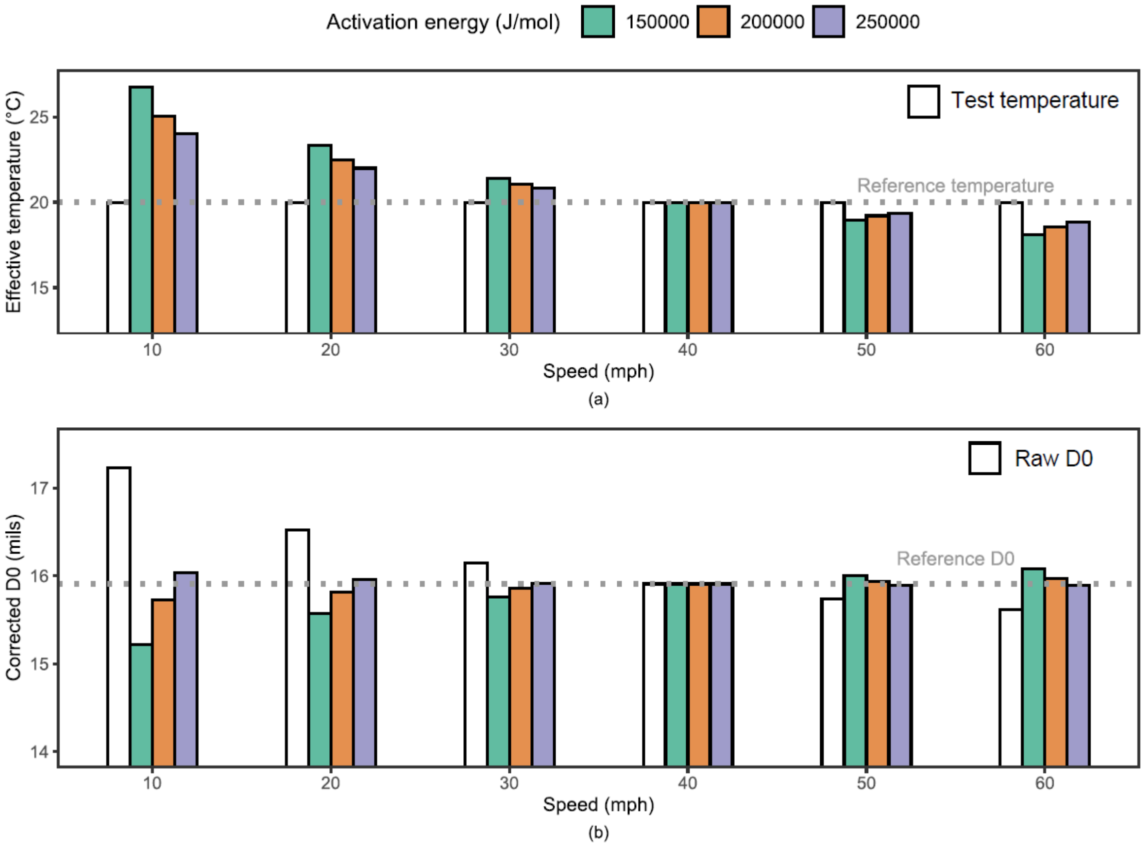

Figure 2-7. The effect of activation energy on speed correction: (a) effective temperature; (b) corrected D0

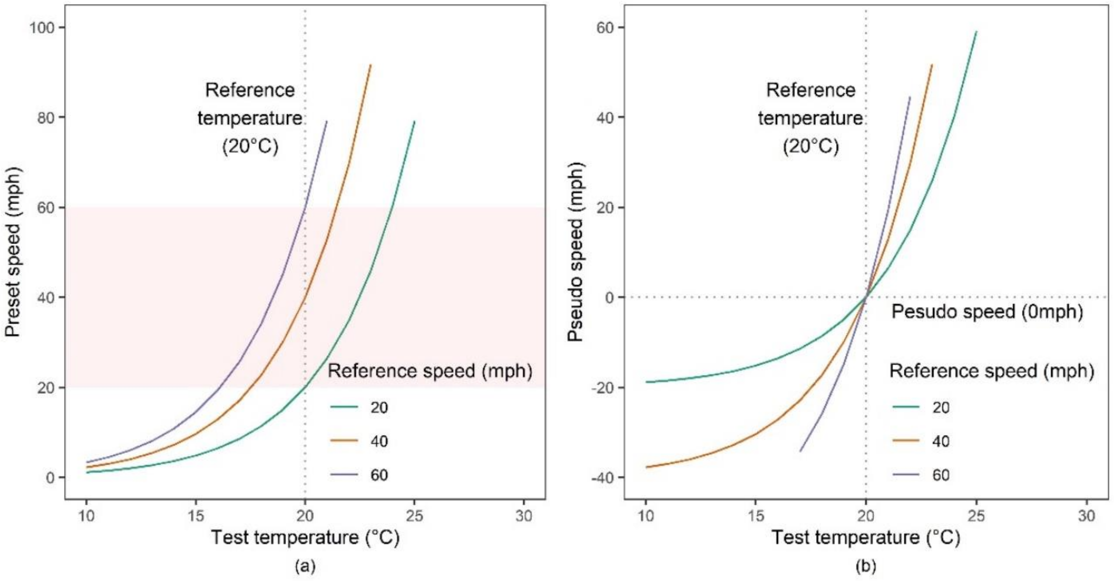

(a) (b)

Figure 2-8. The effect of reference speed on: (a) preset speed; (b) pseudo speed

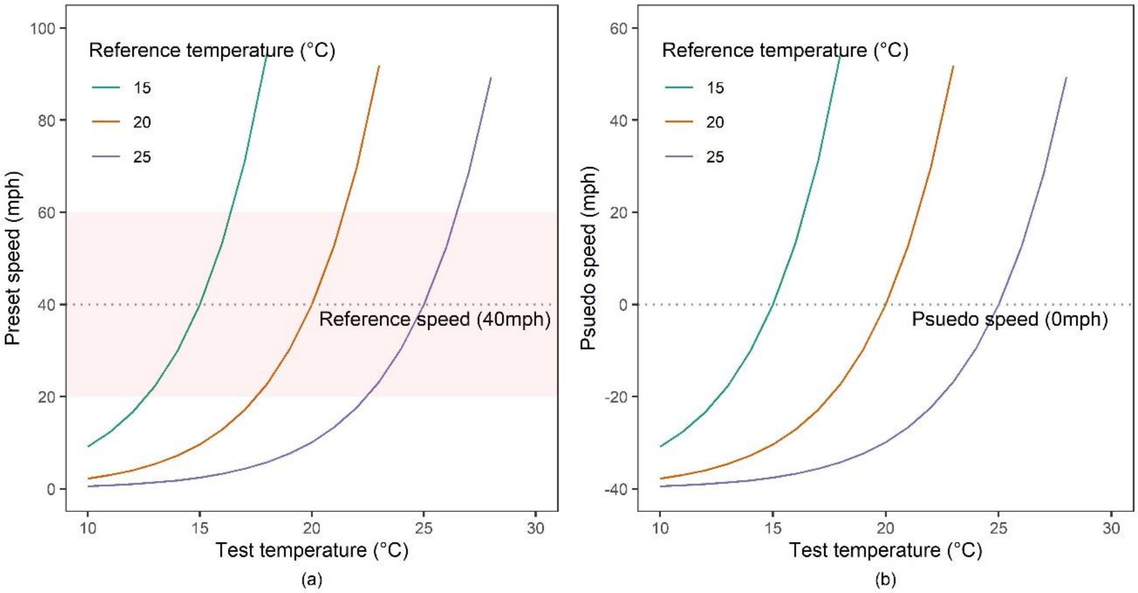

(a) (b)

Figure 2-9. The effect of reference temperature on: (a) preset speed; (b) pseudo speed

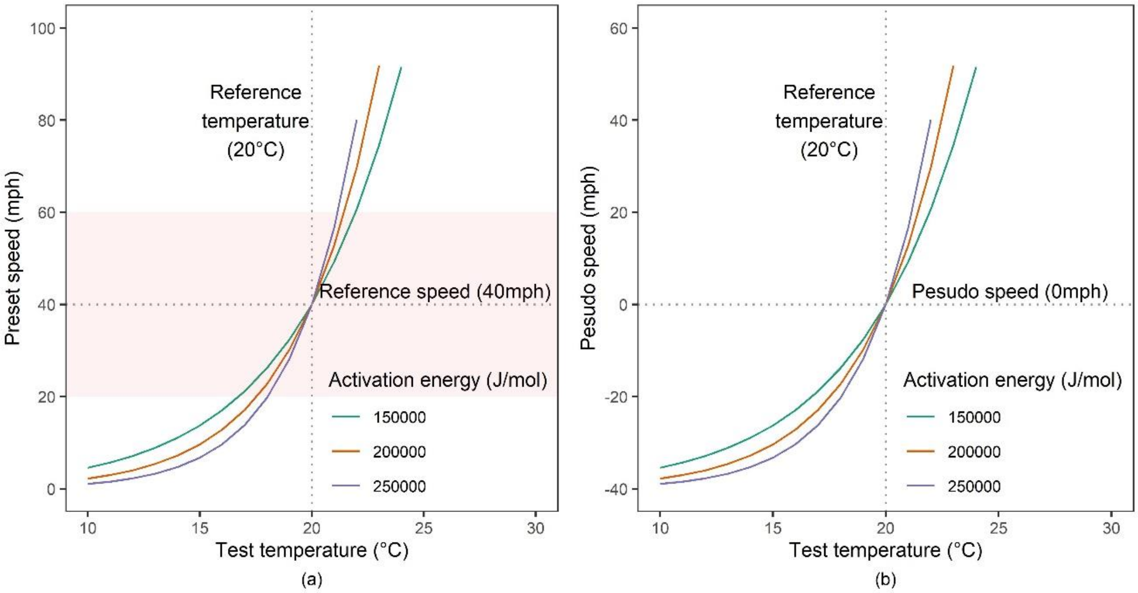

Figure 2-10. The effect of activation energy on: (a) preset speed; (b) pseudo speed

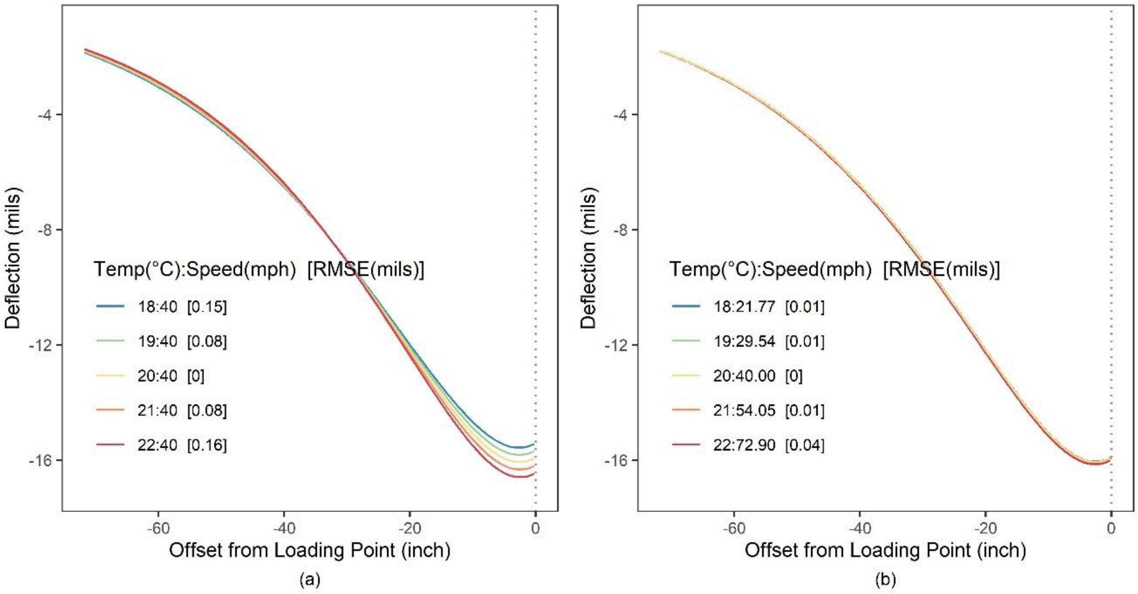

Figure 2-11. Theoretical TSD deflection basin at different test temperatures: (a) at the reference speed of 40 mph; (b) at the preset speed.

Table 2-1. Pavement structure design

Layers	Thickness (inch)	Modulus (ksi)	Poisson’s ratio	Damping ratio
AC	8	-	0.30	25%
Base	9	30	0.35	0
Subgrade	-	20	0.40	0

Table 2-2. Temperature correction for D0 of TSD (AASHTO)

Test temperature (°C)	0	10	18	19	**20**	21	22	30	40
Raw D0 (mils)	12.46	13.78	15.41	15.66	**15.91**	16.17	16.44	18.94	22.66
Raw error (mils)	3.45	2.13	0.50	0.25	**0**	0.26	0.53	3.03	6.75
Corrected D0 (mils)	16.35	15.93	15.89	15.90	**15.91**	15.89	15.87	15.66	14.81
Corrected error (mils)	0.44	0.02	0.02	0.01	**0**	0.02	0.04	0.25	1.10

Table 2-3. Speed correction for D0 of TSD

Case 1: Constant test temperature (20°C): speed correction only							
Test speed (mph)	10	20	30	**40**	50	60	70
Test temperature (°C)	20	20	20	**20**	20	20	20
Raw D0 (mils)	17.23	16.53	16.15	**15.91**	15.74	15.61	15.52
Raw error (mils)	1.32	0.62	0.24	**0**	0.17	0.30	0.39
Effective temperature (°C)	24.66	22.31	20.96	**20**	19.26	18.66	18.16
Corrected D0 (mils)	15.84	15.86	15.88	**15.91**	15.92	15.94	15.96
Corrected error (mils)	0.07	0.05	0.03	**0**	0.01	0.03	0.05
Case 2: Different test temperatures: both temperature and speed correction							
Test speed (mph)	10	20	30	**40**	50	60	70
Test temperature (°C)	0	10	19	**20**	21	30	40
Raw D0 (mils)	12.85	14.14	15.89	**15.91**	15.99	18.47	21.82
Raw error (mils)	3.06	1.77	0.02	**0**	0.08	2.56	5.91
Effective temperature (°C)	4.04	12.16	19.95	**20**	20.26	28.57	37.90
Corrected D0 (mils)	16.06	15.87	15.90	**15.91**	15.92	15.73	15.06
Corrected error (mils)	0.15	0.04	0.01	**0**	0.01	0.18	0.85

Table 2-4. Preset speeds for different activation energy estimates

Activation energy (J/mol)	Test temperature (°C)	18	19	**20**	21	22
-	Reference speed (mph)	40	40	**40**	40	40
	Deflection RMSE (mils)	0.15	0.08	**0**	0.08	0.16
150,000	Preset speed (mph)	26.21	32.40	**40**	49.31	60.69
	Deflection RMSE (mils)	0.05	0.03	**0**	0.03	0.06
200,000	Preset speed (mph)	22.77	30.21	**40**	52.86	69.73
	Deflection RMSE (mils)	0.02	0.01	**0**	0.01	0.05
250,000	Preset speed (mph)	19.77	28.16	**40**	56.69	80.14
	Deflection RMSE (mils)	0.02	0.01	**0**	0.01	0.04

CHAPTER 3

DETERMINING PAVEMENT STRUCTURAL NUMBER WITH TRAFFIC SPEED DEFLECTOMETER MEASUREMENTS

A version of this chapter was published by Miaomiao Zhang, Hongren Gong, Xiaoyang Jia, Xi Jiang, Ning Feng, and Baoshan Huang:

Zhang, M., Gong, H., Jia, X., Jiang, X., Feng, N., & Huang, B. (2022). Determining pavement structural number with traffic speed deflectometer measurements. Transportation Geotechnics, 35, 100774.

My contributions were conducting literature reviews, performing numerical simulations, building machine learning models, and writing the text contained in the paper. Dr. Hongren Gong, Dr. Xiaoyang Jia, Dr. Xi Jiang, Dr. Ning Feng, and Dr. Baoshan Huang provided ideas, guidance, and comments throughout the whole research and offered editorial assistance with the text.

Abstract

Traffic Speed Deflectometer (TSD) overcomes the slow operating speed of the conventional Falling Weight Deflectometer (FWD), but it also introduces new difficulties in estimating the effective structural number (SN) of existing pavements. Due to the different loading mechanisms of TSD and FWD, the FWD-based SN calculation procedure proposed in the AASHTO pavement design guide is incompatible with TSD measurements. To match the existing FWD-based SN records, the authors proposed a new approach to determine the SN with TSD measurements by modifying the AASHTO method. Simulation results show that the difference in AASHTO SN between TSD and FWD essentially came from the difference in the equivalent loading frequency, and the asphalt concrete (AC) layer exhibited lower stiffness under TSD than under FWD. The TSD-based AASHTO SN was generally smaller than the FWD-based AASHTO SN (error of 0.74), and the deviation increased with increasing AC thickness. Therefore, an enhanced AASHTO method was proposed for calibrating TSD-based SN by the AC thickness, which made great progress in estimating SN from TSD deflections with an error reduced to 0.17. The proposed method was verified by filed TSD and FWD measurements and was recommended for pavements with AC thickness greater than 4 inches.

Introduction

Pavement evaluation is an essential step to assess pavement functional and structural conditions, guide routine data monitoring, and select appropriate maintenance measures. The functional conditions are related to pavement roughness and driving quality, while structural conditions deal with the pavement's ability to withstand traffic loads and climate conditions [1]. The pavement structural number (SN) is a frequently used index of pavement structural strength due to its applicability to various material types and environmental conditions [2]. SN is a function of layer thickness, layer coefficient (a function of structural strength, which can be expressed by its elastic modulus), and layer drainage coefficient. SN was first defined by the AASHO Road Test [3] and has been embedded in pavement design procedures of organizations such as AASHTO [4] and the Transport and Road Research Laboratory [5].

Traditionally, the SN of existing pavement structures is estimated from its layer thickness and laboratory-determined material properties, which is destructive, expensive, and not always suitable for large-scale applications [6]. The 1993 AASHTO design guide introduced an approach to determine the pavement effective SN by non-destructive testing (NDT) [4], the Falling Weight Deflectometer (FWD) testing, which has become a prevailing method for assessing pavement structural conditions at the project-level [7]. Many highway agencies use FWD (for pavement deflections), supplemented by ground-penetrating radar (GPR, for layer thickness), to assess the structural performance of existing pavements [8]. As of 2008, FWD testing is routinely conducted in more than 90% of U.S. states [7].

However, issues such as time, expenses, and traffic control hinder FWD testing at the network-level, and the Traffic Speed Deflectometer (TSD) addresses these problems well. TSD is a continuous deflectometer operating at normal traffic speeds and is therefore an efficient and cost-effective test to characterize the pavement structural strength [9]. Field data suggested that TSD measurements had adequate repeatability. In addition, TSD measurements were broadly comparable to FWD measurements, although there were significant differences [10]. Currently, state highway agencies have been exploring the use of the TSD in network-level pavement evaluation [11–13].

One of the main applications of TSD is to estimate the pavement's effective SN and to identify structurally weak spots. The SN calculated from TSD measurements should be comparable to the existing FWD-based SN records. There is currently no satisfactory method to determine the pavement SN using TSD measurements. Engineers generally convert TSD measurements to equivalent FWD values [11] or directly use the FWD-based AASHTO method [8]. Zihan et al. [14] proposed a regression model to estimate SN from TSD measurements collected in Louisiana and Idaho, but the regression model developed from a small number of measurements hindered its practical application on a large scale. Nasimifar et al. [15] used numerical simulation results to calibrate Rohde's empirical equation [6] for TSD-based SN, and field validation showed that the validity of the proposed equation was affected by the thickness estimate. The TSD-based SN calculated from the core-estimated layer thickness was more accurate than that calculated from the GPR-estimated thickness. In contrast to Rohde's empirical equation, the AASHTO procedure for SN calculation is a mechanistic-empirical method, and the TSD calibration based on the AASHTO method will help to understand the underlying mechanism of the SN differences derived from TSD and FWD. In addition, the AASHTO procedure is the most common method used by state highway agencies to estimate pavement SN [8], and calibration equations based on it will be more widely and easily applied. Therefore, it is necessary to calibrate the FWD-based AASHTO method to make it more applicable to TSD deflections.

A universal and reliable calibration method should be based on a comprehensive TSD database containing various pavement structures. Building such a diverse database from field data is laborious and expensive, and researchers often prefer analytical methods [16,17]. Compared to the more complicated finite-element method, the 3D-Move program developed by the University of Nevada, Reno [18] was considered an efficient tool to simulate moving loads [19], and the theoretical deflection output of the 3D-Move has been verified by field data [11,20].

The objective of this study was to develop a new approach to determine the SN with TSD measurements by modifying the AASHTO method so that the improved TSD-based SN can be comparable to the existing FWD-based SN records. Mechanistic simulation models were developed based on the 3D-Move program to simulate the loading mechanisms associated with TSD and FWD and to obtain a deflection database of a wide range of pavement structures. The TSD and FWD data collected at in-service pavement sections were then used to validate the proposed method.

AASHTO Procedure for SN Calculation

The FWD-based SN calculation procedure proposed in the 1993 AASHTO Pavement Design Guide is widely used in pavement maintenance and rehabilitation to evaluate the structural capacity of existing pavements [4]. With the total thickness of pavement layers and the effective pavement modulus, the effective SN can be obtained with the following Equation:

$$SN = 0.0045 * D * \sqrt[3]{E_p} \tag{1}$$

where D is the total pavement thickness above the subgrade, inches; Ep is the effective pavement modulus of all layers above the subgrade, psi; SN is the effective structural number.

The effective pavement modulus represents the overall strength of pavement layers above the subgrade. The effective pavement modulus can be obtained through the back-calculation analysis of deflections, as well as the subgrade resilient modulus, as shown in Equation (2)-(5).

$$M_r = \frac{0.24P}{x * d_x} \tag{2}$$

where M_r is the subgrade resilient modulus, psi; P is applied load, pounds; μ is Poisson's ratio; x is subgrade radius, the radial distance at which the deflection is measured, inches; d_x is measured deflection at a radial distance of x, inches.

Given the subgrade resilient modulus and the total thickness of the pavement structure, the effective modulus can be calculated from the deflection measured at the center of the load plate.

$$d_0 = \frac{1.5*p*a}{M_r}\left[\frac{1}{\sqrt{1+\left(\frac{D}{a}\sqrt[3]{\frac{Ep}{M_r}}\right)^2}} + \frac{\left(1-\frac{1}{\sqrt{1+\left(\frac{D}{a}\right)^2}}\right)}{\frac{Ep}{M_r}}\right] \tag{3}$$

where d0 is the deflection at the center of the load plate, inches. p is the contact pressure, psi. a is the radius of load plate, inches; M_r is the subgrade resilient modulus, psi; D is the total pavement thickness above the subgrade, inches; Ep is the effective pavement modulus of all layers above the subgrade, psi.

The calculation of the subgrade resilient modulus is based on the assumption that, at a point sufficiently far from the loading center, the measured surface deflection is almost entirely due to the deformation in the subgrade [21]. In practical applications, the point must be far enough from the loading center so that the subgrade modulus can be estimated well without being affected by the above layers. It should also be as close to the loading center as possible so that the deflection is not too small to be measured accurately. AASHTO recommends that the subgrade radius x in Equation (2) should be greater than 0.7 of the effective radius, which can be determined from the following relationship:

$$x \geq 0.7\ a_e \tag{4}$$

$$a_e = \sqrt{a^2 + (D\sqrt[3]{\frac{E_p}{M_r}})^2} \tag{5}$$

where a_e is the effective radius, the radius of the stress bulb at the subgrade-pavement interface, inches; a is the circular load radius, inches; D is the total pavement layer thicknesses, inches; E_p is the effective modulus of pavement layer, psi; M_r is the subgrade resilient modulus, psi.

The effective radius is calculated based on the “method of equivalent thickness” or MET. For simplicity, the stress distribution for a typical subgrade is assumed to be at 45 degrees. The pavement layers with thickness D and effective modulus E_p can be transformed into an equivalent section with subgrade modulus M_r. The thickness of the transformed section is given by an equivalent thickness h_e.

$$h_e = D\sqrt[3]{\frac{E_p}{M_r}} \tag{6}$$

where E_p is the effective modulus of pavement layer, psi; M_r is the subgrade resilient modulus, psi; D is the total pavement layer thicknesses, inches.

Numerical Simulation

A general and reliable SN calibration method should be applicable to various pavement structures. However, a database of field TSD deflections from a wide range of pavements is not currently available, and key pavement structure information (e.g., layer thickness) is often lacking in field data collection. In addition, field data are always affected by temperature, traffic conditions in adjacent lanes, TSD speed, etc. Calibration models based on field data may introduce unnecessary errors. Therefore, in this study, the numerical simulation method was preferred to develop the calibration model. A database of 243 different three-layer pavement structures was considered in terms of three levels of asphalt concrete (AC), base modulus, subgrade modulus, AC thickness, and base thicknesses, as presented in Table 3-1 (all tables and figures are located in the Appendix). Figure 3-1 shows the dynamic modulus curves of three plant-produced AC materials considered in this study at the reference temperature (68 °F) [22].

3D-Move simulation

The 3D-Move program was used to simulate the loading mechanism related to TSD and FWD, so as to obtain the corresponding theoretical deflections. In this study, all loading mechanisms of the TSD were based on the Intelligent Pavement Assessment Vehicle (iPAVe) operated by the Australian Road Research Board (ARRB) group Inc. The iPAVe is a fully integrated survey vehicle that collects structural and functional pavement condition data at traffic speeds. Table 3-2 summarizes the notable simulation parameters for TSD and FWD.

Loading characteristics

In the 3D-Move simulation, FWD was statically loaded using a single circular plate with a radius of 5.904 inches. A typical FWD load is nominally 9,000 pounds with a contact pressure of 82.2 psi [11]. The dynamic effects of FWD loading were considered through material properties (discussed below), while the inertia and damping of the pavement were neglected.

For the TSD simulation, the moving speed was set to 40 mph. As shown in Figure 3-2(a), the TSD load shape was simplified to a uniformly distributed dual circular load. For the TSD-based SN calculation, the area-equivalent single circular load (Figure 3-2(b)) will be used, since the AASHTO SN calculation procedure assumes a single circular load.

The actual TSD load magnitude varies continuously during the TSD trip due to varying pavement conditions. TSD continuously records the applied axle load during the test, and the raw TSD measurements should be corrected to a standard load level before any analysis is performed. In this study, the same contact pressure as FWD (82.2 psi with a load magnitude of approximately 11,660 pounds) was used to eliminate the effect of load magnitude, thus facilitating comparisons between FWD and TSD. Due to the homogeneity of the linear viscoelastic material, the TSD deflection is proportional to the load magnitude, and the TSD load magnitude of 82.2 psi does not affect the back-calculation and SN calculation.

Material properties

The AASHTO procedure for SN calculation is based on linear elastic materials. For static FWD (moving speed of zero), only linear elastic materials are applicable in the 3D-Move program. Therefore, in FWD models, all pavement layers were defined as linear elastic materials. For the rate-dependent AC materials, the single dynamic modulus corresponding to the FWD equivalent loading frequency (16.7 Hz) was used [23,24], as listed in Table 3-1. The equivalent loading frequency is described in detail by Zhang et al [25].

For the moving TSD, it has been shown that pavement responses under moving loads were more sensitive to the viscoelasticity of the AC layer [26]. In TSD models, the AC layer was defined as a linear viscoelastic material, and the dynamic modulus curve was fed into the 3D-Move program. The AC layer was characterized by the rate-dependent modulus with a damping ratio of 25%.

Simulation results and discussions

Based on the 3D-Move simulation results, 243 deflection basin pairs for TSD and FWD were obtained. To find out the underlying different mechanism of AASHTO SN derived from TSD and FWD, the deflection results under TSD and FWD should be compared. The deflection at the location x inches from the loading point was defined as Dx. Figure 3-3 shows the deflection comparison between TSD and FWD.

The deflection at the loading center (D0) is the most important deflection indicator, which represents the strength of the overall pavement structure. There are many reasons for the difference in D0 between TSD and FWD. For example, when other loading conditions are consistent, the dual circular loading shape of TSD leads to a lower D0. The inertial damping and the AC viscoelasticity would result in a time difference between the time when the TSD crosses over the point and the time when the maximum response occurs [27]. Unlike FWD, the D0 of TSD is not the maximum deflection.

However, it can be found from Figure 3-3(a) that under the same contact pressure, the D0 of TSD was always greater than the D0 of FWD. In addition to the different loading radius of TSD and FWD (equivalent to 6.72 inches vs. 5.904 inches, which would result in a greater D0 of TSD but would not affect the back-calculation of layer modulus), a more important reason is the different equivalent loading frequency of FWD and TSD. Studies have shown that the equivalent loading frequency of TSD (moving at 40 mph) is about 2.6 Hz [25], which is lower than that of FWD (16.7 Hz). Due to the rate-dependent viscoelastic nature of the AC layer, the AC layer exhibits lower stiffness under TSD than under FWD. The surface curvature index (SCI) of the AC layer (SCI12, the difference between D0 and D12) is an important indicator of the strength of the AC layer. As shown in Figure 3-3(b), the SCI12 of TSD was greater than that of FWD, which may also come from the lower stiffness of the AC layer under TSD.

The surface curvature index of the subgrade (SCI_subgrade, the difference between D36 and D60) is often used to reflect the strength of the subgrade. Figure 3-3(c) shows that the SCI_subgrade of TSD was always greater than that of FWD, which can also be explained by the different loading frequency. Compared to FWD, the AC layer tend to exhibit lower stiffness under TSD (lower loading frequency), and therefore, the subgrade is more heavily loaded and is expected to deform more.

It should be noted that the equivalent loading frequency of TSD was not assumed in the TSD simulation, and the viscoelasticity of the AC layer was represented by its dynamic modulus curve. The Fourier transform technology and frequency domain solutions adopted in 3D-Move enable the direct use of the frequency swept dynamic modulus in the analysis. The description of TSD equivalent loading frequency was only an explanation of the underlying mechanism of different AC behavior under TSD and FWD.

Sensitivity analysis

The influence of pavement structure variations on pavement deflections was also studied. An illustration of AC surface deflection basin for varying pavement structures is shown in Figure 3-4. The default AC material, base modulus, subgrade modulus, AC thickness, and base thickness were level 1, 30 ksi, 15 ksi, 8 inches, and 9 inches, respectively. Obviously, the greater the stiffness or thickness, the smaller the deflection, as weaker pavement structures would result in greater deflections. The deflection was more sensitive to variations in subgrade modulus and AC thickness, but it was insensitive to the base layer. Therefore, both TSD and FWD deflections can be used to detect weak asphalt layers and weak subgrade, but they are not effective in detecting the damage in the base layer.

The deflection at locations close to the loading center was more sensitive to different pavement structural factors, while the deflection at locations far from the loading center was almost exclusively related to the subgrade modulus. It confirmed the assumption that at a location sufficiently far from the loading center, the deflection of the AC surface (the cumulative deformation of all layers) was almost entirely due to deformation in the subgrade. Overall, the sensitivity of FWD deflections and TSD deflections to different pavement structure factors was almost the same.

In addition to the deflection itself, the deflection basin shape can also provide some useful information. At locations close to the loading center, the deflection of TSD was greater than that of FWD, while at locations far from the loading center, the opposite occurred. As a result, the deflection basins of TSD were steeper than those of FWD, and they crossed each other at about 48 inches from the loading center. The deflection basin shape depends on the stress distribution among different layers. Consider a series of pavement structures with the same subgrade modulus and the same upper layer thickness, but with different upper layer stiffness. Structures with softer upper layers will have narrower vertical stress distributions and therefore steeper basins. In contrast, structures with stiffer upper layers will have flatter deflection basins. Therefore, the steeper basin shape of TSD also came from the relatively lower loading frequency of TSD (lower stiffness of the AC layer under TSD).

Determining SN from Theoretical TSD Deflections

AASHTO back-calculation analysis

After obtaining the 243 theoretical TSD and FWD deflection basin pairs, the back-calculation analysis (Equation (2) – (5)) was performed on each deflection pair according to the 1993 AASHTO Pavement Design Guide. For different pavement structures, subgrade radius, subgrade resilient modulus (AASHTO M_r), and effective pavement modulus (AASHTO E_p) derived from TSD and FWD can be obtained, respectively. The difference between TSD and FWD was evaluated by the Root Mean Squared Error (RMSE) in the following form:

$$RMSE = \sqrt{\frac{1}{n}\sum_{k=1}^{n}(y_k - \hat{y}_k)^2} \tag{7}$$

where y_k is the value derived from TSD deflections, $\hat{y}_k$ is the value derived from FWD deflections.

Subgrade radius in this study was defined as the radial distance of the deflection used for subgrade resilient modulus calculation in Equation (2). In the engineering practice of deflection collections, deflections are typically recorded at the following locations: 0, 12, 18, 24, 36, 48, and 60 inches from the loading center. Therefore, the subgrade radius should be selected from these specific locations (generally starting at 24 inches). The detailed process of SN calculation is:

Step 1: Input the layer thickness, deflection, and its position (offset). Set the subgrade radius to 24 inches.

Step 2: Calculate the subgrade resilient modulus based on the deflection at the subgrade radius using Equation (2).

Step 3: Calculate the effective pavement modulus based on D0 and the subgrade resilient modulus (calculated in Step 2) using Equation (3).

Step 4: Check whether the subgrade radius meets the requirements of Equation (4) and (5). If yes, stop; otherwise, go to Step 5.

Step 5: Update the subgrade radius to a greater one (among 24”, 36”, 48”, and 60”), then go to Step 2.

Subgrade radius

Figure 3-5(a) compares the subgrade radius of TSD and FWD of different pavement structures. It can be found that there were 4 different FWD subgrade radius (24”, 36”, 48” and 60”) and 3 different TSD subgrade radius (24”, 36” and 48”) for these 243 pavement structures. When the TSD subgrade radius was 24 inches, the FWD subgrade radius could be 24 inches and 36 inches. When the TSD subgrade radius was 36 inches, the FWD subgrade radius could be 36 inches, 48 inches, and 60 inches. Similarly, when the TSD subgrade radius was 48 inches, the FWD subgrade radius could be 48 inches and 60 inches. Therefore, the subgrade radius of TSD was generally less than or equal to the subgrade radius of FWD. It is assumed that starting from the subgrade radius, the surface deflection was almost only caused by the deformation in the subgrade and independent of other pavement layers. Therefore, the vertical stress in the pavement layers (above the subgrade) tended to be distributed over a narrower area under TSD loading compared to FWD, which was consistent with the steeper deflection basin of TSD.

Subgrade resilient modulus

The subgrade resilient modulus calculated using TSD deflections and FWD deflections is shown in Figure 3-5(b), which is colored by the assumed value in the simulation. It can be found that the AASHTO subgrade resilient modulus calculated using TSD deflections was always greater than that calculated using FWD deflections (RMSE was 3.04 ksi), and the difference increased with the increase of subgrade modulus. For pavements with stiff subgrades (subgrade modulus greater than 30 ksi), the subgrade resilient modulus back-calculated using FWD deflections was smaller than its assumed value, so the AASHTO back-calculation analysis tended to underestimate the stiff subgrade. For pavements with soft subgrades (subgrade modulus less than 5 ksi), the back-calculated subgrade modulus was greater than its assumed value, and the AASHTO back-calculation analysis tended to overestimate the soft subgrade. Overall, the subgrade resilient modulus calculated from theoretical deflections (both FWD and TSD) was close to its assumed value. It can be expected that the AASHTO subgrade resilient modulus derived from FWD and TSD deflections are both good estimates of the actual subgrade modulus.

Effective pavement modulus

The effective pavement modulus represents the overall strength of pavement layers above the subgrade, and it is a composite modulus that depends mainly on the stiffness of the AC layer and the thickness of the AC layer. It has been shown that AC layers tend to exhibit lower stiffness at TSD (lower loading frequency), so the effective pavement modulus is expected to be smaller for TSD than for FWD. As shown in Figure 3-5(c), the AASHTO effective pavement modulus calculated using TSD deflections was generally smaller than that calculated using FWD deflections (RMSE was 97.09 ksi), and the difference increased with the increase of AC thickness. When the AC thickness was 4 inches, the effective pavement modulus calculated from TSD and FWD deflection was similar. This is because when the AC thickness is small, the smaller equivalent AC modulus under TSD is offset by the effects of dual circular loading and asymmetric basins of TSD. As described in Section 3.2, the dual circular loading shape and asymmetric basin of TSD make the D0 of TSD lower than expected, which may result in a greater than expected effective pavement modulus (back-calculated from D0).

TSD-based SN calibration

The AASHTO SN calculated from theoretical TSD and FWD deflections according to the AASHTO procedure is shown in Figure 3-6(a). Similar to the effective pavement modulus, for most pavement structures, the AASHTO SN calculated using FWD deflections was greater than that calculated using TSD deflections. The SN difference between TSD and FWD increased with the increase of AC thickness. The difference (RMSE) between the two was about 0.74, which meant that the TSD-based AASHTO SN was expected to deviate by 0.74 from the FWD-based AASHTO SN. In pavement rehabilitation and overlay design, the difference in the effective SN estimates may result in a difference in the AC thickness of about 1.85 inches (Equation (8)).

$$D_{ol} = \frac{SN_{ol}}{a_{ol}} \tag{8}$$

where SN_{ol} is the required overlay structural number; a_{ol} is the structural coefficient for the AC overlay, 0.4; D_{ol} is the required thickness of AC overlay, inches.

Linear regression

The existing SN records in the PMS were calculated from FWD deflections, and the TSD-based SN needed to be calibrated to be comparable to the FWD-based values. Linear regression was performed on the TSD-based AASHTO SN to make it closer to the FWD-based AASHTO SN, which has the following form:

$$SN_{linear} = 1.22 * SN_{tsd} - 0.33 \tag{9}$$

where SN_{tsd} is TSD-based AASHTO SN, and SN_{linear} is the TSD-based SN improved by linear regression. It (RMSE was 0.33) was more accurate than the direct application of the AASHTO procedure, but there was still room for improvement.

Calibration by AC thickness

Since the simple linear regression cannot eliminate the difference between the FWD-based SN and TSD-based SN, more complex regression methods or the introduction of other variables were required. A machine learning method, Random Forests (RF), was employed to evaluate which factor was most important in predicting FWD-based SN. RF works by constructing a large number of decision trees during training and outputting them as class patterns (classification) or mean prediction (regression) [28]. As a tree-based learning algorithm, it is convenient to interpret RF models through variable importance information, which describes the relative contribution of the input variables to the prediction.

The RF model was established using FWD-based AASHTO SN as the response variable. The influencing factors involved in the AASHTO SN calculation procedure, combined with the TSD-based AASHTO SN, were used as predictors of the RF model. Considering that the base layer thickness was less available than the AC thickness in the network-level application, the pavement thickness was divided into the AC thickness and the base layer thickness (both of which were used as predictors). The importance ranking of different predictors is shown in Figure 3-6(b). It can be found that the TSD-based AASHTO SN was the most important factor in predicting FWD-based SN. AC thickness also contributed significantly, while other factors had little effect.

For the sake of simplicity, only the most important factors were included in the calibration of the TSD-based SN. Therefore, taking into account the effect of AC thickness, the following form can be obtained:

$$SN_{ac} = 0.81 * SN_{tsd} + 0.19 * H_{ac} - 0.15 \tag{10}$$

where SN_{tsd} is TSD-based AASHTO SN, H_{ac} is the thickness of AC layer, and SN_{ac} is the TSD-based SN calibrated by H_{ac}. The calibration effect of AC thickness is shown in Figure 3-6(c). It can be found that the difference between SN calculated from TSD and FWD deflections has been well corrected, and the RMSE between them was 0.17, which was more accurate than the linear regression.

The testing RMSE of the RF model was also 0.17. Since the RF model was too complex for engineering applications, the RF model in this study was only used as a reference to assess different methods. The accuracy of the TSD-based SN calibrated by AC thickness was very close to that of the RF model, so it was considered to be sufficiently accurate without further improvement.

Summary

In summary, the direct application of the AASHTO method to calculate SN with TSD deflections had a relatively large RMSE of 0.74, while the TSD-based SN improved by linear regression made great progress. The most accurate method for estimating SN with TSD deflections was the SN calibrated by the AC thickness, which had the smallest RMSE of 0.17. Moreover, it can even achieve the same accuracy as the much more complicated RF method, which can be considered sufficiently accurate in terms of its simplicity.

Field Evaluation of Proposed Method

The proposed calibration method was applied to field data to verify its effectiveness. The consistency of the SN calculated from TSD and FWD deflections was evaluated. Based on the field FWD and TSD measurements and layer thickness information presented by Elseifi et al. [11], the effective SN was calculated for five test sites in Louisiana. All deflections were corrected to the reference temperature (68 °F) and the standard load level (82.2 psi). Figure 3-7 shows the SN calculation and calibration results for the five test sites. The AC thickness for each site is also given. It can be found that the direct use of the AASHTO method to calculate SN from TSD deflections had a relatively large error, and the difference (RMSE) between FWD-based AASHTO SN and TSD-based AASHTO SN was about 0.96. Both the linear regression (RMSE was 0.65) and the proposed method of calibration by AC thickness (RMSE was 0.62) improved the estimation of TSD-based SN. However, the improvement of the proposed method was limited, which may be due to the influence of other factors, such as the accuracy of TSD measurements and TSD speed, which need to be further investigated.

In addition, for pavements with a 4-inch AC layer, the proposed calibration method may introduce some errors. The difference between the TSD-based AASHTO SN and the TSD-based SN calibrated by AC thickness was small or even slightly increased. Due to the limited selection of AC thickness in the parametric study, the calibration method is recommended for pavements with AC thickness greater than 4 inches.

Conclusions

The FWD-based AASHTO SN calculation procedure is the most prevailing method to assess the effective SN of existing pavements at the project level. However, issues such as time, cost, and traffic control limit applying FWD at a network level, and state highway agencies have been exploring the use of the TSD at network-level recently. There is currently no satisfactory method to determine the pavement SN from TSD measurements. To make the TSD-based SN comparable with the existing FWD-based SN records, new equations were developed to determine TSD-based SN by modifying the AASHTO method. A database of theoretical TSD and FWD deflections of various pavement structures was developed using 3D-Move program. Based on the analyses presented, the following conclusions were reached:

- There were many reasons for the difference in AASHTO SN calculated using FWD and TSD deflections. In addition to the obviously different loading characteristics (single vs. dual circular load, stationary vs. moving load), a more important but underlying reason was the different equivalent loading frequency of FWD and TSD. Due to the rate-dependent viscoelasticity of the AC layer, the AC layer exhibited lower stiffness under TSD than under FWD.
- The deflection basin of TSD was steeper than that of FWD. The AASHTO subgrade resilient modulus calculated using TSD deflections was always greater than that calculated using FWD deflections, but they were both good estimates of the actual subgrade modulus.
- The TSD-based AASHTO SN was generally smaller than the FWD-based AASHTO SN (RMSE of 0.74), and the deviation was related to the AC thickness. The deviation was insignificant when the AC thickness was 4 inches and increased as the AC thickness increased.

- An enhanced AASHTO method was proposed for calibrating TSD-based SN by the AC thickness. The proposed method provided the most accurate TSD-based SN estimates, with an RMSE of 0.17. Compared with more complicated methods such as random forests, the proposed method attained comparable accuracy while having a substantially simplified form.
- The proposed method was verified by field TSD and FWD measurements and was recommended for pavements with AC thickness greater than 4 inches.

References

[1] Elseifi, M.A., Gaspard, K., Wilke, P.W., Zhang, Z. and Hegab, A., 2015. Evaluation and validation of a model for predicting pavement structural number with rolling wheel deflectometer data. Transportation Research Record, 2525(1), pp.13-19.

[2] Kim, M.Y., Kim, D.Y. and Murphy, M.R., 2013. Improved method for evaluating the pavement structural number with falling weight deflectometer deflections. Transportation research record, 2366(1), pp.120-126.

[3] Board, H., 1962. The AA. SH, O Road Test.

[4] Highway, A. and Officials, T., 1993. AASHTO Guide for Design of Pavement Structures, 1993.

[5] Zofka, A., Sudyka, J., Maliszewski, M., Harasim, P., & Sybilski, D. (2014). Alternative approach for interpreting traffic speed deflectometer results. Transportation Research Record, 2457(1), 12-18.

[6] Rohde, G.T., 1994. Determining pavement structural number from FWD testing. Transportation Research Record, (1448).

[7] Alavi, S., LeCates, J.F. and Tavares, M.P., 2008. Falling weight deflectometer usage (No. Project 20-5 (Topic 38-15)).

[8] Maser, K., Schmalzer, P., Shaw, W. and Carmichael, A., 2017. Integration of Traffic Speed Deflectometer and Ground-Penetrating Radar for network-level roadway structure evaluation. Transportation Research Record, 2639(1), pp.55-63.

[9] Flintsch, G.W., Ferne, B., Diefenderfer, B., Katicha, S., Bryce, J. and Nell, S., 2012. Evaluation of traffic-speed deflectometers. Transportation research record, 2304(1), pp.37-46.

[10] Flintsch, G., Katicha, S., Bryce, J., Ferne, B., Nell, S. and Diefenderfer, B., 2013. Assessment of continuous pavement deflection measuring technologies (No. SHRP 2 Report S2-R06F-RW-1).

[11] Elseifi, M.A., Zihan, Z.U. and Icenogle, P., 2019. A Mechanistic Approach to Utilize Traffic Speed Deflectometer (TSD) Measurements into Backcalculation Analysis (No. FHWA/LA. 17/612). Louisiana State University. Department of Civil and Environmental Engieering.

[12] Nasimifar, M., Thyagarajan, S. and Sivaneswaran, N., 2017. Backcalculation of flexible pavement layer moduli from traffic speed deflectometer data. Transportation Research Record, 2641(1), pp.66-74.

[13] Katicha, S.W., Flintsch, G.W., Ferne, B. and Bryce, J., 2014. Limits of agreement method for comparing TSD and FWD measurements. International Journal of Pavement Engineering, 15(6), pp.532-541.

[14] Uddin Ahmed Zihan, Z., Elseifi, M. A., Gaspard, K., & Zhang, Z. (2018). Development of a structural capacity prediction model based on traffic speed deflectometer measurements. Transportation research record, 2672(40), 315-325.

[15] Nasimifar, M., Thyagarajan, S., Chaudhari, S., & Sivaneswaran, N. (2019). Pavement structural capacity from traffic speed deflectometer for network level pavement management system application. Transportation Research Record, 2673(2), 456-465.

[16] Mabrouk, G. M., Elbagalati, O. S., Dessouky, S., Fuentes, L., & Walubita, L. F. (2022). Using ANN modeling for pavement layer moduli backcalculation as a function of traffic speed deflections. Construction and Building Materials, 315, 125736.

[17] Mabrouk, G. M., Elbagalati, O. S., Dessouky, S., Fuentes, L., & Walubita, L. F. (2021). 3D-finite element pavement structural model for using with traffic speed deflectometers. International Journal of Pavement Engineering, 1-15.

[18] Siddharthan, R.V., Yao, J. and Sebaaly, P.E., 1998. Pavement strain from moving dynamic 3D load distribution. Journal of Transportation Engineering, 124(6), pp.557-566.

[19] Huhtala, M. and Pihlajamaki, J., 1992. New concepts on load equivalency measurements. In International Conference on Asphalt Pavements, 7th, 1992, Nottingham, United Kingdom (Vol. 3).

[20] Nasimifar, M., Siddharthan, R. V., Rada, G. R., & Nazarian, S. (2017). Dynamic analyses of traffic speed deflection devices. International Journal of Pavement Engineering, 18(5), 381-390.

[21] Rohde, G. T., & Scullion, T. (1990). MODULUS 4.0: Expansion and validation of the MODULUS backcalculation system.

[22] Huang, B., Shu, X., & Bass, J. (2008). Investigation of simple performance characteristics of plant-produced asphalt mixtures in Tennessee. Transportation Research Record, 2057(1), 140-148.

[23] Lytton, R. L. (1990). Determining asphaltic concrete pavement structural properties by nondestructive testing (No. 327). Transportation Research Board.

[24] Siddharthan, R. V., Krishnamenon, N., & Sebaaly, P. E. (2000). Finite-layer approach to pavement response evaluation. Transportation Research Record, 1709(1), 43-49.

[25] Zhang, M., Zhang, J., Gong, H., Jia, X., Xiao, R., Huang, H., & Huang, B. (2022). Numerical investigation of pavement responses under TSD and FWD loading. Construction and Building Materials, 318, 126014.

[26] Wu, C., Wang, H., Zhao, J., Jiang, X., & Qiu, Y. (2020). Asphalt pavement modulus backcalculation using surface deflections under moving loads. Computer‐Aided Civil and Infrastructure Engineering, 35(11), 1246-1260.

[27] Rada, G. R., Nazarian, S., Visintine, B. A., Siddharthan, R. V., & Thyagarajan, S. (2016). Pavement structural evaluation at the network level.

[28] Breiman, L., Friedman, J. H., Olshen, R. A., & Stone, C. J. (2017). Classification and regression trees. Routledge.

Appendix

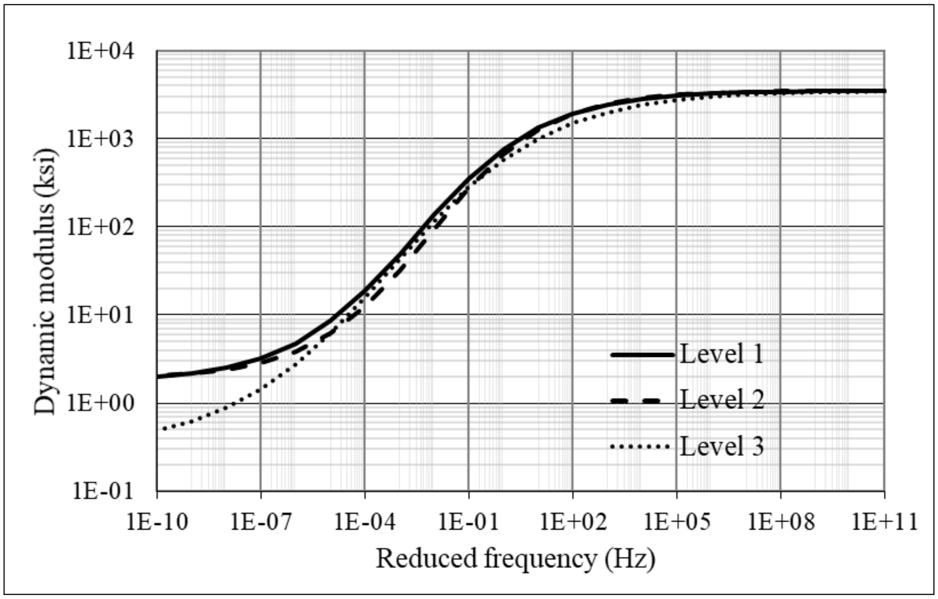

Figure 3-1. Dynamic modulus for AC at 68 °F

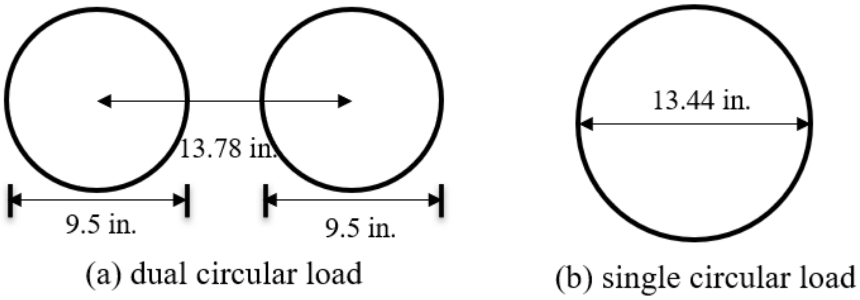

Figure 3-2. Equivalent uniform circular loads of TSD: (a) dual circular load; (b) single circular load

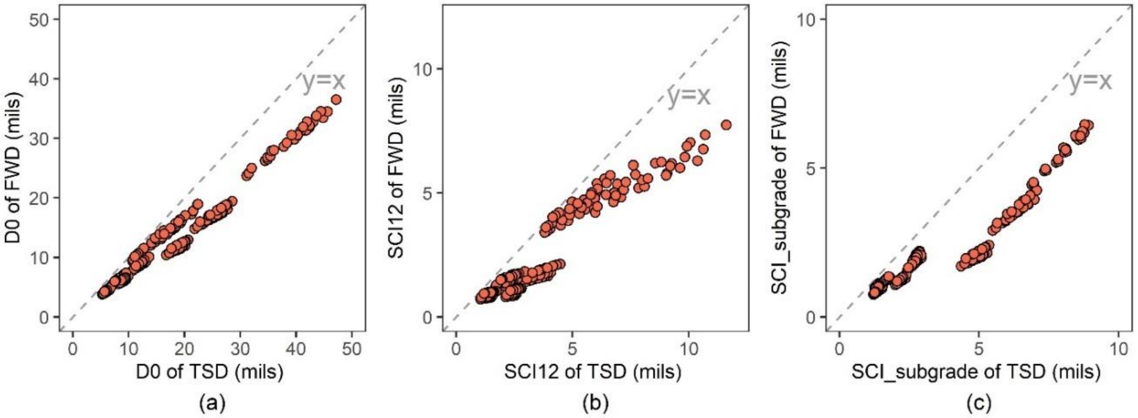

Figure 3-3. Deflection comparison between TSD and FWD: (a) D0; (b) SCI12; (c) SCI_subgrade

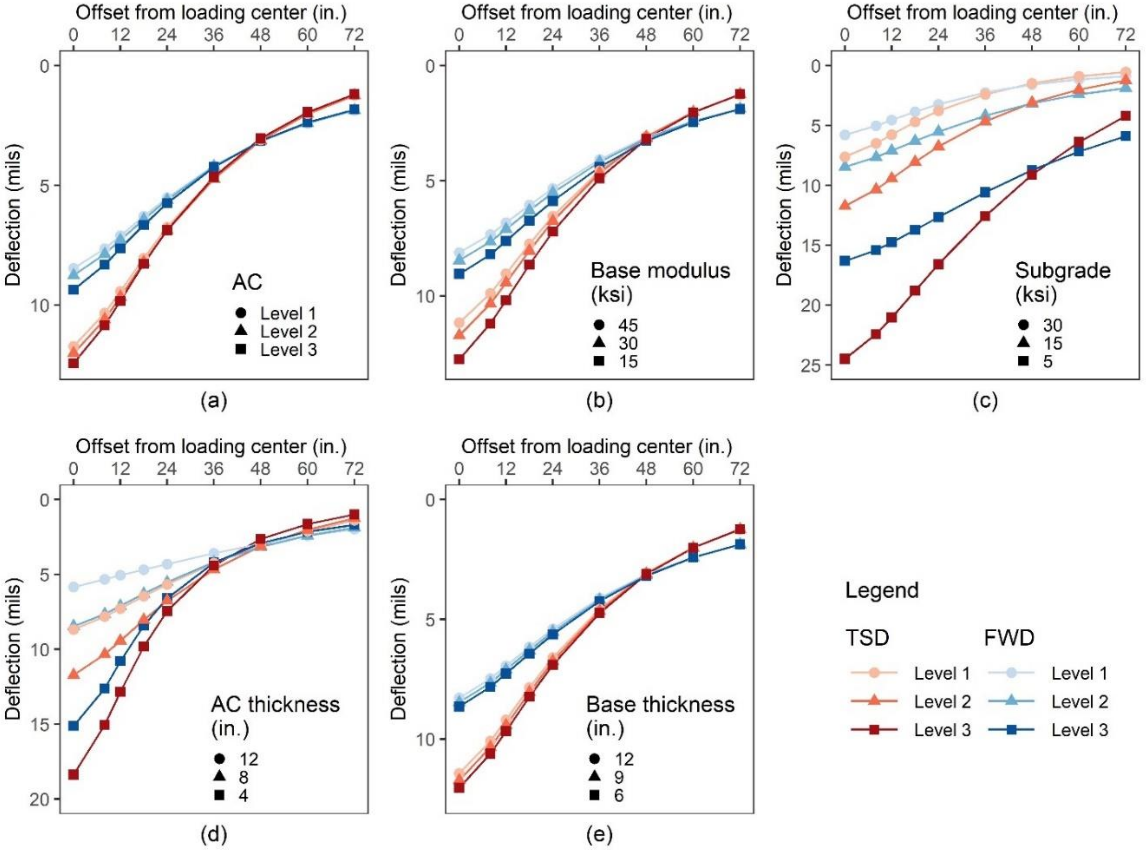

Figure 3-4. 3D-Move deflections for varying pavement conditions: (a) AC dynamic modulus; (b) base modulus; (c) subgrade modulus; (d) AC thickness; (e) base thickness

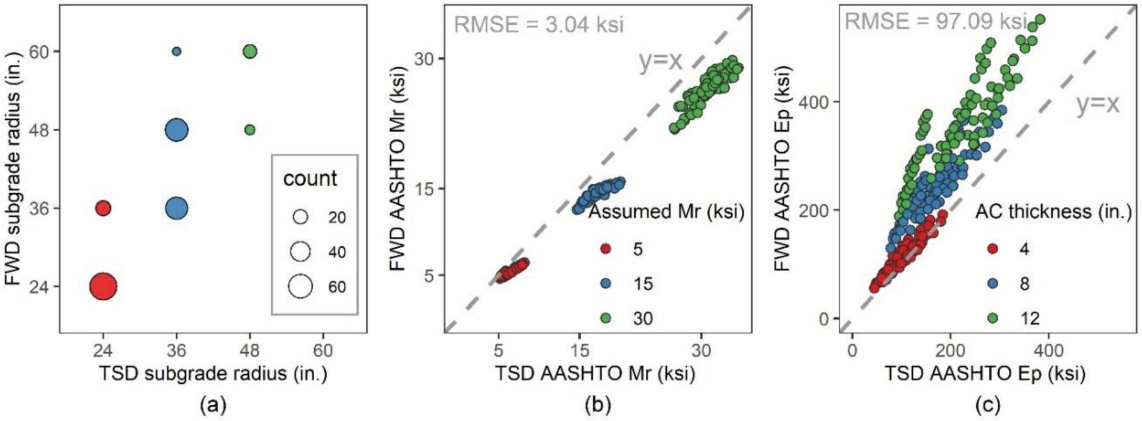

Figure 3-5. AASHTO SN calculation process: (a) AASHTO subgrade radius; (b) AASHTO subgrade resilient modulus; (c) AASHTO pavement effective modulus

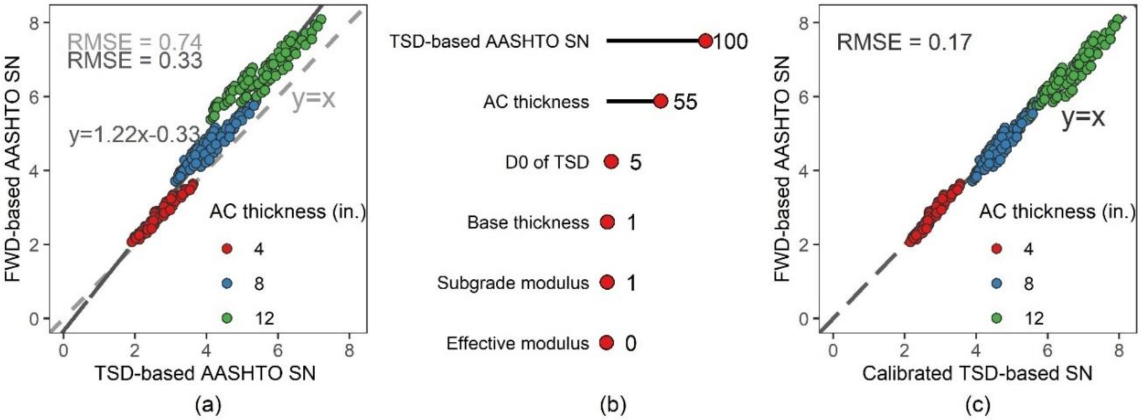

Figure 3-6. TSD-based SN: (a) Linear regression; (b) Variable importance of the random forest model; (c) Calibration by AC thickness

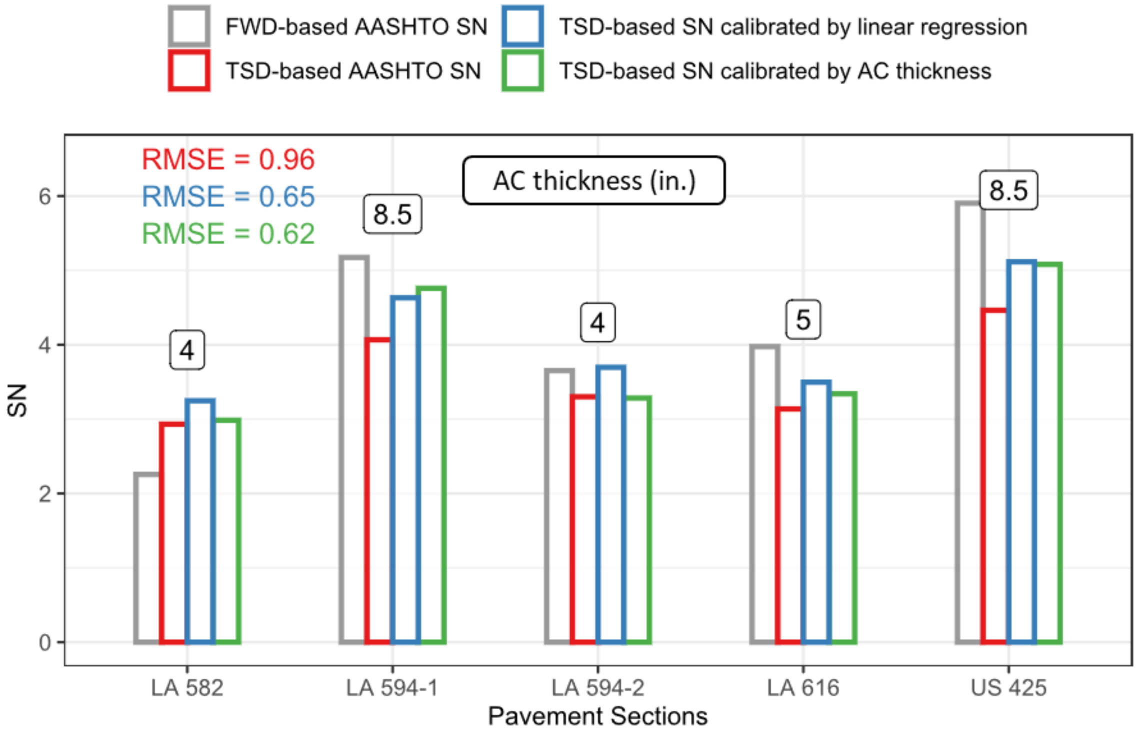

Figure 3-7. SN in pavement sections at Louisiana

Table 3-1. Design factors in the parametric study

Levels	Thickness (in.)		Modulus (ksi)		
	AC	Base	AC	Base	Subgrade
Level 1	12	12	1500*	45	30
Level 2	8	9	1350*	30	15
Level 3	4	6	1100*	15	5

* Equivalent AC modulus corresponding to the equivalent loading frequency of FWD.

Table 3-2. Simulation parameters of TSD and FWD

	FWD	TSD
Load type	Static	Moving (40mph)
Load shape	Single circular	Dual circular
Load magnitude	82.2 psi	82.2 psi
AC layer	Elastic	Linear viscoelastic
Other layers	Elastic	Elastic

CHAPTER 4

USE OF DEFLECTION SLOPES FROM TRAFFIC SPEED DEFLECTOMETER FOR EVALUATING STRUCTURAL CHARACTERISTICS OF ASPHALT PAVEMENTS

A version of this chapter was recently submitted for possible publication by Miaomiao Zhang, Rui Xiao, Yuetan Ma, Xi Jiang, Pawel Polazyk, and Baoshan Huang to Construction and Building Materials.

My contributions were conducting the literature review, developing numerical simulation models, performing the curve fitting and interpolation, and writing the text contained in the paper. Dr. Rui Xiao, Dr. Yuetan Ma, Dr. Xi Jiang, Dr. Pawel Polazyk, and Dr. Baoshan Huang provided ideas, guidance, and comments throughout the whole research and offered editorial assistance with the text.

Abstract

The Traffic Speed Deflectometer (TSD) overcomes the limitations of the Falling Weight Deflectometer (FWD) in terms of traffic interruption and testing inefficiency, making it an efficient tool for network-level pavement structural evaluation. The current research on TSD is inherited from FWD and mainly focuses on deflection. However, the raw measurement of TSD is the deflection slope, i.e., the first-order derivative of deflection. TSD deflection is calculated by curve fitting and integration, and the extensive use of deflection may accumulate the error caused by curve fitting. This study explores the potential use of TSD slope in assessing the strength of pavement structures, estimating the location of the inflection point, and calculating the lag distance. The results show that both the TSD deflection and slope are effective in detecting weak asphalt layers and subgrades, but they are not sensitive to damage to the base layer. It is recommended that TSD slopes at 5” and 60” (in front of the load center) be used to indicate the strength of the asphalt layer and subgrade, respectively. The location of the inflection point is related to the asphalt thickness and subgrade modulus, and it can be approximated by the location of the maximum slope measurement. In addition, the lag distance can be calculated by determining the maximum deflection point or by determining the zero-slope point. The zero-slope method is recommended over the maximum deflection method due to its accuracy and robustness.

Introduction

Structural assessment of existing pavements is important for maintenance and rehabilitation decisions. Estimating the structural strength of pavements through layer thickness and laboratory-determined material properties is destructive and costly. The only reliable non-destructive method currently available for determining the pavement structural capacity is the deflection measurement. The stationary falling weight deflectometer (FWD) is the most prevailing deflection measurement method, which is equipped with geophones at fixed radial distances from the loading center to measure the surface deflection of the pavement [1]. In the United States, more than 90% of states routinely conducted FWD testing as of 2008 [2].

FWD has a wide range of applications in pavement structural evaluation. The 1993 AASHTO design guide introduced a method to estimate the structural number (SN) of existing pavement through FWD deflections [3]. Combined with layer thickness, deflection can also be used to back-calculate the layer modulus [4]. In addition, an FWD-based benchmark method, namely Deflection Bowl Parameters (DBPs), provides a simple and fast way to estimate pavement structural conditions by deflection slope parameters [5]. The best-known deflection slope parameter is the surface curvature index SCI_12, which is the difference between the deflection at the loading point and the deflection at a radial distance of 12 inches and is commonly used to represent the strength of the asphalt layer [6,7]. However, FWD is a stationary device that must remain stationary at each test point. Traffic control and limited productivity hinder the FWD testing for network-level pavement structural evaluation.

Recent technological advancements have led to the development of continuous deflection measurement devices, including the traffic speed deflectometer (TSD), which is capable of performing deflection measurements at traffic speeds [8,9]. TSD uses Doppler lasers mounted on the centerline of rear dual tires to measure the deflection velocity (horizontal and vertical) of the pavement surface at traffic speeds [8]. The horizontal proportion of the deflection velocity is related to the moving speed of TSD. To eliminate the dependence on the moving speed, the measured deflection velocity is divided by the instantaneous moving speed to obtain the deflection slope [10]. The deflection slope is the first-order derivative of the deflection, which is converted to actual pavement deflection by curve fitting and numerical integration [11].

Many studies have been conducted to improve and expand the application of TSD. These studies were mainly inherited from FWD, such as using TSD deflections to back-calculate layer modulus or to calibrate the FWD-based equations [12–14]. FWD measures pavement deflection, so the TSD study also focuses on the deflection itself, ignoring potentially useful information in the TSD deflection slope. Since the TSD slope is the raw measurement, the intensive use of deflection may accumulate errors caused by curve fitting. In addition, the most commonly used deflection index, the surface curvature index, such as SCI_12 (as shown in Figure 4-1, all tables and figures are located in the Appendix), is essentially the tangent of the deflection, which is an approximation of the deflection slope. The use of the TSD slope may avoid the introduction of additional deflection indices.

The deflection basin has long been described as three distinct zones: positive curvature, curvature inflection, and reverse curvature, as shown in Figure 4-2. Many studies have linked the structural integrity of different layers to the different zones [5,7]. The inflection point is where the deflection basin switches from a positive curvature to a reverse curvature. It has been shown that the drift of the inflection point is often observed in the presence of a weak subgrade [15]. However, the exact location of the inflection point is difficult to determine from the deflection, especially since the field deflection measurements are limited to pre-set distances (geophones), which makes it even more difficult to locate the inflection point. For the FWD deflection basin, a plot of the deflection tangents versus horizontal distance is often used to estimate the location of the inflection point [5]. Since the TSD slope is the first-order derivative of the deflection, the inflection point should be exactly where the maximum slope occurs. Therefore, it may be easier to use the TSD slope to determine the location of the inflection point.

In addition, the viscoelasticity of the asphalt concrete (AC) and the inertia and damping of the pavement structure could result in a lag between the time when the TSD crosses over the point and the time when the maximum response occurs [16]. Therefore, there is a lag between the load center and the maximum deflection point in the TSD deflection basin, as shown in Figure 4-2. Several studies have suggested the possibility of using deflection lags to predict the fatigue condition of the AC layer [17,18]. It is also a new challenge to accurately estimate the deflection lag based on field TSD data. The maximum deflection point is exactly the zero-slope point, and it may be more accurate to calculate the deflection lag from the TSD slope.

The objective of this study was to explore the potential use of TSD slope in pavement structural evaluation. The substitutability of TSD slope for deflection in assessing the strength of pavement structures was investigated. The feasibility of estimating the inflection point by TSD slopes was evaluated. In addition, the advantages of using TSD slopes to calculate deflection lags were discussed. Numerical simulations based on the 3D-Move program were used to obtain TSD deflections/slopes of various pavement structures.

Pavement Structural Strength

In field TSD data collection, TSD uses several Doppler sensors to acquire slope measurements at discrete points. Typically, the Doppler sensors are installed in front of the load center and measure only half of the deflection basin before the load center [11]. However, since the maximum deflection point occurs behind the load center, only TSD devices that cover the deflection basin behind the load center can be used to investigate deflection lag. In this study, the TSD loading configuration and Doppler sensors arrangement were based on the upgraded version of the TSD device operated by the Australian Road Research Council (ARRB) Group Inc. As shown in Figure 4-3, ten Doppler sensors are mounted at -18, -12, -8, 5, 8, 12, 18, 24, 36, and 60 inches in front of the load center. The slope at location *r* inches in front of the load center is defined as S*r*, and the slope at location *r* inches behind the load center is defined as S.*r*. The TSD slope is converted to actual pavement deflection by curve fitting and numerical integration. The pavement surface deflection at any given location is the area under the fitted slope curve from the tail to that particular location. The deflection at location *r* inches in front of the load center is defined as D*r*, and the deflection at location *r* inches behind the load center is defined as D.*r*. Notable TSD deflections are at 0, 8, 12, 18, 24, 36, 48, 60, and 72 inches in front of the load center. In the subsequent analysis, if not otherwise specified, the deflections and slopes at the discrete points are:

- Deflection: (D.18, D.12, D.8), D0, D8, D12, D18, D24, D36, D48, D60, and D72.
- Slope: (S.18, S.12, S.8), S5, S8, S12, S18, S24, S36, and S60.

For generality, the deflections and slopes at locations behind the load center were only used for the analysis of the deflection lag.

In this study, numerical simulations were used to obtain the TSD deflection and slope of different pavement structures. The numerical model was developed based on the 3D-Move program, which has been validated with field data in many studies [10,19]. In order to include as many pavement structures as possible, a database of 243 different three-layer pavement structures was considered. As shown in Table 4-1, three levels of plant-produced AC materials, base modulus, subgrade modulus, AC thickness, and base thickness were considered. The AC viscoelasticity was characterized by its dynamic modulus curve because the Fourier transform technique used in the 3D-Move allows the direct use of the frequency swept dynamic modulus. The details of the TSD simulation can be found in the previous study [12]. The moving speed was set to 40 mph and the test temperature was 20 °C.

Sensitivity analysis

To evaluate the substitutability of the TSD slope for deflection, it is important to ensure that the slope contains at least as much information as the deflection. The use of TSD slope instead of deflection does not result in a loss of useful information for pavement structural evaluation. Therefore, the effect of pavement structure variations on TSD deflection and slope was investigated. Figure 4-4 shows the TSD deflection (red, left axis) and slope (blue, right axis) for varying pavement structures. The default AC material, AC thickness, base modulus, base thickness, and subgrade modulus were level 1, 8 inches, 30 ksi, 9 inches, and 15 ksi, respectively.

For the half TSD basin in front of the load center, the TSD deflection decreases monotonically as the horizontal distance increases. However, the TSD slope curve is not monotonic; it increases and then decreases with increasing horizontal distance. The slope curve is more complex and variable than the deflection curve, and it may include more useful information. In addition, it can be found that as the modulus or thickness increases, the TSD deflection and slope decrease. Weaker pavement structures can lead to greater deflections and slopes. There are significant differences in TSD deflections and slopes for different AC thickness and subgrade modulus. However, for other pavement structure parameters, the differences in TSD deflections and slopes are not significant. Therefore, the TSD deflection and slope are sensitive to AC thickness and subgrade modulus, but not to the base layer. The sensitivity of TSD slope to different pavement structures is similar to that of TSD deflection, so the substitutability between slope and deflection is satisfactory. Both deflection and slope are effective in detecting weak asphalt layers and subgrades, but they are not sensitive to the damage to the base layer.

Among the TSD deflections at different locations, the TSD deflection at the loading point (D0) is the most sensitive to almost all pavement structure parameters. This is because D0 is the accumulation of deformations of all layers and is therefore related to the parameters of all layers. The deflection at the far end is almost entirely due to the deformation in the subgrade and is therefore exclusively related to the subgrade modulus. Similarly, the TSD slope at locations far from the loading point depends only on the subgrade modulus. However, compared to the slope at the loading point (S0), the maximum TSD slope is more sensitive to different pavement structure parameters. The maximum TSD slope usually occurs about 12 inches in front of the loading point.

Visual inspection of the TSD measurements (Figure 4-4) shows that deflection and slope are correlated with related to AC thickness and subgrade modulus, while there appears to be little relationship with pavement structure parameters. However, there may be some patterns in deflection (or slope) that cannot be fully captured by visual inspection, such as interactions between deflections. More sophisticated methods are needed to fully and exhaustively investigate the pavement structure information contained in the deflection (slope). A machine learning method, namely the random forests (RF) method, was employed to achieve such a purpose.

The RF model was developed to predict pavement structure parameters by using the theoretical deflections (or slopes) at discrete locations as predictors. Five RF models were developed using theoretical deflections to predict the AC type, AC thickness, base modulus, base thickness, and subgrade modulus with testing R^2 of 53.1%, 99.3%, 72.4%, 21.6%, and 99.9%, respectively. Another five RF models were developed using theoretical slopes as predictors, and R^2 of 75.9%, 99.8%, 66.4%, 11.2%, and 99.7% correspond to the AC type, AC thickness, base modulus, base thickness, and subgrade modulus, respectively. A large R^2 implies a better predictive performance, i.e., the deflection (or slope) contains enough information to predict the structure parameters. It can be found that the AC thickness and subgrade modulus can be well predicted by TSD deflections (slopes). The base thickness is the least predictable parameter because it has little effect on TSD deflections (slopes). Therefore, TSD deflections and slopes can only be used to detect weak asphalt layers and subgrades, either by visual inspection or by more sophisticated machine learning methods.

Correlation with pavement structures

TSD deflections (slopes) effectively indicate the AC thickness and subgrade modulus. The correlation analyses for deflections (slopes) at different locations were performed to find the deflection (slope) that is most relevant to the AC thickness (or subgrade modulus). Several FWD-based studies have shown that deflection by itself does not directly indicate pavement structure information and some additional deflection indices have been introduced as a supplement [20]. The most used deflection indices are:

$$SCI\_12 = D0 - D12 \tag{1}$$

$$SCI\_sub = D36 - D60 \tag{2}$$

The surface curvature index (SCI) is the difference in deflection between two points. SCI_12 is an important indicator of the strength of the AC layer, while SCI_sub reflects the subgrade strength [21].

Figure 4-5 shows the Pearson correlation between TSD indices and AC thickness (or subgrade modulus). Pearson correlation coefficient (the absolute value) is a measure of the linear correlation between two variables [22]. In Figure 4-5(a), the TSD deflection itself is shaded in red, while the introduced deflection index is shaded in blue. It can be found that the TSD deflection itself is not highly correlated with the AC thickness. Among all TSD deflections, D0 shows the highest correlation with the AC thickness, while the Pearson correlation coefficient is only 0.51. As the horizontal distance increases, the correlation between the deflection and AC thickness decreases. SCI_12 helps to correlate TSD deflections to the AC thickness with a correlation coefficient of 0.81. Therefore, SCI_12 is a good complement to the TSD deflection. In TSD deflection applications, it is necessary to identify the weak AC layer with the help of SCI_12.

In contrast, almost all TSD deflections are closely related to the subgrade modulus. The correlation between the deflection and subgrade modulus increases slightly with increasing horizontal distance (coefficients of 0.73-0.89). This is because the pavement surface deflection is an accumulation of deformation in each layer, of which the deformation in subgrade is the most important component, even if it is D0. Studies have shown that more than 70% of D0 comes from the deformation of the subgrade [9,23]. For the SCI_sub, the correlation coefficient is about 0.85, which does not improve the correlation between TSD deflections and the subgrade modulus. Therefore, there is no need to introduce SCI_sub, and TSD deflections at far ends are better indicators of subgrade modulus.

For TSD slopes (Figure 4-5(b)), some TSD devices do not measure the TSD slope behind the load center, and these slopes are shaded in blue. S0 may be disturbed by the dynamic loading of the TSD and thus exhibits unexplained behavior, so the TSD device hardly measures S0. As the horizontal distance increases, the correlation between the TSD slope and AC thickness gradually decreases, while the correlation with subgrade modulus gradually increases. Slopes near the load center are almost entirely related to the AC thickness, while slopes at far ends depend almost exclusively on the subgrade modulus. The TSD slope itself can be well correlated with the AC layer thickness and subgrade modulus, so it can be used to identify weak AC layers and subgrades without introducing additional slope indices.

The deflection of the pavement surface accumulates the deformation of all layers, while the deflection slope better distinguishes the deformation of the different layers. SCI originally came from the study of FWD, which measures deflection rather than slope. SCI is used to approximate the slope (see Figure 4-1). However, TSD measures slope and calculates deflection by curve fitting and numerical integration. Therefore, using TSD slope to identify weak AC layers and subgrades is more accurate and less labor-intensive than using TSD deflection. TSD slopes near the load center are good indicators of the AC thickness. S.8 shows the highest correlation with AC thickness (correlation coefficient of 0.90), but the availability is poor because it is located after the load center. Therefore, S5 (with a correlation coefficient of 0.86) is recommended to indicate the AC layer. S60 is the most correlated with subgrade modulus (with a correlation coefficient of 0.86) and is recommended to represent the strength of the subgrade.

It is worth noting that the deflection slope is the first-order derivative of the deflection in the horizontal direction, while the vertical strain is the first-order derivative of the vertical deformation of the pavement (deflection). Under TSD vertical loading, the horizontal extension of the stress distribution in the different layers is different and increases with the depth of the pavement structure. Therefore, the deflection slope is more effective in distinguishing the different layers than the deflection itself (vertical deformation). However, the stress-strain relationship in the vertical direction can be used to back-calculate the layer modulus. In this respect, the deflection is certainly more valuable than the slope.

Inflection Point

As shown in Figure 4-1, the deflection basin can be described as three distinct zones. In Zone 1, closest to the load center, the deflection basin has a positive curvature. This zone is usually within a radius of no more than 12 inches from the load center [7]. Zone 2, the inflection zone, is the area where the curvature of the deflection basin switches from positive to negative. Zone 2 is usually located within a range of about 12 inches to 24 inches from the load center, and the inflection point is located within this zone. Zone 3 is the farthest from the load center. In this zone, the deflection basin is switched to reverse curvature and extends to the normal pavement surface (zero deflection). Zone 3 usually starts at about 24 inches [7].

The concept of the three distinct zones has been proposed for many years; however, the exact locations of the three zones have yet to be determined. The location of the inflection point depends on the pavement structures and is almost impossible to obtain from the deflections at several discrete locations. The deflection acceleration is the first-order derivative of the TSD slope, while the TSD slope is the first-order derivative of the deflection. The dividing point between Zone 2 and Zone 3 should be Point A, where the minimum acceleration occurs. The dividing point between Zone 1 and Zone 2 should be Point A', where the slope is equal to the slope at Point A. The inflection point of the TSD deflection is exactly where the maximum slope occurs. Therefore, the inflection point can be located simply by identifying the maximum slope point. The inflection point location is defined as the horizontal distance between the inflection point and the load center.

Influencing factors

To investigate the factors affecting the inflection point locations, the inflection point locations were calculated for different pavement structures (as listed in Table 4-1) based on the 3D-Move simulation results. For each TSD model (pavement structure), the 3D-Move program outputs 1024 points of slope with an output interval of approximately 0.26 inches. The Modified Akima piecewise cubic Hermite interpolation method was employed to fit the 1024 slope points with an interpolation accuracy of 0.001 inches. Based on the fitted slope curve, the location of the maximum slope point can be determined, which is the inflection point location. 3D-Move simulation results show that the inflection point location is different for different pavement structures. The RF method was employed to rank the importance of different pavement parameters on the inflection point location, as shown in Figure 4-6(a). Subgrade modulus and AC thickness are tied as the most important factors. The AC type, modulus and thickness of the base layer have little effect on the inflection point location.

Figure 4-6(b) shows the influence of AC thickness and subgrade modulus on the inflection point location. As the AC thickness increases, the horizontal distance between the inflection point and the load center also increases. This can be explained by the fact that the extent of Zone 1 increases with the increase of the AC thickness. Zone 3 is more related to the subgrade, and a stiffer subgrade means a larger extent of Zone 3. Therefore, the horizontal distance between the inflection point and the load center decreases with the increase of the subgrade modulus. In the presence of very soft subgrades, a significant drift of the inflection point can be observed.

Approximation of inflection point location

In practical applications of TSD, it is laborious to estimate the location of the inflection point from TSD slope measurements at discrete locations using curve fitting and interpolation methods. The location of the inflection point can be approximated by the maximum TSD slope measurement (among S5, S8, S12, S18, S24, S36, and S60). The detailed procedure for identifying the approximate inflection point location is:

Step 1: Compare S5, S8, S12, S18, S24, S36, and S60 to obtain the maximum TSD slope measurement S*x*.

Step 2: Obtain the approximate inflection point location *x*.

The approximate inflection point location for different pavement structures was calculated based on the 3D-Move simulation results. The theoretical and approximate inflection point locations were compared to assess the reliability of the proposed inflection point approximation method, as shown in Figure 4-7. The theoretical inflection point occurs within a range of about 8 inches to 24 inches from the load center, while the approximate inflection point location is between 8, 12, 18, and 24 inches. The scatter plot of the theoretical and approximate inflection point locations is also shown in Figure 4-7.

It can be found that the approximate inflection point location is close to the theoretical inflection point location with an R^2 of 87.8%. The Root Mean Square Error (RMSE) of the proposed approximation method is 1.48 inches, which means that the approximate inflection point location is expected to deviate from the theoretical inflection point location by 1.48 inches. The approximate inflection point location is considered sufficiently accurate in terms of its simplicity. It is recommended to estimate the inflection point location based on the TSD slope, i.e., the location of the maximum TSD slope measurement.

Lag Distance Calculation

Lag distance calculation methods

The lag distance is defined as the horizontal distance between the load center and the location where the maximum deflection occurs. The location of the maximum deflection point is exactly where the TSD slope is zero (Figure 4-2). Therefore, the lag distance can be calculated by identifying the maximum deflection point or by identifying the zero-slope point.

- Maximum deflection method:
  Step 1: Fit the TSD slope curve.
  Step 2: Integrate the TSD slope curve to obtain TSD deflection in discrete points.
  Step 3: Fit the TSD deflection curve.
  Step 4: Determine the location of the maximum deflection point.
- Zero-slope method:
  Step 1: Fit the TSD slope curve.
  Step 2: Determine the location of the zero-slope point.

The maximum deflection method has more steps since the TSD slope is the raw measurement and the TSD deflection is calculated by curve fitting and numerical integration. In contrast, the fitting of the TSD slope curve is included in the deflection calculation and does not require additional work.

The most important step to accurately calculate the lag distance is curve fitting. Typically, curve fitting is a process of constructing a predefined mathematical function and selecting the parameters by fitting that function to the data points. However, the shape of the TSD deflection (slope) curve is complex, and it is not symmetric about the load center due to the presence of deflection lag. It is also not symmetric about the maximum deflection (zero-slope) point, as the TSD deflection basin itself is asymmetric (steep at the leading edge and shallow at the trailing edge) [17]. It is difficult to construct a mathematical function that fits the TSD deflection (slope) well. Even if successful, this mathematical function must include many unknown parameters. Given the limited number of TSD Doppler sensors (slope measurements), fitting so many unknown parameters is unrealistic. Most curve fitting methods either ignore the deflection lag or assume that the deflection curve is symmetric [24]. The Greenwood method models the slope curve as a sum of symmetric (Gaussian) and asymmetric (stable distribution) functions, but is proprietary in its details [11].

Interpolation is commonly used to fit complex curves by applying different polynomial functions between consecutive measurement locations, which is suitable for fitting deflection (slope) curves. In this study, four interpolation methods with different levels of complexity were applied, including:

- Linear: Linear spline interpolation
- Cubic: Cubic spline interpolation
- Pchip: Piecewise cubic Hermite interpolation polynomial
- Makima: Modified Akima piecewise cubic Hermite interpolation

The linear spline interpolation is the simplest interpolation method, which connects adjacent data points by straight lines. The Cubic, Pchip, and Makima methods all perform different forms of piecewise cubic interpolation. Each method differs in the way it calculates the interpolant slope, leading to different behavior when the underlying data has flat areas or undulations [25].

In field TSD data collection, the TSD deflection of discrete points is always given by the TSD device operator, so Steps 1-2 in the maximum deflection method were skipped in this study. The fitted lag distances were calculated from the deflection curves fitted by the 12 TSD deflection points, namely D.18, D.12, D.8, D0, D8, D12, D18, D24, D36, D48, D60, and D72. For the zero-slope method, the fitted lag distances were calculated by fitting ten TSD slopes located at -18, -12, -8, 5, 8, 12, 18, 24, 36, and 60 inches from the load center.

Evaluation of lag distance calculation methods

Based on the 3D-Move simulation results of different pavement structures (Table 4-1), the fitted lag distances for the maximum deflection method and the zero-slope method were calculated. To evaluate the accuracy and feasibility of the four interpolation methods, the fitted lag distances of different interpolation methods were calculated separately. The theoretical lag distance was also calculated from the 3D-Move simulation results, but with a finer interpolation interval. The theoretical lag distance was calculated by the zero-slope method using the point spacing of 0.26 inches (1024 TSD points in total), which is the output spacing of the 3D-Move program. The Makima interpolation method was employed to fit the slope curve of 1024 data points with an interpolation accuracy of 0.001 inches.

Figure 4-8(a) shows the fitted lag distance for the different interpolations calculated with the maximum deflection method. The maximum deflection point occurs behind the load center, and the lag distance is generally less than 8 inches. The calculation of the lag distance depends mainly on the interpolation between D.8 and D0. For the maximum deflection method, the essence of linear interpolation is to compare D.8 and D0, with a lag distance of only 0 (D0>D.8) or 8 (D0<D.8) inches. The same lag distance was obtained by the Pchip interpolation because the fitted deflection curve was locally over-flattened to avoid the overshoot problem. The fitted lag distances calculated by the Cubic and Makima interpolation are usually smaller than the theoretical lag distances. As the theoretical lag distance increases, the difference between the fitted and theoretical values increases. Overall, the fitted lag distances calculated by different interpolations vary considerably. The Makima method performs the best with the largest R^2 (99.1%) and the smallest RMSE (0.35 inches). The accuracy of the maximum deflection method is greatly influenced by the selection of interpolation methods.

Figure 4-8(b) shows the fitted lag distances calculated with the zero-slope method. The calculation of the lag distance depends mainly on the interpolation between S.8 and S5. For the linear interpolation, the lag distance Δl can be calculated as:

$$\frac{|5|+\Delta l}{|-8|-\Delta l} = \frac{|S5|}{|S.8|} \tag{3}$$

The Pchip and Makima interpolation tie for the best with the smallest RMSE (0.38 inches). The linear interpolation shows the largest error (RMSE) while the highest R^2. Compared with other interpolations, linear interpolation tends to obtain larger fitted lag distances, especially when the theoretical value is greater than 5 inches. Overall, the fitted lag distances for different interpolations are similar, so the zero-slope method is not sensitive to interpolation methods.

Due to the different spacing of the fitted data points, the Makima interpolation of the maximum deflection method (D.8 and D0) shows smaller RMSE and greater R^2 than that of the zero-slope method (S.8 and S5). However, in field TSD applications where the TSD slope is the raw measurement and the deflection is integrated from TSD slopes, calculating the lag distance using the maximum deflection method will accumulate the error caused by curve fitting and integration. In addition, the maximum deflection method is more sensitive to the interpolation method than the zero-slope method. This is because the TSD deflection curve is not monotonic near the maximum deflection point, which increases the difficulty of curve fitting and limits the choice of interpolation methods. In contrast, the TSD slope curve is monotonic around the zero-slope point and is therefore more robust to different interpolation methods. Therefore, the zero-slope method is recommended over the maximum deflection method due to its accuracy and robustness. Considering the simplicity of linear interpolation of the zero-slope method (Equation (3)), it is considered sufficiently accurate and practical to provide at least an initial guess about the lag distance at the network-level.

Conclusion

TSD is capable of performing deflection measurements at traffic speeds and is therefore an efficient tool for network-level pavement structural evaluation. The current research on

TSD is inherited from FWD, so it mainly focuses on deflection. However, TSD measures the deflection slope, and the extensive use of deflection may ignore the potentially useful information in the deflection slope and accumulate errors caused by curve fitting. This study explored the potential uses of TSD slopes, including using TSD slopes to assess the strength of pavement structures, estimate the location of the inflection point, and calculate the lag distance. In addition, the advantages of using slope rather than deflection were discussed. All analyses were based on the simulation results of the 3D-Move program. Based on the analyses presented, the following conclusions are drawn:

- The sensitivity of TSD slope to different pavement structure parameters is similar to that of TSD deflection. Both deflection and slope are effective in detecting weak asphalt layers and subgrades, but they are not sensitive to the damage to the base layer.
- Deflection is not directly related to the AC thickness. The introduction of SCI_12 is a good complement to the deflection and can help to identify weak AC layers. In contrast, TSD deflections at far ends are directly related to subgrade modulus, so there is no need to introduce additional indices, such as SCI_sub.
- Deflection slope correlates well with the AC thickness and the subgrade modulus. The TSD slope itself can be used to identify weak asphalt layers and subgrades without introducing additional indices. S5 and S60 (slopes at 5 inches and 60 inches in front of the load center) are recommended to indicate the strength of the asphalt layer and subgrade, respectively.
- The location of the inflection point depends on the AC thickness and subgrade modulus. The horizontal distance between the inflection point and the load center increases as the AC thickness increases or as the subgrade modulus decreases. The location of the inflection point can be estimated from the location of the maximum TSD slope measurement.
- The lag distance can be calculated by identifying the maximum deflection point or by identifying the zero-slope point. The zero-slope method is recommended over the maximum deflection method due to its accuracy and robustness. The linear

interpolation between S.8 and S5 (slopes at -8 inches and 5 inches in front of the load center) is considered sufficiently accurate and practical to provide an initial guess about the lag distance at the network-level.

References

[1] Katicha, S. W., Flintsch, G. W., Ferne, B., & Bryce, J. (2014). Limits of agreement method for comparing TSD and FWD measurements. International Journal of Pavement Engineering, 15(6), 532-541.

[2] Alavi, S., LeCates, J. F., & Tavares, M. P. (2008). Falling weight deflectometer usage (No. Project 20-5 (Topic 38-15)).

[3] Transportation Officials. (1993). AASHTO Guide for Design of Pavement Structures, 1993 (Vol. 1). Aashto.

[4] Mehta, Y., & Roque, R. (2003). Evaluation of FWD data for determination of layer moduli of pavements. Journal of Materials in Civil Engineering, 15(1), 25-31.

[5] Horak, E., Emery, S., & Maina, J. (2015, August). Review of falling weight deflectometer deflection benchmark analysis on roads and airfields. In 11th conference on asphalt pavements for Southern Africa: CAPSA15 (pp. 16-19).

[6] Jiang, X., Gabrielson, J., Huang, B., Bai, Y., Polaczyk, P., Zhang, M., ... & Xiao, R. (2022). Evaluation of inverted pavement by structural condition indicators from falling weight deflectometer. Construction and Building Materials, 319, 125991.

[7] Horak, E. (2008). Benchmarking the structural condition of flexible pavements with deflection bowl parameters. Journal of the South African Institution of Civil Engineering, 50(2), 2-9.

[8] Flintsch, G. W., Ferne, B., Diefenderfer, B., Katicha, S., Bryce, J., & Nell, S. (2012). Evaluation of traffic-speed deflectometers. Transportation research record, 2304(1), 37-46.

[9] Zhang, M., Zhang, J., Gong, H., Jia, X., Xiao, R., Huang, H., & Huang, B. (2022). Numerical investigation of pavement responses under TSD and FWD loading. Construction and Building Materials, 318, 126014.

[10] Elseifi, M. A., Zihan, Z. U., & Icenogle, P. (2019). A Mechanistic Approach to Utilize Traffic Speed Deflectometer (TSD) Measurements into Backcalculation Analysis (No. FHWA/LA. 17/612). Louisiana State University. Department of Civil and Environmental Engieering.

[11] Nasimifar, M., Thyagarajan, S., & Sivaneswaran, N. (2018). Computation of pavement vertical surface deflections from traffic speed deflectometer data: evaluation of current methods. Journal of Transportation Engineering, Part B: Pavements, 144(1), 04018001.

[12] Zhang, M., Gong, H., Jia, X., Jiang, X., Feng, N., & Huang, B. (2022). Determining Pavement Structural Number with Traffic Speed Deflectometer Measurements. Transportation Geotechnics, 100774.

[13] Elbagalati, O., Mousa, M., Elseifi, M. A., Gaspard, K., & Zhang, Z. (2018). Development of a methodology to backcalculate pavement layer moduli using the traffic speed deflectometer. Canadian Journal of Civil Engineering, 45(5), 377-385.

[14] Flintsch, G., Katicha, S., Bryce, J., Ferne, B., Nell, S., & Diefenderfer, B. (2013). Assessment of continuous pavement deflection measuring technologies (No. SHRP 2 Report S2-R06F-RW-1).

[15] Dehlen, G. L. (1962). A simple instrument for measuring the curvature induced in a road surfacing by a wheel load. Civil Engineering= Siviele Ingenieurswese, 1962(9), 189-194.
[16] Rada, G. R., Nazarian, S., Visintine, B. A., Siddharthan, R. V., & Thyagarajan, S. (2016). Pavement structural evaluation at the network level (No. FHWA-HRT-15-074). United States. Federal Highway Administration. Office of Infrastructure Research and Development.
[17] Deng, Y., Luo, X., Gu, F., Zhang, Y., & Lytton, R. L. (2019). 3D simulation of deflection basin of pavements under high-speed moving loads. Construction and Building Materials, 226, 868-878.
[18] Carlson, P., Storey, B., Poorsartep, M., Stevens, C., Ettelman, B., Lindheimer, T. E., ... & Hurlebaus, S. (2017). Advancing innovative high-speed remote-sensing highway infrastructure assessment using emerging technologies: technical report (No. FHWA/TX-16/0-6869-1). Texas A&M Transportation Institute.
[19] Nasimifar, M., Siddharthan, R. V., Rada, G. R., & Nazarian, S. (2017). Dynamic analyses of traffic speed deflection devices. International Journal of Pavement Engineering, 18(5), 381-390.
[20] Chang, C., Saenz, D., Nazarian, S., Abdallah, I. N., Wimsatt, A., Freeman, T., & Fernando, E. G. (2014). TXDOT guidelines to assign PMIS treatment levels (No. 0-6673-P1). Texas. Dept. of Transportation. Research and Technology Implementation Office.
[21] Nasimifar, M., Thyagarajan, S., Siddharthan, R. V., & Sivaneswaran, N. (2016). Robust deflection indices from traffic-speed deflectometer measurements to predict critical pavement responses for network-level pavement management system application. Journal of Transportation Engineering, 142(3), 04016004.
[22] Benesty, J., Chen, J., Huang, Y., & Cohen, I. (2009). Pearson correlation coefficient. In Noise reduction in speech processing (pp. 1-4). Springer, Berlin, Heidelberg.
[23] Horak, E. (2010). Aspects of deflection basin parameters used in a mechanistic rehabilitation design procedure for flexible pavements in South Africa (Doctoral dissertation, University of Pretoria).
[24] Zofka, A., Sudyka, J., Maliszewski, M., Harasim, P., & Sybilski, D. (2014). Alternative approach for interpreting traffic speed deflectometer results. Transportation Research Record, 2457(1), 12-18.
[25] Akima, H. (1974). A method of bivariate interpolation and smooth surface fitting based on local procedures. Communications of the ACM, 17(1), 18-20.

Appendix

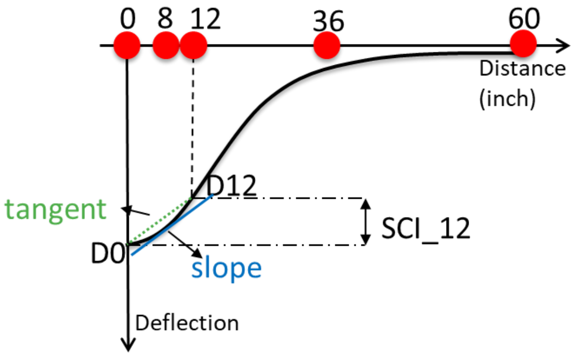

Figure 4-1. Surface curvature index (SCI)

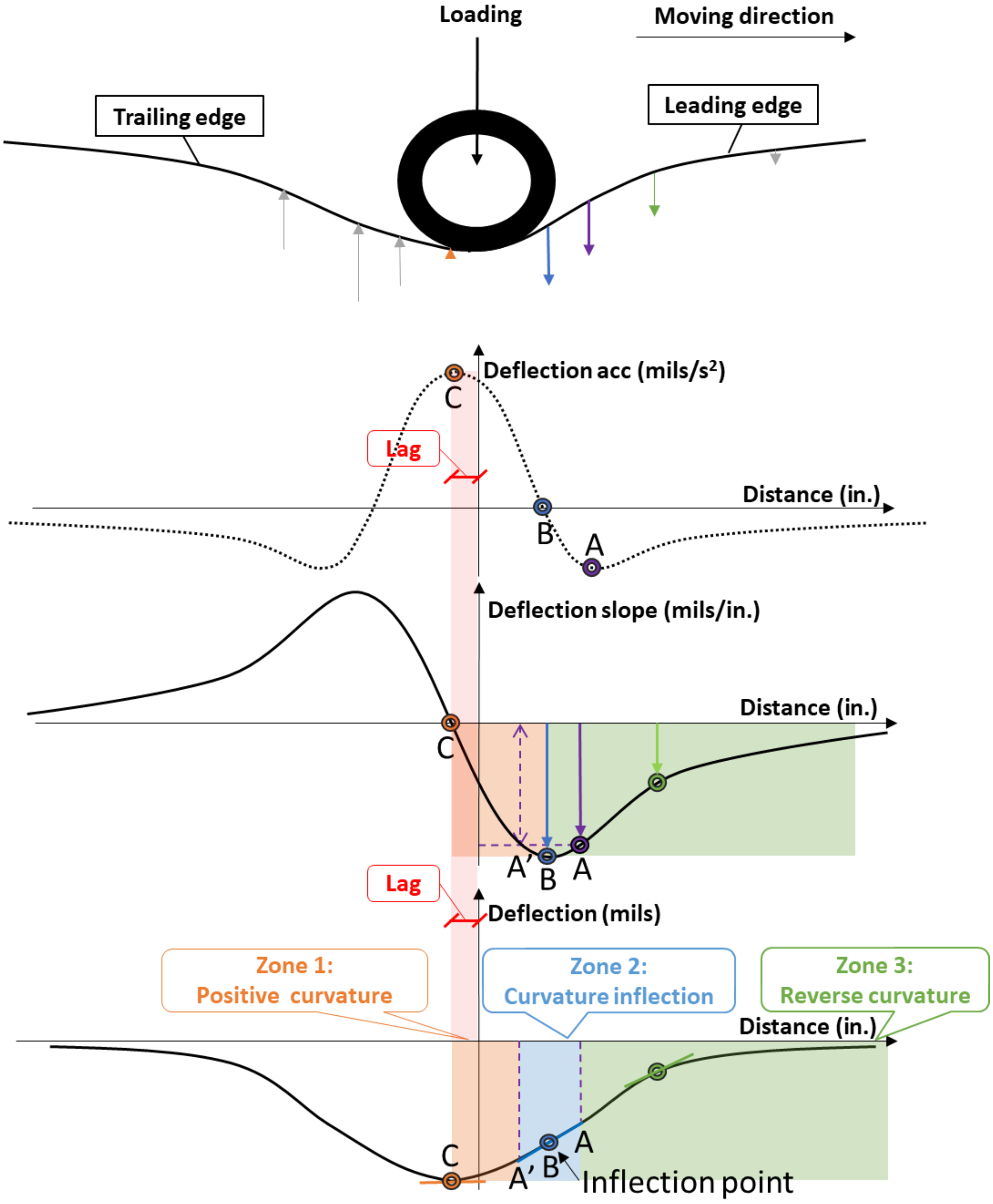

Figure 4-2. Schematic diagram of the TSD deflection, slope and acceleration curves

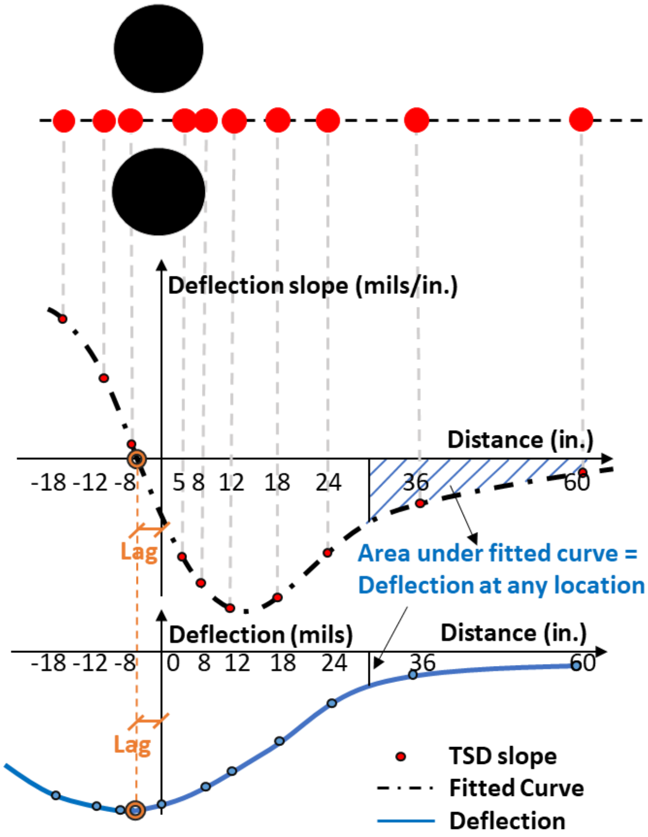

Figure 4-3. Schematic diagram of TSD slope collection

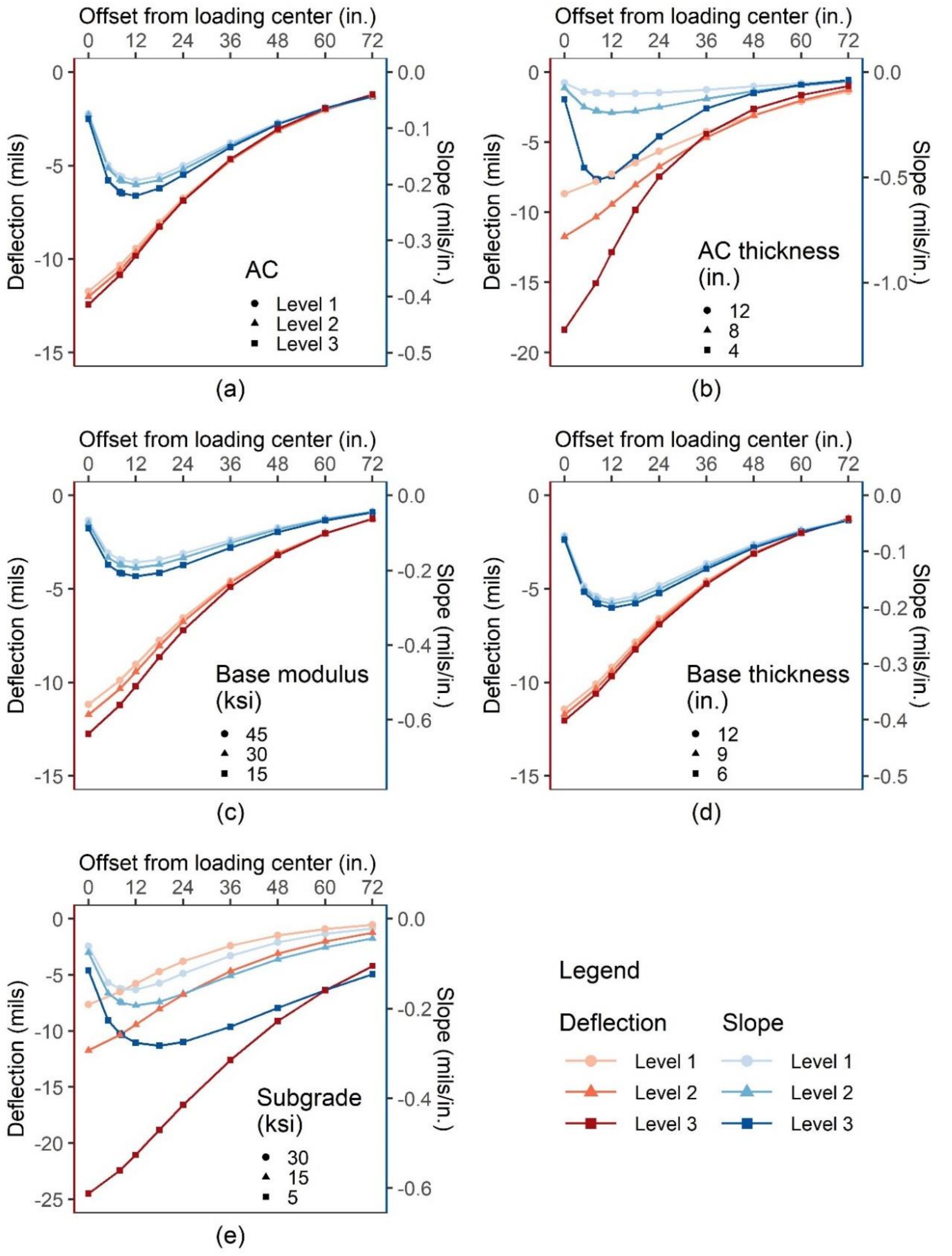

Figure 4-4. TSD deflections and slopes for varying pavement conditions: (a) AC dynamic modulus; (b) AC thickness; (c) base modulus; (d) base thickness; (e) subgrade modulus

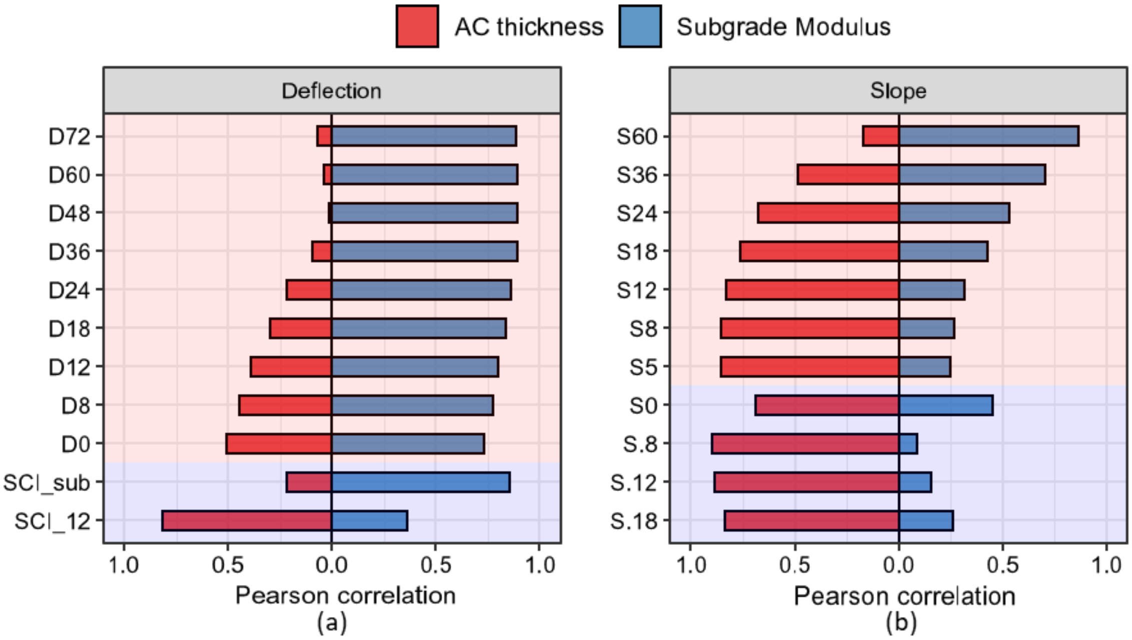

Figure 4-5. Correlation between TSD indices and pavement structures: (a) deflection itself; (b) deflection slope

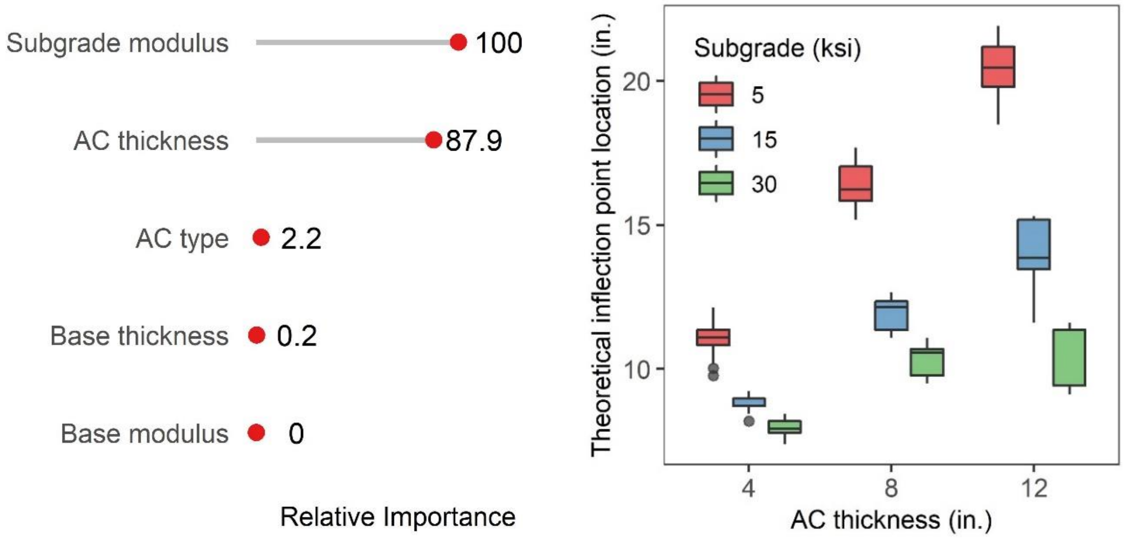

(a) (b)

Figure 4-6. Effect of pavement structures on the inflection point location: (a)importance ranking; (b) effect of AC thickness and subgrade modulus

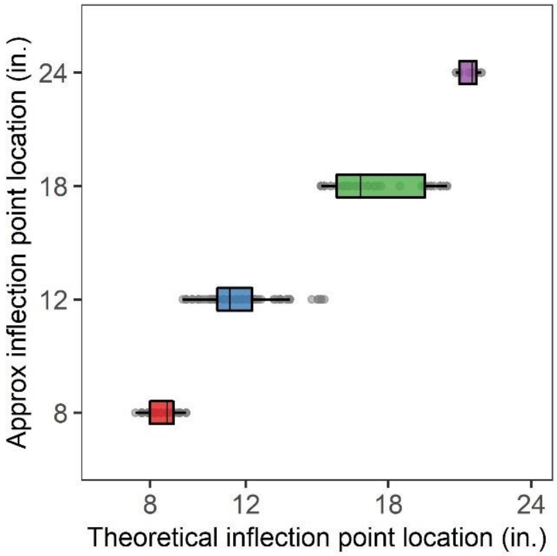

Figure 4-7. Approximate location of the inflection point

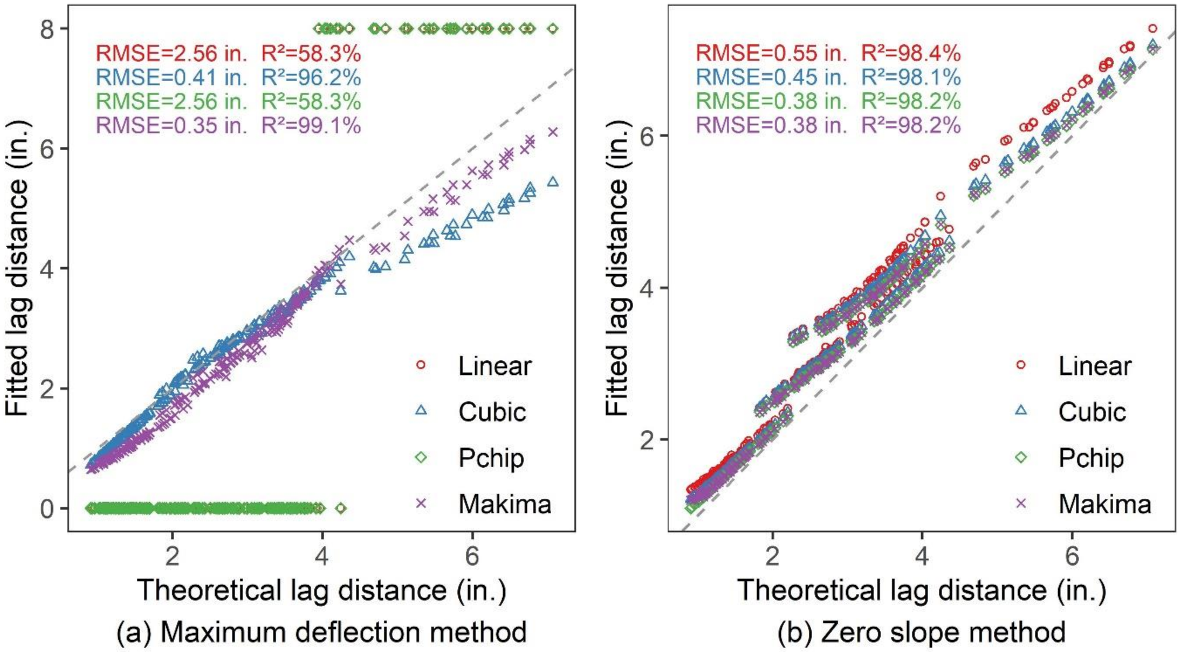

(a) Maximum deflection method

(b) Zero slope method

Figure 4-8. The lag distance calculation: (a) maximum deflection method; (b) zero slope method

Table 4-1. Pavement structures parameters

Levels	Thickness (in.)		Modulus (ksi)		
	AC	Base	AC	Base	Subgrade
Level 1	12	12	-	45	30
Level 2	8	9	-	30	15
Level 3	4	6	-	15	5

CHAPTER 5

RELATIONSHIP BETWEEN FATIGUE CONDITION OF ASPHALT PAVEMENTS AND DEFLECTION LAG FROM TRAFFIC SPEED DEFLECTOMETER (TSD)

A version of this chapter was recently submitted for possible publication by Miaomiao Zhang, Guozhi Fu, Xiaoyang Jia, Yuetan Ma, Pawel Polazyk, and Baoshan Huang to Journal of Materials in Civil Engineering.

My contributions were conducting the literature review, performing asphalt mixture tests, building numerical simulation models, performing the data analysis, and writing the text in the paper. Dr. Guozhi Fu, Dr. Xiaoyang Jia, Dr. Yuetan Ma, Dr. Pawel Polazyk, and Dr. Baoshan Huang provided ideas, guidance, and comments throughout the research process, and offered editorial assistance with the text.

Abstract

The phase angle is a good indicator of the current fatigue condition of asphalt concrete (AC) layers, but estimating phase angles from drilled core samples is destructive, expensive, and unsuitable for large-scale applications. Similar to the phase angle, a lag between load and response has recently been observed in the deflection basin of the non-destructive traffic speed deflectometer (TSD), i.e., the lag between the loading point and the maximum deflection point, and the deflection lag may be closely related to the phase angle. This study investigated the potential of TSD deflection lag as a non-destructive indicator of pavement fatigue conditions. The relationship between AC phase angle and TSD deflection lag was investigated using the 3D-Move program, and the effects of pavement structure, TSD speed, and test temperature on the deflection lag were also investigated. Field TSD data collected in Tennessee were used to verify the relationship between deflection lag and fatigue cracking. The results show that the lag distance increases uniformly with increasing fatigue levels (phase angles) until fatigue failure occurs. However, the lag distance is also closely related to the asphalt thickness and subgrade modulus; therefore, only the lag distance of pavements with the same structures can be compared to identify the fatigue sections. Overall, the lag distance can be used as an implicit indicator of the fatigue condition of the pavement to predict the initiation and growth of fatigue cracks. Fatigue cracking is expected to occur where the lag distance is relatively large.

Introduction

An accurate assessment of existing pavements provides essential inputs to the developers of maintenance and rehabilitation strategies, thus helping to optimize the use of limited funds. Fatigue cracking is the most common type of flexible pavement distress and usually occurs in the early stages of pavement performance deterioration [1]. Assessment of pavement fatigue conditions is a top priority in periodic pavement condition surveys, and researchers in both industry and academia have devoted significant efforts to this end [2–4].

Under repeated traffic loads and weather conditions, the fatigue condition of asphalt concrete (AC) layers tends to deteriorate with the increase of service age. Fatigue tests have been performed to investigate how the AC characteristics change with loading cycles [5–7]. According to the cyclic fatigue test [8], as specified in AASHTO TP 133-21, the curves of dynamic modulus and phase angle with loading cycles show four characteristic regions: internal heating, micro-crack formation, crack formation, and sample breakdown (in Figure 5-1, all tables and figures are located in the Appendix) [9]. The dynamic modulus decreases continuously with the loading cycles [9]. In contrast, the phase angle increases gradually as the sample is repeatedly loaded. This is due to the increasing cracks and voids in the sample, resulting in an enhanced viscous response of the AC material [10]. When the sample starts to break down, the phase angle reaches a maximum and then begins to drop rapidly [8,11]. The failure cycle is defined as the cycle in which the phase angle drops sharply after a stable increase during cyclic loading. Such a pattern suggests that the phase angle is a good indicator of the current fatigue condition of the AC material.

The same conclusion about the phase angle can be extended to the actual pavement. The newly constructed AC layer has a low phase angle. With repeated loading, the phase angle gradually approaches its maximum value as the fatigue crack increases [10]. After that, the pavement will suffer severe fatigue damage [12]. Therefore, if the phase angle can be measured during the pavement service life, the current and impending pavement conditions can be effectively assessed and predicted [12]. However, the current cyclic fatigue test is performed on the Asphalt Mixture Performance Tester (AMPT), which requires AC samples with a height of 4.33 in [13]. Given that a typical asphalt layer is less than a few inches thick, it is usually impossible to obtain field AC samples of this size from actual pavements. Indirect tensile (IDT) testing of AC samples (with a height of 1.5 or 2 in.) is more suitable for evaluating existing pavements [14]. In addition, the pavement fatigue life is closely related to the maximum horizontal tensile strain of the AC layer [4]. Compared to the vertical phase angle measured by AMPT, the horizontal deformation characteristics in the IDT test are more representative of the fatigue cracking behavior of the AC layer [15,16].

In addition, estimating the phase angle of existing AC layers from drilled core samples is destructive and expensive, making it unsuitable for large-scale applications. The phase angle comes from the time lag between the peaks of stress and strain due to AC viscoelasticity (Figure 5-2(a)). A similar phenomenon of the lag between the load and response has recently been observed in deflection basins measured with the traffic speed deflectometer (TSD) [17]. TSD is a continuous deflection measurement device that evaluates the structural strength of flexible pavements in a non-destructive manner [18]. TSD uses a set of Doppler lasers mounted on a servo-hydraulic beam near the rear axle to measure the pavement deflection velocity at traffic speeds [19]. The deflection velocity is converted to pavement surface deflection by curve fitting and integration [20]. Overall, TSD is a promising device that overcomes the limitations of the falling weight deflectometer (FWD) in terms of interruption disruption and testing inefficiency, and it has been used for network-level pavement structural evaluation [21–23].

Figure 5-2(b) shows that the deflection basin obtained from TSD is asymmetric with a steep leading edge and a shallow trailing edge [10]. There is a lag between the loading point and the maximum deflection point, with the maximum deflection point falling behind the loading point. The viscoelastic nature of the AC layer and the inertial damping of the pavement structure could result in a lag between the time when the TSD crosses over the point and the time when the maximum response occurs [17,22]. Some studies suggested that the lag obtained from the TSD deflection basin is closely related to the phase angle of the AC material [10,12]. Therefore, the deflection lag has the potential to be a non-destructive indicator of pavement fatigue crack occurrence and growth. However, the deflection lag may be affected by the pavement structure, TSD moving speed, and test temperature, which will affect the use of the deflection lag in predicting the AC fatigue condition [10,12]. This study will investigate these challenges.

The objective of this study was to investigate the feasibility of assessing pavement fatigue conditions from TSD deflection lag. To achieve this objective, the relationship between the phase angle and the TSD deflection lag was established based on the finite layer method (through 3D-Move program). In addition, the effects of pavement structure, TSD moving speed, and test temperature on the lag distance were also investigated. Field TSD data collected in Tennessee were used to verify the relationship between deflection lag and fatigue cracking.

Figure 5-3 shows the relationship between the fatigue condition, phase angle, and TSD deflection lag of the asphalt pavement. Based on the AMPT cyclic fatigue test specified in AASHTO TP 133-21, a relationship between AC fatigue condition and phase angle was obtained, i.e., the phase angle increases with increasing AC fatigue conditions before fatigue failure occurs. In the next sections, the relationship between AC phase angle and TSD deflection lag will first be investigated using 3D-Move simulations, and the feasibility of linking TSD deflection lag to AC fatigue conditions will be discussed. After that, the effect of other influencing factors on the deflection lag will be investigated using 3D-Move program simulations, including pavement structures, TSD speeds, and test temperatures. At last, the relationship between fatigue conditions of asphalt pavements and TSD deflection lags will be validated by field TSD measurements collected in Tennessee.

Relationship Between Phase Angle and Lag Distance

The phase angle of AC materials is defined as:

$$\varphi = 2\pi \frac{\Delta t}{T} \tag{1}$$

where φ is the phase angle; Δt is the time lag between peaks of the stress and strain within one cycle; T is the period of the cyclic load. Similarly, the lag angle obtained from the TSD deflection basin can be defined as follows:

$$\varphi' = 2\pi \frac{\Delta t'}{T'} \tag{2}$$

where φ' is the lag angle of the deflection basin; $\Delta t'$ is the time lag when the TSD crosses over the point (loading point) and the time when the maximum response occurs; T' is the period of the deflection basin. Assuming that the TSD speed is constant as it drives through the deflection basin, the Equation (2) can be rewritten as:

$$\varphi' = 2\pi \frac{\Delta l}{L} \tag{3}$$

where φ' is the lag angle of the deflection basin; Δl is the lag distance, i.e., the distance between the loading point and the location where the maximum deflection occurs; L is the total length of the deflection basin, i.e., the length that defines the extent of the pavement surface affected by the TSD loading.

Equation (3) shows that the lag angle of the deflection basin is related not only to the lag distance but also to the total length of the deflection basin. However, the latter is very difficult to estimate accurately in practice. The farthest sensor on the TSD is normally located 60 inches from the loading center, which is far from the end of the deflection basin (typically more than 138 inches). Calculating the length of the deflection basin implies the use of the fitted curve that is beyond the range of the observed data, which has a high degree of uncertainty. Therefore, to avoid introducing additional errors in the lag calculation, only the lag distance was considered in this study.

TSD deflections of different phase angles

The relationship between the lag in the TSD deflection basin and the phase angle of the AC layer was investigated by numerical simulation methods. In this study, the 3D-Move program was used to simulate pavement responses under TSD loading. The accuracy of the 3D-Move program has been verified in many studies with field data [17,22]. The Fourier transform technology and frequency domain solutions adopted in the 3D-Move program allows the direct use of the frequency swept data, including the rate-dependent dynamic modulus and rate-dependent phase angles, making it ideal for studying the behavior of viscoelastic AC materials [24].

Assuming a three-layer pavement structure as shown in Table 5-1, the AC layer was defined as a viscoelastic material. The AC viscoelasticity is represented by the rate-dependent dynamic modulus, shown as curve Level 1 in Figure 5-4. The moving speed was 40mph, and the test temperature was 20°C. To investigate the effect of phase angle on TSD deflections, TSD models with four constant phase angles of 15, 25, 35, and 45 degrees were developed. The constant phase angle is represented by a constant damping ratio in the 3D-Move program. The damping ratio (ζ_{AC}) of the AC layer can be estimated from the phase angle (φ) by the following form [17]:

$$\zeta_{\mathrm{AC}} = 0.5\tan(\varphi) \tag{6}$$

Similar to the AC phase angle, the AC damping ratio increases gradually with increasing AC fatigue conditions until fatigue failure occurs.

Figure 5-5 shows the theoretical deflection curves for different AC phase angles. It can be found that the TSD deflection is not symmetric with respect to the loading point. The deflection at the loading point (D0) is not the maximum deflection; the maximum deflection occurs behind the loading point. As the phase angle increases, the maximum deflection increases slightly, while D0 decreases slightly. However, the difference between D0 and the maximum deflection is negligible compared to D0. In addition, the lag distance increases with the increase of the phase angle.

Lag distance calculation

To calculate the lag distance of the TSD deflection basin, the curve fitting method based on the Modified Akima piecewise cubic Hermite interpolation was used [25]. The 3D-Move program outputs pavement surface deflections at 1024 points with an interval of approximately 0.26 inches. Therefore, the theoretical deflection curve was fitted to the 1024 data points. Based on the fitted deflection curve, the location of the maximum deflection point, which is the lag distance, can be determined.

Error! Reference source not found. shows the lag distances of the TSD deflection curves for different phase angles. It can be found that the lag distance increases almost linearly with the increase of phase angle (R^2 of 99.9% for the linear regression). A linear increase means that the lag distance increases uniformly with the phase angles, without inflection or turning points, so the lag distance has the potential to be a non-destructive indicator of the phase angle of the AC layer.

The phase angle reflects the fatigue condition of the AC layer, and the lag distance is closely related to the phase angle. Therefore, the lag distance may be a simple and practical indicator to quantify the AC fatigue condition. The lag distance increases uniformly with increasing fatigue levels (phase angles).

Factors Influencing Lag Distance

The use of the lag distance may help to assess the fatigue condition of the AC layer and allow for more accurate decisions on pavement maintenance and rehabilitation treatments. However, the lag distance may be influenced by factors besides the phase angle, which may affect the assessment of AC fatigue conditions. In this study, the effects of pavement structure, TSD moving speed, and test temperature were investigated using numerical simulations.

Pavement structure

To study the effect of pavement structure on the lag distance, TSD models of various pavement structures were developed using the 3D-Move program. In order to cover as many pavement structures as possible, a total of 243 different three-layer pavement structures were considered, including three plant-produced asphalt concrete (AC) materials, three base moduli, three subgrade moduli, three AC thicknesses, and three base thicknesses, as shown in Table 5-3. Dynamic modulus curves of the three AC materials considered in this study at the reference temperature (20 °C) are shown in Figure 5-4. The AC phase angle was set to an identical constant of 26.57 degrees for all pavement structures to exclude the effect of phase angle. The TSD speed was 40 mph, and the test temperature was 20 °C.

Based on the 3D-Move simulation results, the lag distances were calculated for 243 different pavement structures. The results show that different pavement structures show different lag distances even at the same AC phase angle. The importance of different pavement structure parameters on the lag distance was ranked using the random forest (RF) method, as shown in Figure 5-6(a). It can be found that the AC thickness is the most important factor affecting the lag distance, and subgrade modulus also contributes significantly. The effect of the granular base layer on the lag distance is negligible.

Figure 5-6(b) shows the boxplot of the lag distance grouped by AC thickness and subgrade modulus. The boxplot displays the distribution and skewness of continuous variables through data quartiles, including the minimum, first quartile, median, third quartile, and maximum. As the AC thickness increases, the lag distance also increases. In addition, soft subgrades will lead to larger lag distances. Therefore, the lag distance is related to the pavement structure, and the lag distances of pavements with different structures cannot be directly compared to identify the fatigue sections. For the same pavement structure, it is possible to identify the fatigued section by comparing the lag distance.

It is important to quantify the effect of different pavement structure parameters on the lag distance so that the fatigue level (by lag distance) of different pavement structure segments can be compared. However, there is a large overlap of lag distances between different groups, so it is difficult to isolate the effects of different factors. In the present study, some attempts were made in this regard.

AC thickness

In Figure 5-6(b), the lag distance seems to increase uniformly with the increase of the AC thickness. Assuming that a parameter lag_{ac} is:

$$lag_{ac} = \frac{\Delta l}{h_{ac}} \tag{5}$$

where Δl is the lag distance, in inch; h_{ac} is the thickness of the AC layer, in inch. The lag_{ac} was calculated for different pavement structures. Figure 5-7(a) shows the boxplots of the lag distance and lag_{ac} for different AC thickness groups. The significance of the differences between groups was assessed by the *t*-test. It can be found that there is a significant difference in the lag distance between different AC thickness groups (*p*-values for all *t*-tests were less than 0.01). However, the lag_{ac} is similar for different AC thickness groups (p-value > 0.1). Therefore, by dividing the AC thickness (lag_{ac}), the difference in lag distance caused by AC thickness can be elimiated to a large extent. The results may indicate that the lag distance is proportional to the AC thickness.

$$\Delta l \sim h_{ac} \tag{6}$$

Subgrade modulus

As shown in Figure 5-6(b), the relationship between the lag distance and subgrade modulus is clearly nonlinear. From the preliminary analysis, assuming a parameter lag_{sub} as:

$$lag_{sub} = \Delta l \sqrt[3]{E_{sub}} \tag{7}$$

where Δl is the lag distance, in inch; E_{sub} is the subgrade modulus, in ksi. The lag_{sub} was calculated for different pavement structures. Figure 5-7(b) shows the boxplots of the lag distance and lag_{sub} for different subgrade groups. Similarly, the lag distances are significantly different between the different subgrade groups (p-value < 0.01). However, there is no significant differences in lag_{sub} between different subgrade groups (p-value > 0.1). The difference in lag distances caused by subgrade modulus can be greatly elimiated by lag_{sub}. It may suggest that the lag distance is inversely proportional to the cube root of the subgrade modulus:

$$\Delta l \sim \frac{1}{\sqrt[3]{E_{sub}}} \tag{8}$$

Constant AC modulus

Figure 5-6(a) shows that the type of AC material has little effect on the lag distance, probably because the dynamic modulus curves of the three plant-produced AC materials used in the simulation are similar. To investigate more closely the effect of AC modulus on the lag distance, TSD models with different constant AC modulus were developed based on the pavement structure in Table 5-1. For the rate-dependent AC modulus, it is difficult to determine the exact frequency and equivalent AC modulus to be used. Therefore, the constant AC modulus was used to quantify its effect on the lag distance.

Six constant AC modulus were considered, including 800, 1000, 1200, 1400, 1600, 2000, and 3000ksi, and their lag distances are shown in Figure 5-8. The lag distance increases with increasing AC modulus. It is clear that the lag distance increases nonlinearly with the increase of AC modulus (the R^2 of the linear regression is 96.7%). However, the relationship between the lag distance and the cube root of the AC modulus is basically linear (R^2 of 99.7%). This may indicate that the lag distance is linearly related to the cube root of the AC modulus.

$$\Delta l \sim \sqrt[3]{E_{ac}} \tag{9}$$

where Δl is the lag distance, in inch; E_{ac} is the AC modulus, in ksi.

Equivalent thickness

According to Equations (6)-(9), the lag distance is linearly related to the AC thickness and the cube root of the AC modulus, while inversely proportional to the cube root of the subgrade modulus. The following equation can be obtained:

$$\Delta l \sim h_{ac} \sqrt[3]{\frac{E_{ac}}{E_{sub}}} \tag{10}$$

where Δl is the lag distance, in inch; h_{ac} is the AC thickness, in inch. E_{ac} and E_{sub} are modulus of the AC layer and subgrade, in psi.

The Mechanistic-Empirical Pavement Design Guide proposed a similar equation to calculate the equivalent thickness of the AC layer [4]. According to the "method of equivalent thickness (MET)" established by Odemark, the AC layer can be equivalent to a transformed layer with the subgrade modulus, as shown in Figure 5-9. The thickness of the transformed section is given by an equivalent thickness, h_e, with the following form:

$$h_e = h_{ac} \sqrt[3]{\frac{E_{ac}}{E_{sub}}} \tag{11}$$

The stress distribution for a typical subgrade soil is assumed to be at 45 degree [4]. Therefore, the horizontal extension of the stress distribution in the middle of the AC layer is also h_e.

With the introduction of the equivalent thickness, Equation (10) can be rewritten as:

$$\Delta l \sim h_e \tag{12}$$

The effects of AC thickness, AC modulus, and subgrade modulus can be integrated into a single factor, i.e., the effective thickness. Equation (12) suggests that the lag distance is closely related to the equivalent thickness of the AC layer. It should be noted that the equivalent thickness is introduced to quantify the effect of pavement structure parameters on the lag distance, for which further research is needed.

TSD speed

To evaluate the sensitivity of the lag distance to TSD speeds, 3D-Move models with different TSD speeds were developed based on the three-layer pavement structure presented in Table 5-1. The viscoelasticity of the AC layer was characterized by the rate-dependent modulus and rate-dependent phase angle (AC characteristics Type I). The test temperature was 20 °C. Six TSD speeds were considered, and their lag distances are shown in Table 5-4.

For normal TSD operating speeds (10-60mph), higher TSD speeds (loading frequency) correspond to smaller AC phase angles and are expected to have smaller lag distances. However, Table 5-4 shows that the lag distance increases with increasing TSD speed. This can be explained by the fact that the TSD speed (loading frequency) affects not only the phase angle but also the AC modulus, which is also related to the lag distance. To verify this, TSD models with AC characteristics Type II (rate-dependent modulus and constant phase angle) and Type III (constant modulus and constant phase angle) were developed. The constant AC modulus (988ksi) and constant phase angle (26.57 degrees) are chosen randomly because it is difficult to estimate their equivalent values accurately.

It can be found that for AC with constant modulus and constant phase angle (Type III), the lag distance is almost independent of the TSD speed. For AC with rate-dependent modulus and constant phase angle (Type II), the AC modulus increases with increasing TSD speeds (loading frequency), and therefore the lag distance increases. For AC with rate-dependent modulus and rate-dependent phase angle (Type I), as the TSD speed increases, the weakening effect of the decreasing phase angle on the lag distance is offset by the gaining effect of the increasing modulus, and the lag distance increases slightly. Therefore, compared to the speed-induced phase angle change, the lag distance is more sensitive to the speed-induced modulus change.

Deng et al. also found that the lag distance increased with increasing speeds, and the moving speed showed a significant effect on the lag distance due to the assumption of the constant phase angle [10]. However, considering the more realistic rate-dependent phase angle (AC characteristics Type I), the difference in the lag distance is insignificant, i.e., the lag distance is not sensitive to the variation in TSD speeds. Therefore, during TSD deflection collection, TSD speed variations would not greatly affect the use of lag distance to assess the fatigue condition of the AC layer.

Test temperature

To evaluate the effect of test temperature on the TSD lag distance, 3D-Move models with different test temperatures were developed based on the assumed pavement structure in Table 5-1. The test speed was 40mph. The AC characteristics with temperature-dependent modulus and temperature-dependent phase angle were used in the 3D-Move simulation, and the lag distance of different temperatures is shown in Table 5-5. According to the time-temperature superposition principle, the effects of test temperature and test speed (time) on pavement responses are equivalent. The phase angle of the AC layer increases as the test temperature increases (within 0-30°C), while the modulus decreases. The lag distance is more sensitive to temperature-induced modulus changes; therefore, the lag distance decreases with the increase in temperature.

The lag distance varies more at different test temperatures than at different TSD speeds, so the lag distance is more sensitive to the test temperature than the TSD speed. In addition, the variation of the lag distance is greater at lower temperatures (below 10°C) than at higher temperatures (greater than 20°C). Therefore, in order to minimize the lag distance difference caused by the test temperature variation, it is recommended to perform the TSD test in the warm season.

Field Lag Distance Evaluation

Based on field TSD measurements collected from in-service pavements in Tennessee, lag distances were calculated for various pavement structures and conditions. Field TSD slopes were collected using the TSD device operated by the Australian Road Research Council (ARRB) Group Inc. TSD slopes were measured at ten points (Doppler sensors are mounted at -18, -12, -8, 5, 8, 12, 18, 24, 36, and 60 inches in front of the load center), and lag distances were calculated by curve-fitting and interpolation. In addition to the interpolation error, the testing error of the TSD device is not negligible, especially when the TSD slope measurement is small. Therefore, in this study, the lag distance was calculated only for pavement sections with high TSD slopes, i.e., S5 (slope at 5 inches in front of the load center) is greater than 100μm/m.

The percentage of fatigue crack area is usually used to reflect the fatigue condition of the pavement, and it can be divided into different levels to reflect the different stages of fatigue crack development. Wang et al. considered 3.6% as the cut-off point between the slow and rapid growth of fatigue cracking [26]. FHWA defines pavements with less than 5% fatigue cracks as good condition and those with more than 20% fatigue cracks as poor condition [27]. In this study, fatigue crack development was divided into four stages: no crack (0), early (0-5%), intermediate (5%-20%), and late (>20%), corresponding to pavement fatigue conditions of crack-free, good, fair, and poor, respectively.

Figure 5-10 shows the lag distances for the field TSD routes (including all field pavement structures). Since the lag distance is greatly affected by the pavement structure, pavement sections of different structures cannot be directly compared. Therefore, Figure 5-10 only provides an overview of the relationship between the field lag distance and pavement fatigue cracking. It can be found that the lag distance is the smallest for pavements without fatigue cracks. The lag distance increases gradually with increasing fatigue crack area (early-stage) and reaches a peak at the intermediate stage of crack development (5%-20%). Thereafter, the lag distance decreases as the fatigue crack area increases until fatigue failure occurs (late-stage). Note that under repeated loading, the lag distance shows the same pattern as the phase angle (Figure 5-1). The four fatigue crack development stages: no crack, early, intermediate, and late, can be associated with the four characteristic regions of the phase angle, corresponding to the internal heating, micro-crack formation, crack formation, and breakdown, respectively.

However, in Figure 5-10, the lag distances within each fatigue level vary considerably due to the inclusion of different pavement structures. In addition, there is a large overlap in the lag distances for different fatigue levels. Due to the great influence of the pavement structure, the lag distances for different pavement segments with unknown structures are not comparable. Figure 5-11 shows the comparison of lag distances for different locations on the same road (assuming the same pavement structure). It can be found that for some road sections in Tennessee, the fatigue crack area is closely related to the lag distance. Although there are occasional differences, in general, the lag distance and fatigue crack area always follow the same trend.

The area of fatigue cracks does not always coincide with the lag distance. This can be explained as fatigue cracks explicitly reflect the fatigue condition of asphalt pavements, while the lag distance is an implicit indicator of the pavement fatigue condition. For example, some road sections show only a small amount of fatigue cracks, but with a large lag distance. In this case, it can be assumed that fatigue distress has already occurred in the AC material and more fatigue cracks are expected to appear soon. In Figure 5-12, road SR-457-27 shows a small number of fatigue cracks (less than 3%), and the larger the lag distance, the more fatigue cracks there are. Similarly, on SR-372_92, fatigue cracking seems to follow the trend of lag distance, i.e., a few cracks start to appear at locations with relatively large lag distances. Therefore, the lag distance can be used to predict the initiation and growth of fatigue cracks. For pavements that are currently crack-free (SR-183_66, SR-366_27, SR-5_57), fatigue cracks are expected to initiate at locations with relatively large lag distances.

Therefore, the lag distance can be used as an advance warning of pavement deterioration. The proposed lag distance method is complementary to the traditional fatigue cracking assessment for evaluating pavement fatigue conditions. In addition, the lag distance is a potential use of TSD measurements, whose main purpose is to non-destructively assess the pavement structural condition. Therefore, the use of the lag distance allows taking full advantage of TSD measurements without additional costs.

Conclusion

The phase angle, derived from the time lag between the peaks of stress and strain due to AC viscoelasticity, is considered a good indicator of the current fatigue condition of AC materials (the phase angle increases gradually with increasing fatigue levels until fatigue failure occurs). However, estimating the phase angle of existing AC layers from drilled core samples is destructive, expensive, and unsuitable for large-scale applications. Recently, a similar phenomenon of the lag between load and response has been observed in TSD deflection basins. This study investigated the potential of TSD deflection lag as a non-destructive indicator of pavement fatigue conditions. In addition to phase angle, the effects of other factors on the lag distance were investigated, including pavement structure, TSD moving speed, and test temperature. Field TSD data were used to verify the correlation between lag distance and fatigue cracking. Based on the analyses presented, the following conclusions are drawn:

- The lag distance increases almost linearly with the increase of phase angle (R^2 of 99.9% for the linear regression). The lag distance increases uniformly with increasing fatigue levels until fatigue failure occurs.
- The lag distance increases as the AC thickness (AC modulus) increases or the subgrade modulus decreases. Therefore, the lag distances of different pavement sections with unknown structures are not comparable.
- The effects of AC thickness, AC modulus, and subgrade modulus can be integrated into a single factor, the effective thickness, and the lag distance is closely related to the equivalent thickness of the AC layer.
- The variation of TSD moving speed has little effect on the lag distance. However, the lag distance is more sensitive to the test temperature. The lag distance varies more at lower temperatures (below 10°C) than at higher temperatures (greater than 20°C). Therefore, it is recommended that TSD testing be performed in the warm seasons.

- The lag distance can be considered as an implicit indicator of the fatigue condition of the pavement to predict the initiation and growth of fatigue cracks. Fatigue cracking is expected to occur at locations with relatively large lag distances.

It should be noted that the proposed lag distance method is still under development. Due to the great influence of the pavement structure, the lag distances for different pavement segments with unknown structures are not comparable. Further investigation is recommended to quantify the effect of different pavement structure parameters on the lag distance in order to compare the fatigue levels (by lag distance) of different pavement structure sections. In addition, the decrease of AC modulus with increasing fatigue levels was not considered in this study, and further investigation is needed.

References

[1] Priest, A. L., & Timm, D. H. (2006). Methodology and calibration of fatigue transfer functions for mechanistic empirical flexible pavement design (No. NCAT Report 06-03).

[2] Moreno-Navarro, F., & Rubio-Gámez, M. C. (2016). A review of fatigue damage in bituminous mixtures: Understanding the phenomenon from a new perspective. Construction and Building Materials, 113, 927-938.

[3] Transportation Officials. (1993). AASHTO Guide for Design of Pavement Structures, 1993 (Vol. 1). Aashto.

[4] ARA (Applied Research Associates), Guide for mechanistic- empirical design of new and rehabilitated pavement structures, Washington, DC: Transportation Research Board of the National Academies., 2004.

[5] Wang, C., Castorena, C., Zhang, J., & Richard Kim, Y. (2015). Unified failure criterion for asphalt binder under cyclic fatigue loading. Road Materials and Pavement Design, 16(sup2), 125-148.

[6] Castelo Branco, V. T., Masad, E., Bhasin, A., & Little, D. N. (2008). Fatigue analysis of asphalt mixtures independent of mode of loading. Transportation Research Record, 2057(1), 149-156.

[7] Gibson, N., & Li, X. (2015). Characterizing cracking of asphalt mixtures with fiber reinforcement: use of cyclic fatigue and direct tension strength tests. Transportation Research Record, 2507(1), 57-66.

[8] Castorena, C., Underwood, B. S., Kim, Y. R., Lee, K., Tran, N. H., & Taylor, A. (2021). Ruggedness and Interlaboratory Studies for Asphalt Mixture Performance Tester (AMPT) Cyclic Fatigue Test: Phase I Report (No. FHWA-HRT-21-057). United States. Federal Highway Administration. Office of Infrastructure Research and Development.

[9] Rowe, G. M., & Bouldin, M. G. (2000, September). Improved techniques to evaluate the fatigue resistance of asphaltic mixtures. In 2nd Eurasphalt & Eurobitume Congress Barcelona (Vol. 2000).

[10] Deng, Y., Luo, X., Gu, F., Zhang, Y., & Lytton, R. L. (2019). 3D simulation of deflection basin of pavements under high-speed moving loads. Construction and Building Materials, 226, 868-878.

[11] Anderson, D. A., Christensen, D. W., & Bahia, H. (1991). Physical properties of asphalt cement and the development of performance-related specifications. Journal of the Association of Asphalt Paving Technologists, 60.

[12] Carlson, P., Storey, B., Poorsartep, M., Stevens, C., Ettelman, B., Lindheimer, T. E., ... & Hurlebaus, S. (2017). Advancing innovative high-speed remote-sensing highway infrastructure assessment using emerging technologies: technical report (No. FHWA/TX-16/0-6869-1). Texas A&M Transportation Institute.

[13] Witczak, M. W. (2002). Simple performance test for superpave mix design (Vol. 465). Transportation Research Board.

[14] Kim, Y. R., Seo, Y., King, M., & Momen, M. (2004). Dynamic modulus testing of asphalt concrete in indirect tension mode. Transportation Research Record, 1891(1), 163-173.

[15] Al-Khateeb, G. G., & Ghuzlan, K. A. (2014). The combined effect of loading frequency, temperature, and stress level on the fatigue life of asphalt paving mixtures using the IDT test configuration. International Journal of Fatigue, 59, 254-261.

[16] Seo, Y., El-Haggan, O., King, M., Joon Lee, S., & Richard Kim, Y. (2007). Air void models for the dynamic modulus, fatigue cracking, and rutting of asphalt concrete. Journal of Materials in Civil Engineering, 19(10), 874-883.

[17] Rada, G. R., Nazarian, S., Visintine, B. A., Siddharthan, R. V., & Thyagarajan, S. (2016). Pavement structural evaluation at the network level (No. FHWA-HRT-15-074). United States. Federal Highway Administration. Office of Infrastructure Research and Development.

[18] Flintsch, G. W., Ferne, B., Diefenderfer, B., Katicha, S., Bryce, J., & Nell, S. (2012). Evaluation of traffic-speed deflectometers. Transportation research record, 2304(1), 37-46.

[19] Flintsch, G., Katicha, S., Bryce, J., Ferne, B., Nell, S., & Diefenderfer, B. (2013). Assessment of continuous pavement deflection measuring technologies (No. SHRP 2 Report S2-R06F-RW-1).

[20] Nasimifar, M., Thyagarajan, S., & Sivaneswaran, N. (2018). Computation of pavement vertical surface deflections from traffic speed deflectometer data: evaluation of current methods. Journal of Transportation Engineering, Part B: Pavements, 144(1), 04018001.

[21] Zhang, M., Gong, H., Jia, X., Jiang, X., Feng, N., & Huang, B. (2022). Determining pavement structural number with traffic speed deflectometer measurements. Transportation Geotechnics, 35, 100774.

[22] Zhang, M., Zhang, J., Gong, H., Jia, X., Xiao, R., Huang, H., & Huang, B. (2022). Numerical investigation of pavement responses under TSD and FWD loading. Construction and Building Materials, 318, 126014.

[23] Elbagalati, O., Mousa, M., Elseifi, M. A., Gaspard, K., & Zhang, Z. (2018). Development of a methodology to backcalculate pavement layer moduli using the traffic speed deflectometer. Canadian Journal of Civil Engineering, 45(5), 377-385.

[24] Siddharthan, R. V., Krishnamenon, N., & Sebaaly, P. E. (2000). Finite-layer approach to pavement response evaluation. Transportation Research Record, 1709(1), 43-49.

[25] Akima, H. (1974). A method of bivariate interpolation and smooth surface fitting based on local procedures. Communications of the ACM, 17(1), 18-20.

[26] Wang, Y., Mahboub, K. C., & Hancher, D. E. (2005). Survival analysis of fatigue cracking for flexible pavements based on long-term pavement performance data. Journal of transportation engineering, 131(8), 608-616.

[27] Grogg, M., Van, T., Rozycki, R., Vaughn, R., Roff, T., Clarke, J., ... & Chang, C. (2018). FHWA Computation Procedure for the Pavement Condition Measures (No. FHWA-HIF-18-022). United States. Federal Highway Administration.

Appendix

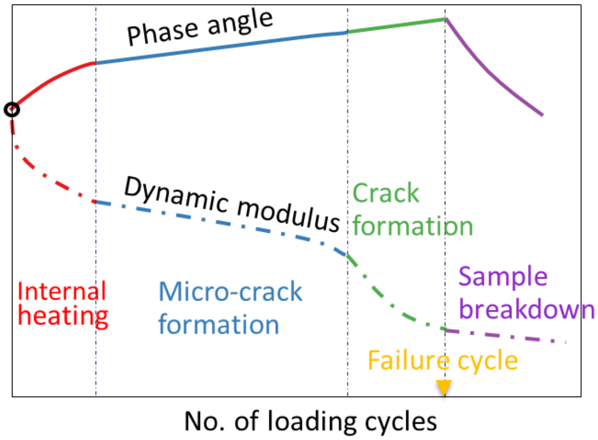

Figure 5-1. AMPT cyclic fatigue test

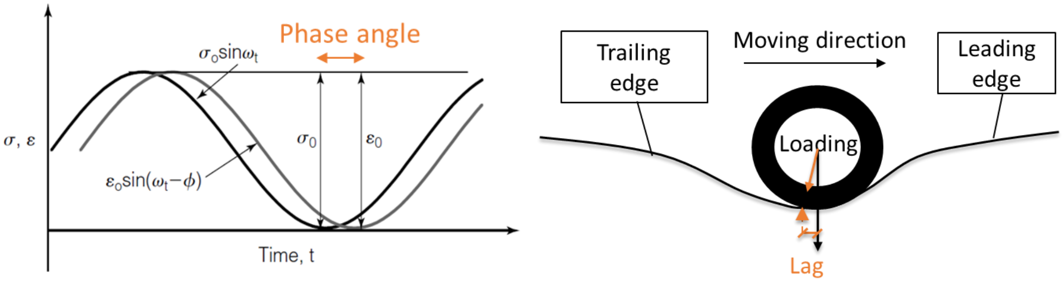

(a) (b)

Figure 5-2. Lag in: (a) phase angle test; (b) in TSD deflection basin

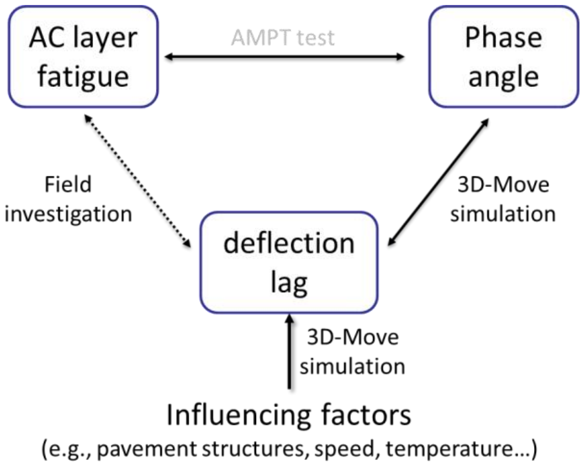

Figure 5-3. Relationship between AC fatigue condition, phase angle and deflection lag

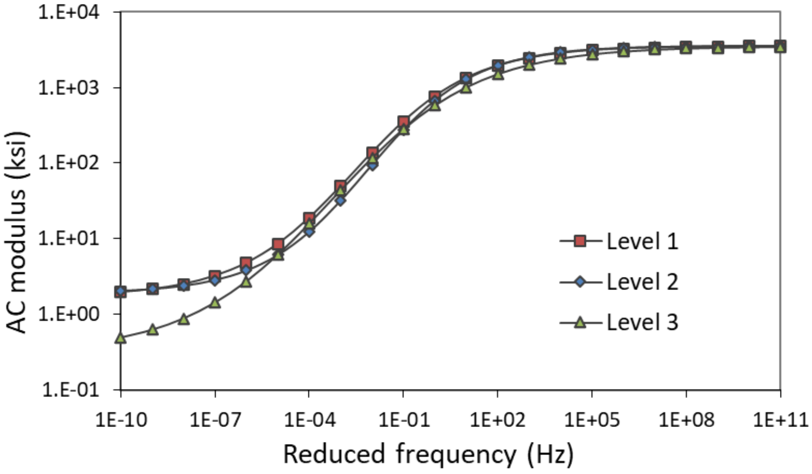

Figure 5-4. Dynamic modulus curves for the three AC materials

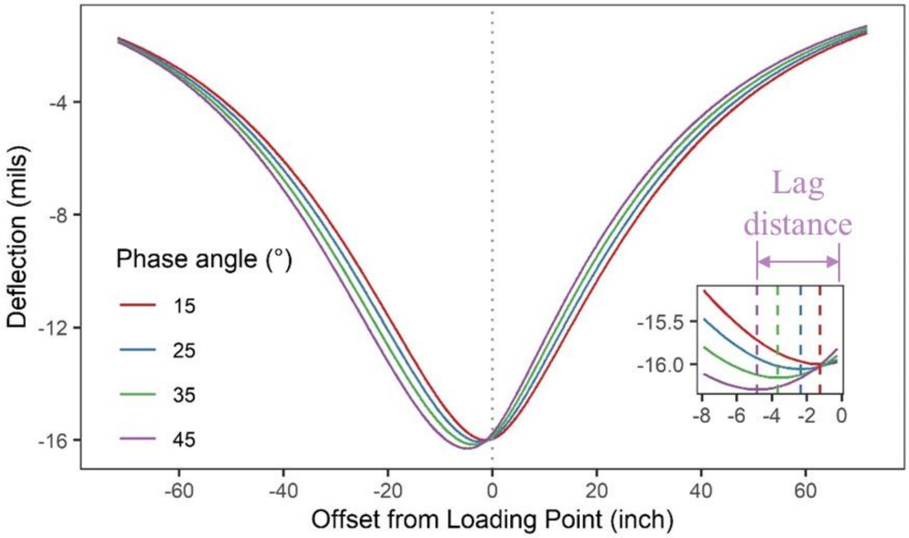

Figure 5-5. TSD deflections of different phase angles

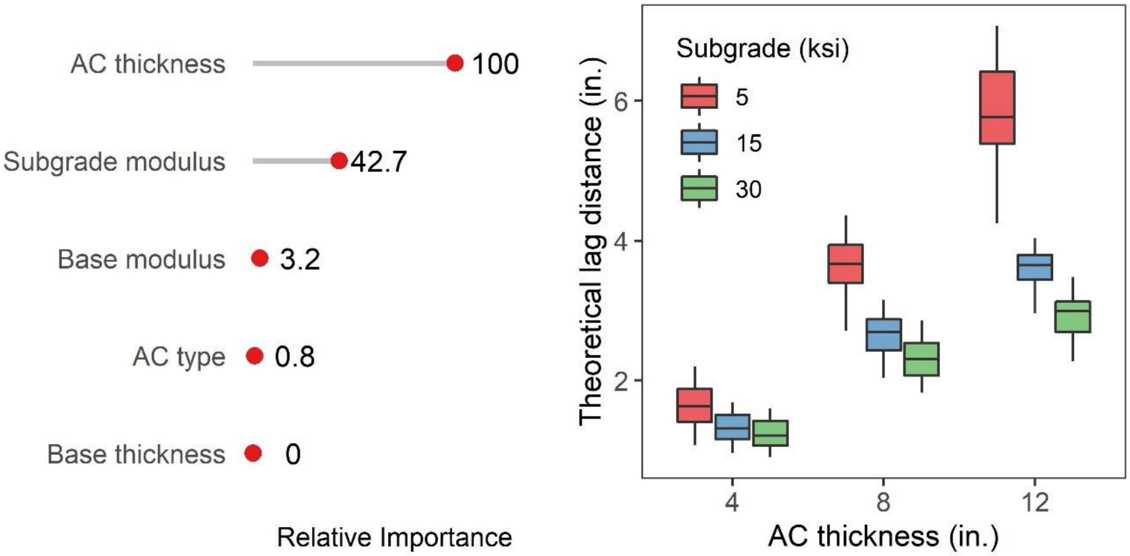

(a) (b)

Figure 5-6. Effect of pavement structure on lag distance: (a)importance ranking; (b) effect of AC thickness and subgrade modulus

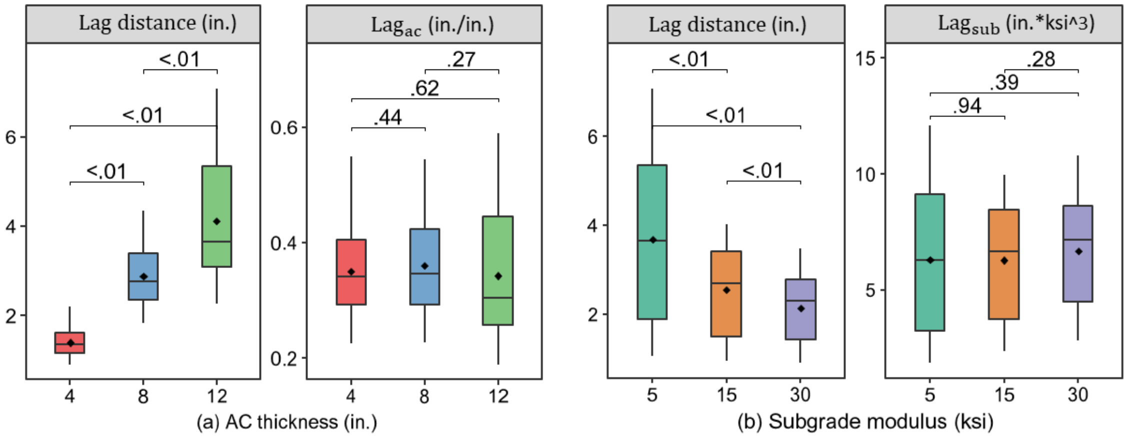

Figure 5-7. Lag distances of different: (a) AC thickness; (b) subgrade modulus

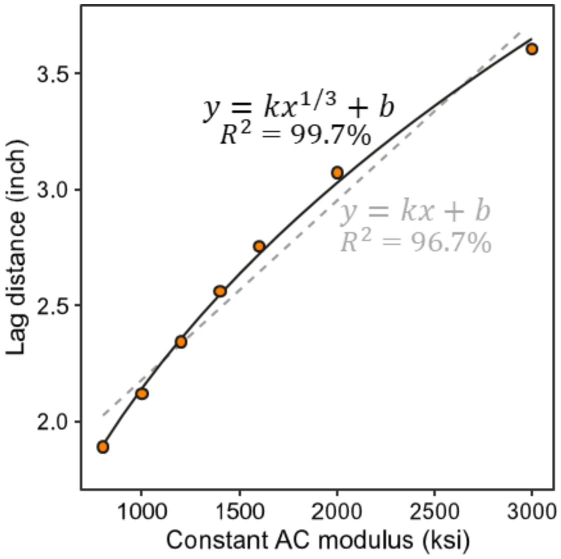

Figure 5-8. Lag distance of different AC modulus

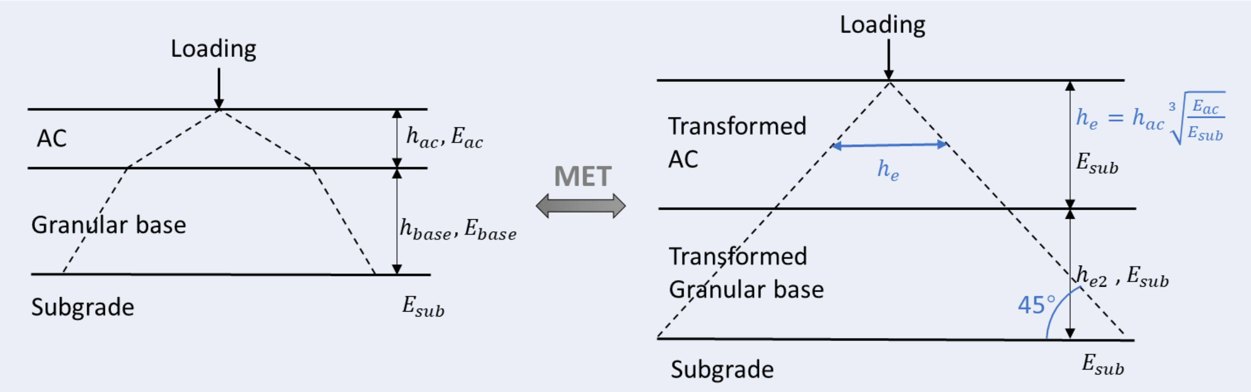

Figure 5-9. Method of equivalent thickness (MET)

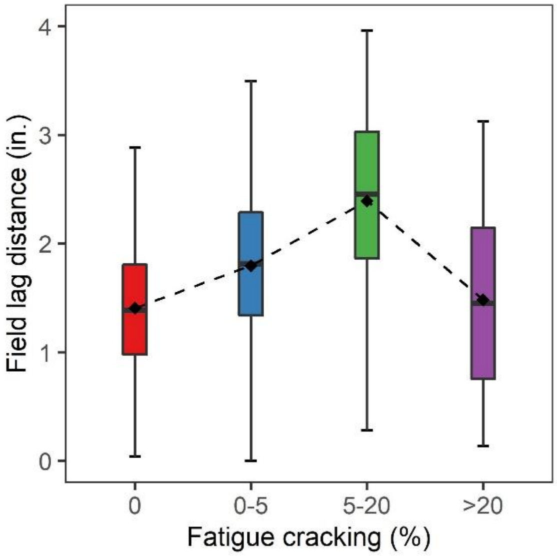

Figure 5-10. Relationship between lag distance and fatigue cracking

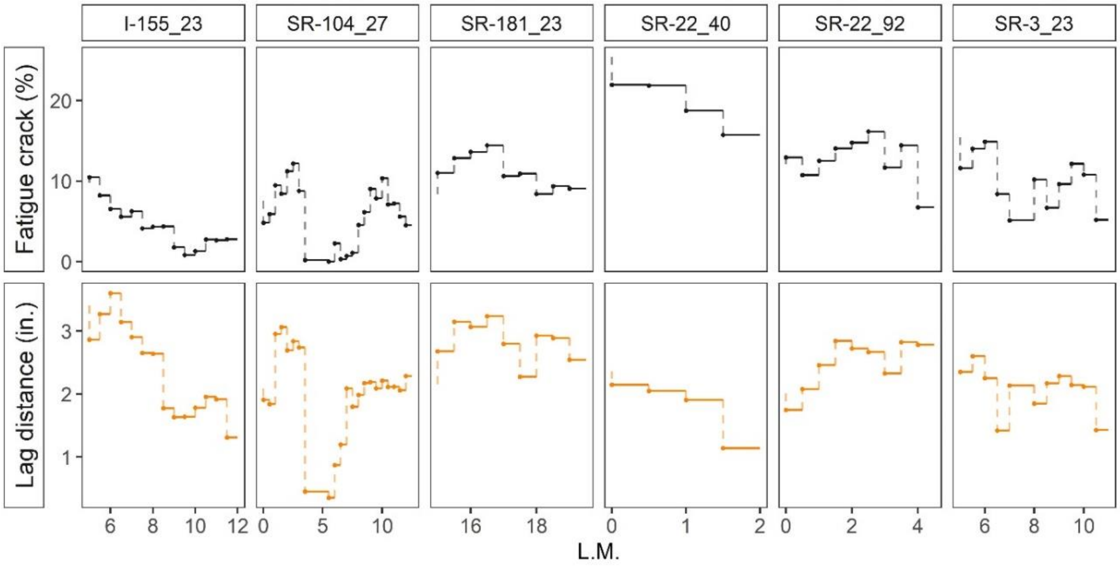

Figure 5-11. Lag distance for cracked pavements

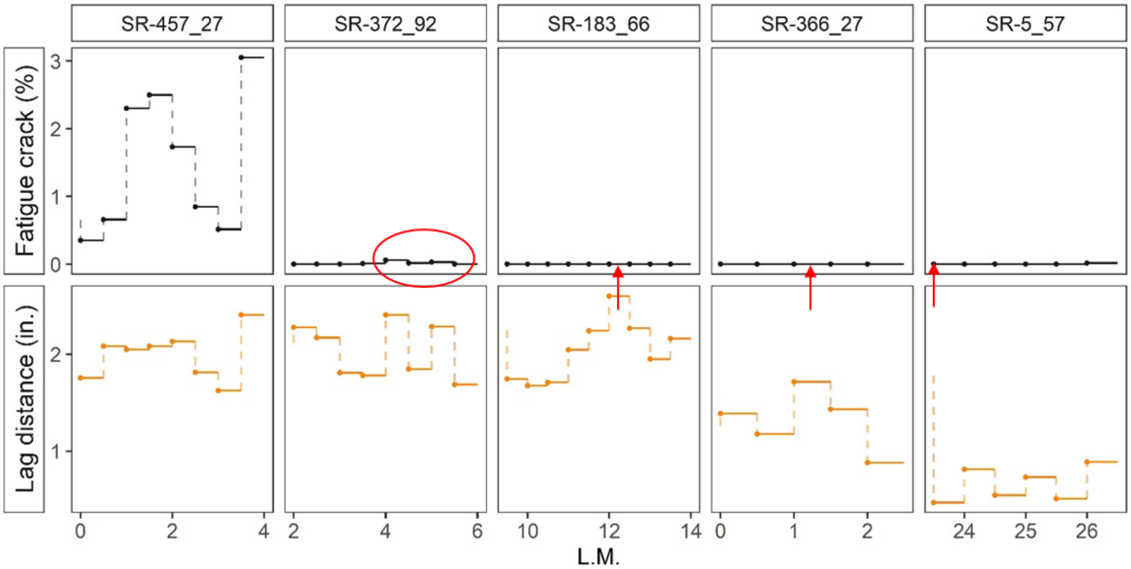

Figure 5-12. Lag distance for crack-free pavements

Table 5-1. Pavement structure design

Layers	Thickness (inch)	Modulus (ksi)	Poisson's ratio
AC	8	-	0.30
Base	9	30	0.35
Subgrade	-	20	0.40

Table 5-2. Lag distance of different phase angles

Phase angle (degree)	15	25	35	45
Lag distance (inch)	1.25	2.36	3.67	4.85

Table 5-3. Different pavement structures in 3D-Move simulations

Levels	Thickness (in.)		Modulus (ksi)		
	AC	Base	AC	Base	Subgrade
Level 1	12	12	-	45	30
Level 2	8	9	-	30	15
Level 3	4	6	-	15	5

Table 5-4. Lag distance at different test speeds

AC characteristics	Type I	Type II	Type III
Modulus	Rate-dependent	Rate-dependent	Constant
Phase angle	Rate-dependent	Constant	Constant
Speed (mph)	Lag distance (inch)	Lag distance (inch)	Lag distance (inch)
10	1.44	2.25	2.10
20	1.46	2.41	2.10
30	1.48	2.51	2.10
40	1.50	2.58	2.10
50	1.51	2.64	2.11
60	1.53	2.68	2.12

Table 5-5. Lag distance at different test temperatures

Test temperature (°C)	0	10	20	30
Lag distance (inch)	1.88	1.61	1.49	1.50

CHAPTER 6

AUTOMATIC CRACK DETECTION AND STRUCTURE CLASSIFICATION USING AUTOENCODER

A version of this chapter is in preparation for possible publication by Miaomiao Zhang, and Baoshan Huang.

My contributions were conducting the literature review, preprocessing image data, developing deep learning models, performing the data analysis, and writing the text in the paper. Dr. Baoshan Huang provided ideas, guidance, and comments throughout the research process, and offered editorial assistance with the text.

Abstract

Currently used crack features are defined based on human experiences (length, area, etc.) and do not adequately reflect pavement crack information, making it difficult to relate pavement cracks to pavement structural conditions. This study proposed a computer-oriented method to extract crack features (called encoded features) from pavement crack images using the autoencoder, thus linking pavement cracks to their structural conditions. The original crack images (128*128 pixels) are compressed into the encoded features (4*4 pixels) by the proposed autoencoder. The encoded features are represented digitally and is difficult for humans to understand, but it retains as much useful information as possible and is therefore a more accurate representation of pavement cracks. On this basis, random forests (RF) classifiers were developed to classify the structural conditions (evaluated by deflection) of different crack images. The RF classifier trained on encoded features outperforms that trained on original images. For crack images with more than 20% cracks, longitudinal cracks on wheel paths play the most important role in the structure classification, and their presence indicates potential pavement structural weakness. However, for crack images with less than 5% cracks, cracks are randomly distributed and contain less structural information. Overall, it is recommended to encode crack features through autoencoders, which is beneficial for both data storage and structure classification.

Introduction

For decades, most pavement surface crack condition evaluations have been conducted manually. Although the highway agencies have realized some drawbacks, such as lower accuracy and lower efficiency [1], they have no or limited choice due to the less advanced data collection devices and the underdeveloped analytical algorithms. Nowadays, computerized technologies have undergone eye-catching advancements [2]. Large amounts of high-quality pavement surface crack image collections have become much easier.

To complement the new data collection techniques, there have been some advances in the analysis algorithms for pavement crack images, but they still fall short of the advances in data collection. The characterization of pavement cracks has evolved from manually counting the number of cracks to extracting crack features through image processing algorithms [3] (Figure 6-1(a)). However, such feature extraction (e.g., crack width, length, and area) is still based on human experiences [4,5]. There are some global or subtle features that cannot be generalized by human experiences, such as the shape and distribution of cracks, but may be important for accurate pavement evaluation. For example, pavement surface cracking should be related to the structural capacity of the pavement; however, some pavements show extensive cracking but are in good structural condition, or vice versa. This may be due to the fact that the currently used crack features (number, area, etc.) do not adequately reflect pavement cracking information. Therefore, new crack image processing and analysis algorithms are needed to be able to retain more crack features.

In fact, there is no need to empirically extract crack features from crack images; the crack images themselves contain all the information about pavement cracks that may have known so far. Those crack features related to the structural condition of the pavement, if any, are hidden in the crack images. However, direct applications of crack images are rarely investigated due to limited data storage (an image typically contains 10k-500k pixels) and underdeveloped analytical algorithms [6]. With the development of computer technology, it has become possible to achieve accurate image dimensionality reduction through deep learning methods, such as the autoencoder [7,8]. The autoencoder is an unsupervised artificial neural network that learns how to efficiently compress the original image to obtain the encoded features [9]. The reconstruction is then performed from the encoded features to make it as close as possible to the original input [9]. Therefore, the encoded features retain as much crack information as possible and can even be used to reconstruct the original crack image, but at a much smaller size.

To some extent, the autoencoder can also be considered a feature extraction method, and the encoded features are the extracted crack features [10]. Instead of extracting crack features based on human experience, the autoencoder is a computer-oriented method, i.e., the encoded features are represented in a digitalized manner and may be difficult for humans to understand (**Error! Reference source not found.**(b)). However, the encoded features retain as much useful information as possible and is therefore a more accurate representation of the crack features. The crack images encoded by the autoencoder may be able to capture crack features that are closely related to the pavement structural condition.

The objective of this study was to develop a computer-oriented method for automatic pavement crack evaluation. The autoencoder was used to reduce the dimensionality of crack images and retain useful crack features (encoded features). Based on the encoded feature, random forest classifiers were developed to classify crack images into strong and weak pavement structures.

Autoencoder Development

Image pre-processing

The pavement crack images used in this study were collected by the Automatic Crack Detection (ACD) system equipped on the intelligent Pavement Assessment Vehicle (iPAVe), which is operated by the Australian Road Research Board (ARRB) [11]. The ACD system consists of two high-performance 3D sensors mounted on the rear of the iPAVe trailer. Each sensor consists of two main components: a high-power spread line laser and a high-speed 3D camera. When combined, the two 3D laser units project a 4-meter-wide laser line on the pavement surface consisting of more than 4,000 measurement points. By combining sequential transverse profiles, an image of the pavement surface can be built up, with only 5 mm between these profiles at 55 mph.

Figure 6-2 shows the pre-processing steps of the crack images. The raw surface image is processed into a crack map by a proprietary Pavemetrics software algorithm [2], and all crack maps are provided by ARRB. By removing the pavement background from the crack map, an image with only cracks can be obtained. The size of the crack image usually varies from road segment to road segment, with an average size of about 600*500 pixels. The crack images were resized to the same size (128*128 pixels) for subsequent programming implementation. The color variation indicates the average width of each crack. In this study, RGB images (3 channels) were converted to binary images (1 channel).

Autoencoder configuration

The proposed autoencoder is inspired by the basic theory of U-net [12–14] with a similar U-shape, as shown in Figure 6-3. Each blue box in the figure represents a multi-channel feature map. The values above the boxes represent the number of kernels. The size of the feature map is also given. The autoencoder can be divided into the encoder (left) and the decoder (right). The pre-processed binary crack images are used as inputs to provide information to the encoder. The encoder extracts the crack features using successive convolutional and pooling layers. For simplicity, fixed convolutional kernel size (3*3) is used to extract multi-level features [15]. The max-pooling operation is selected over the mean pooling based on the consideration that the cracks have the highest contrast with the background (non-crack area) [16]. After five max-pooling operations, the size of the feature map (4*4 pixels) is reduced to $1/32^2$ of the original crack input (128*128 pixels). Neural networks typically get deeper and deeper because more complex and nonlinear relationships can be better learned from deeper neural networks [15,17]. However, the goal of the proposed autoencoder is to reduce the size of the crack images while retaining as much useful information as possible. Therefore, the depth of the proposed autoencoder, i.e., the number of kernels, first increases (from 16 to 32 to 64) and then decreases (from 64 to 32 to 16 to 4 to 1). The output of the encoder (the encoded feature) is the smallest feature map obtained in the encoder part, with a size of 4*4*1.

On the right side, the output of the encoder (the encoded feature) is fed to the decoder. The corresponding five-level transpose convolutions (up-convolutions) are conducted consecutively to restore the size of the encoded features (4*4 pixels) to the original size

(128*128 pixels). The number of kernels in the transpose convolution direction is symmetrical to the encoder. Finally, the reconstructed crack image can be found in the output of the decoder. It should have the same size as the original input [12]. Compared with the original input, the size of the encoded features is greatly reduced after the encoding operation, and the loss of information caused by the smaller size is difficult to be compensated for. Therefore, the reconstructed image should be obviously different from the original input, but still reflects most of the crack features.

In addition, it is noteworthy that there is no concatenate layer in the proposed autoencoder. In the typical U-net, feature maps of the same size in the encoder and decoder are copied and added at each level of up-convolutions, which is called the “concatenate operation” [16]. The concatenate layer facilitates minimizing the backward loss in training because it provides additional useful information beyond the encoded features [18]. With the help of the concatenate layer, the performance of the reconstructed image will be boosted, however, the concatenate layer will also be an essential input to the reconstructed images. Then, the reconstructed image cannot be reconstructed by the encoded features only. It cannot force the encoded features to contain as much useful information as possible, nor can it achieve image dimensionality reduction. Therefore, the proposed autoencoder does not include the concatenate layer.

Autoencoder training

The proposed autoencoder has a total of 253,682 parameters (1,650 parameters are non-trainable), of which 108,529 are for the encoder and 145,153 are for the decoder. A total of 10,304 crack images were used in the autoencoder development, of which 50% were randomly selected as the training data to train the autoencoder, while the rest were kept as the test data. During the training process, 50% of the training data (with replacement) were randomly selected for validation in each epoch. Both the original inputs and the ground truth of the autoencoder are the pre-processed binary crack images. The batch size was 64 and the learning rate was gradually adjusted from 0.01 to 0.0001 during the training process. The binary cross-entropy was employed as the loss function, and the test loss was reduced from 0.8630 to 0.2557 after 745 epochs.

Autoencoder Evaluation

As shown in Figure 6-4, six crack images with different numbers of cracks were randomly selected for encoding and decoding to show the performance of the proposed autoencoder. The original input of the autoencoder is the pre-processed binary crack images. The original inputs (128*128 pixels) are reduced to the encoded features (4*4 pixels) by the encoder, and the encoded features are restored to the reconstructed image (128*128 pixels) by the decoder.

It can be found that the original input and the reconstructed image are roughly similar, and the reconstructed images are able to reflect most of the crack features in the original input. The amount, shape, and distribution of pavement cracks are well reconstructed from the encoded features, so most crack features can be captured by the encoded features. However, due to the greatly reduced dimensionality of the encoded feature, there are still differences between the original input and the reconstructed image; specifically, the autoencoder is good at identifying cracks in the longitudinal direction, while cracks in the transverse direction are difficult to be reconstructed by the proposed autoencoder. This is because longitudinal cracks are often observed in the pavement centerlines and wheel paths, and they are more continuous and can be connected from pixel to pixel, making them easier to compress and store. For cracks in the transverse direction, they are more discontinuous, random, and irregular, making them difficult to compress and reconstruct. For images with a small number of cracks, the over-dominance of longitudinal cracks is more obvious, while for images with a large number of cracks, both longitudinal and transverse cracks can be recognized.

The encoded features are the most important intermediate of the autoencoder, which retains most crack features while having a very small size. However, it is represented digitally and is too abstract to be understood. Figure 6-5 is an attempt to explain the meaning of the encoded feature. As shown in Figure 6-5(a), the 4*4 pixels of the encoded features can be represented by 16 variables, namely X1, X2, …, and X16. In order to figure out what each of the 16 variables refers to, assume that one variable is 1 and the other 15 variables are all 0. These 16 variables (reshaped as 4*4) are then fed to the decoder to obtain the reconstructed plot. The reconstructed plot (128*128 pixels) is easier to understand because it is an approximation of the actual pavement crack image.

Figure 6-5(b) shows the matrix of assumed encoded plots (1 for one variable and 0 for the other 15 variables) corresponding to the 16 variables. Figure 6-5(c) is the corresponding matrix of reconstructed plots obtained from assumed encoded plots, each subplot representing one variable in the encoded feature. The subplot positions in Figure 6-5(a) & (b) & (c) correspond to each other. It can be found that X5, X9, and X13 represent cracks near the left edge of the pavement, while X8, X12, and X16 represent cracks near the right edge of the pavement. X7, X11, and X15 represent longitudinal cracks on the right wheel path, while X10 and X14 represent longitudinal cracks on the left wheel path (near the pavement centerline). Therefore, the encoded feature corresponds well to the actual crack image or the original input. It should be noted that the 16 variables in the encoded features may not be independent but interrelated, so Figure 6-5(c) is only one possible interpretation of the encoded feature.

Structure Classification for Crack Images

The pavement structural condition refers to the ability of the pavement to withstand traffic loads and weather conditions, and it is the underlying reason for pavement surface cracking. Generally, strong pavement structures tend to show few cracks, while weak pavement structures tend to show a large number of cracks. However, the opposite also happens. Some pavements show extensive cracking but are in good structural conditions, or vice versa. Identifying these counter-intuitive pavement sections (widely cracked but structurally sound, less cracked but structurally weak) facilitates more appropriate decisions on maintenance and rehabilitation (M&R) strategies, thereby helping to optimize the use of limited funds.

FHWA defines pavements with less than 5% fatigue cracks as good condition and those with more than 20% fatigue cracks as poor condition [19]. Two random forests (RF) classifiers were developed to classify pavement structures for crack images with more than 20% cracks and for crack images with less than 5% cracks, respectively. The pavement structural condition was assessed by the pavement deflection collected by the traffic speed deflectometer (TSD). In addition to the ACD system, the iPAVe is also equipped with the TSD device so that TSD deflections and pavement crack images can be collected simultaneously [20]. Based on field TSD deflections (and crack images) collected in Tennessee, the pavement structure can be classified into two levels:

- Strong structure: TSD deflection at the loading center is less than 5 mils.
- Weak structure: TSD deflection at the loading center is greater than 20 mils.

Structure classification for crack images with more than 20% cracks

RF classifier development

For crack images with more than 20% cracks, the RF classifier was developed to classify their structural conditions. As shown in Figure 6-6, two different RF classifiers were trained on the original inputs (128*128 pixels) and on the encoded features (4*4 pixels), respectively. There are 2109 crack images with more than 20% cracks, of which 1591 are strong structures and 518 are weak structures. 80% of the crack images were randomly selected as the training dataset, while the remaining 20% were retained as the test dataset. To tune hyperparameters in the RF classifier, the randomized search combined with 3-fold cross-validation was performed for 100 iterations based on the training dataset [21]. **Error! Reference source not found.** shows all hyperparameters considered in this study [22] and the optimized hyperparameters for each RF classifier.

RF classification performance

Table 6-2 shows the performance of each RF classifier evaluated on the test dataset, including accuracy, precision, recall, and F1-score. Considering the imbalance of the dataset, the balanced accuracy is also calculated. It can be found that in terms of accuracy, the RF classifier trained on the encoded features (0.97) performs better than the RF classifier trained on the original inputs (0.93), especially for the balanced accuracy (0.96 vs. 0.87). In addition, the various performance metrics of the RF classifier trained on the encoded features are more balanced and stable. This is because there are 16384 (128*128) predictors in the original input, which increases the difficulties of training the RF classifier. However, the encoded feature has only 16 (4*4) predictors, which makes the training of the RF classifier much easier and with less overfitting. In addition, it is verified from the side that the encoded features can capture most crack patterns in the actual crack images and contains sufficient information about the pavement structural condition. The encoded features are more valuable than the original input because it is smaller in size, contains complete pavement crack and structural information, and can be used to predict pavement structural conditions.

RF variable importance

Variable importance is a key concept in machine learning that refers to the relative importance of each variable in the training data [23]. Determining variable importance is one of the key steps in the machine learning model development pipeline. Using the RF classifier, the variable importance can be measured by the average impurity decrease calculated over all decision trees in the forest, i.e., the Gini index [24]. The variable importance helps to understand which variables are most important to the RF classifier and makes the RF classifier more interpretable.

Figure 6-7(a) and (b) show the relative variable importance of the RF classifier (for crack images with more than 20% cracks) trained on the original inputs and on the encoded features, respectively. From Figure 6-7(a), it can be found that for crack images with more than 20% cracks, longitudinal cracks on the wheel path play the most important role in the structure classification. Cracks at other locations are less important. This may be due to the fact that the wheel path cracks are mainly caused by the traffic load, while cracks at other locations may be caused by other factors, such as temperature variations. Load-induced cracks are more closely related to the pavement structural condition. It should be noted that the TSD's Doppler lasers are mounted on a servo-hydraulic beam near the rear axle (on the centerline of the right dual tire). The TSD measures the pavement deflection on the centerline of the right dual tire. Therefore, in Figure 6-7(a), cracks on the right wheel path seem to be more significant than cracks on the left wheel path, but this may not be the case. Compared to Figure 6-7(a), Figure 6-7(b) is more abstract and less interpretable, because it is obtained from the RF classifier trained on the encoded features. Corresponding to Figure 6-5, it can be found that X15 is the most important variable, representing cracks on the right wheel path. X13 also contributes significantly to the structure classification, representing cracks at the left edge of the pavement (near the left wheel path). The same is true for X9 and X11. Therefore, although it looks different at the first glance, the variable importance of the FR classifier trained on original inputs is essentially the same as that trained on the encoded features. In structural classification, the RF classifier extracts the same information from the original inputs and the encoded features.

Figure 6-8 shows the comparison of strong and weak structures for crack images with more than 20% cracks, and five examples were randomly selected for each category. For strong structures in Figure 6-8(a), no cracks are found on the right wheel path, and X15 in the encoded features are all less than 0.5. For weak structures in Figure 6-8(b), there are many cracks on the wheel path, and X15 in the encoded features are all greater than 0.5. Therefore, cracks on the wheel path (X15 greater than 0.5) indicate potential pavement structure weakness.

Structure classification for crack images with less than 5% cracks

RF classifier development

For crack images with less than 5% cracks, the RF classifier was developed to classify their structural conditions. Similarly, two different RF classifiers were trained from the original inputs (128*128 pixels) and from the encoded features (4*4 pixels), respectively, as shown in Figure 6-9. There are 2311 crack images with less than 5% cracks, of which 590 are strong structures and 1721 are weak structures. 80% of the crack images were randomly selected as the training dataset, while the remaining 20% were retained as the test dataset. To tune hyperparameters in the RF classifier, the randomized search combined with 3-fold cross-validation was performed for 100 iterations based on the training dataset. Table 6-3 shows all hyperparameters considered and the optimized hyperparameters for each RF classifier.

RF classification performance

Table 6-4 shows the testing performance of each RF classifier in terms of accuracy, balanced accuracy, precision, recall, and F1-score. It can be found that although the accuracies are similar (0.83 vs. 0.82), the balanced accuracy of the RF classifier trained on the encoded features (0.74) is higher than that trained on the original inputs (0.69). Similarly, the various performance metrics of the RF classifier trained on the encoded features are more balanced and stable. Therefore, the same conclusion can be drawn that the encoded features rather than the original inputs are recommended for structure classification.

Overall, the classification performance of crack images with less than 5% cracks is not as good as that of crack images with more than 20% cracks. Especially for strong structures, the recalls (and F-1 scores) of both RF classifiers are unsatisfactory, which means that a significant portion of strong structures is misclassified. This may be due to the fact that for crack images with less than 5% cracks, cracks are rather randomly distributed and contain less structural information. Even in the encoded features, only a few crack features are learned.

RF variable importance

Figure 6-10(a) and (b) show the relative variable importance of the RF classifier (for crack images with less than 5% cracks) trained on the original inputs and on the encoded features, respectively. From Figure 6-10(a), it can be found that for crack images with less than 5% cracks, cracks on the wheel path are relatively more important than cracks at other locations, but the importance difference is not significant. The same is true for the encoded features in Figure 6-10(b), where all 16 variables seem to have an equal impact on the structural classification, with X14 (cracks on the left wheel path) and X15 (cracks on the right wheel path) being slightly more important.

Figure 6-11 shows the comparison of strong and weak structures for crack images with less than 5% cracks, and five examples were randomly selected for each category. There is no significant difference between crack images of strong and weak structures.

Conclusion

In this study, a computer-oriented method was developed to extract crack features (encoded features) from pavement crack images using the autoencoder, thus linking pavement cracks to their structural conditions. The original pavement crack images (128*128 pixels) are compressed to the encoded features (4*4 pixels) by the proposed autoencoder. Two RF classifiers were developed to classify pavement structures for crack images with more than 20% cracks and for crack images with less than 5% cracks, respectively. Based on the analyses presented, the following conclusions are drawn:

- The original crack images (128*128 pixels) are compressed to the encoded features (4*4 pixels) by the proposed autoencoder. The encoded features are able to capture most features of pavement cracks (e.g., number, shape, and distribution), while having a very small size.
- Longitudinal cracks on the pavement surface are more regular, while cracks in the transverse direction are more discontinuous, random, and irregular. The autoencoder is more capable of identifying longitudinal cracks than it is of identifying transverse cracks.
- RF classifiers trained on encoded features outperform those trained on original inputs. The huge size of the original input (128*128 pixels) increases the difficulty of training the RF classifier, while the small size of the encoded features reduces the risk of overfitting. The encoded features rather than the original images are recommended for pavement structure classification.
- Some pavements show extensive cracking but are in good structural conditions. For crack images with more than 20% cracks, it contains sufficient structural information so that strong and weak pavement structures can be classified with high accuracy (0.87 for the original input and 0.96 for the encoded feature). Longitudinal

cracks on the wheel path play the most important role in the structure classification, and their presence indicates potential pavement structural weakness.

- Some pavements show few cracks but are in poor structural conditions. For crack images with less than 5% cracks, cracks are randomly distributed and contain less structural information. The accuracy of structure classification is unsatisfactory, with 0.69 for the original input and 0.74 for the encoded feature.

Overall, it is recommended to encode the original crack images without loss of crack information, which is beneficial for both data storage and structure classification.

References

[1] Ragnoli, A., De Blasiis, M. R., & Di Benedetto, A. (2018). Pavement distress detection methods: A review. Infrastructures, 3(4), 58.

[2] Vavrik, W., Evans, L., Sargand, S., & Stefanski, J. (2013). PCR evaluation: considering transition from manual to semi-automated pavement distress collection and analysis.

[3] Wang, W., Wang, M., Li, H., Zhao, H., Wang, K., He, C., ... & Chen, J. (2019). Pavement crack image acquisition methods and crack extraction algorithms: A review. Journal of Traffic and Transportation Engineering (English Edition), 6(6), 535-556.

[4] Lins, R. G., & Givigi, S. N. (2016). Automatic crack detection and measurement based on image analysis. IEEE Transactions on Instrumentation and Measurement, 65(3), 583-590.

[5] Hoang, N. D., & Nguyen, Q. L. (2019). A novel method for asphalt pavement crack classification based on image processing and machine learning. Engineering with Computers, 35(2), 487-498.

[6] Indyk, P., & Motwani, R. (1998, May). Approximate nearest neighbors: towards removing the curse of dimensionality. In Proceedings of the thirtieth annual ACM symposium on Theory of computing (pp. 604-613).

[7] Petscharnig, S., Lux, M., & Chatzichristofis, S. (2017, June). Dimensionality reduction for image features using deep learning and autoencoders. In Proceedings of the 15th international workshop on content-based multimedia indexing (pp. 1-6).

[8] Yang, Y., Wu, Q. J., & Wang, Y. (2016). Autoencoder with invertible functions for dimension reduction and image reconstruction. IEEE Transactions on Systems, Man, and Cybernetics: Systems, 48(7), 1065-1079.

[9] Rumelhart, D. E., Hinton, G. E., & Williams, R. J. (1985). Learning internal representations by error propagation. California Univ San Diego La Jolla Inst for Cognitive Science.

[10] Meng, Q., Catchpoole, D., Skillicom, D., & Kennedy, P. J. (2017, May). Relational autoencoder for feature extraction. In 2017 International Joint Conference on Neural Networks (IJCNN) (pp. 364-371). IEEE.

[11] ARRB Group Inc. Road Survey Equipment. ARRB Systems n.d. https://arrbsystems.com/ (accessed October 9, 2022).

[12] Ronneberger, O., Fischer, P., & Brox, T. (2015, October). U-net: Convolutional networks for biomedical image segmentation. In International Conference on Medical image computing and computer-assisted intervention (pp. 234-241). Springer, Cham.

[13] Zhou, Z., Rahman Siddiquee, M. M., Tajbakhsh, N., & Liang, J. (2018). Unet++: A nested u-net architecture for medical image segmentation. In Deep learning in medical image analysis and multimodal learning for clinical decision support (pp. 3-11). Springer, Cham.

[14] Huang, H., Lin, L., Tong, R., Hu, H., Zhang, Q., Iwamoto, Y., ... & Wu, J. (2020, May). Unet 3+: A full-scale connected unet for medical image segmentation. In ICASSP 2020-2020 IEEE International Conference on Acoustics, Speech and Signal Processing (ICASSP) (pp. 1055-1059). IEEE.

[15] Simonyan, K., & Zisserman, A. (2014). Very deep convolutional networks for large-scale image recognition. arXiv preprint arXiv:1409.1556.

[16] Huyan, J., Li, W., Tighe, S., Xu, Z., & Zhai, J. (2020). CrackU‐net: A novel deep convolutional neural network for pixelwise pavement crack detection. Structural Control and Health Monitoring, 27(8), e2551.

[17] Szegedy, C., Liu, W., Jia, Y., Sermanet, P., Reed, S., Anguelov, D., ... & Rabinovich, A. (2015). Going deeper with convolutions. In Proceedings of the IEEE conference on computer vision and pattern recognition (pp. 1-9).

[18] Zou, Q., Zhang, Z., Li, Q., Qi, X., Wang, Q., & Wang, S. (2018). Deepcrack: Learning hierarchical convolutional features for crack detection. IEEE Transactions on Image Processing, 28(3), 1498-1512.

[19] Grogg, M., Van, T., Rozycki, R., Vaughn, R., Roff, T., Clarke, J., ... & Chang, C. (2018). FHWA Computation Procedure for the Pavement Condition Measures (No. FHWA-HIF-18-022). United States. Federal Highway Administration.

[20] Zhang, M., Zhang, J., Gong, H., Jia, X., Xiao, R., Huang, H., & Huang, B. (2022). Numerical investigation of pavement responses under TSD and FWD loading. Construction and Building Materials, 318, 126014.

[21] Breiman, L. (2001). Random forests. Machine learning, 45(1), 5-32.

[22] Probst, P., Wright, M. N., & Boulesteix, A. L. (2019). Hyperparameters and tuning strategies for random forest. Wiley Interdisciplinary Reviews: data mining and knowledge discovery, 9(3), e1301.

[23] Strobl, C., Boulesteix, A. L., Kneib, T., Augustin, T., & Zeileis, A. (2008). Conditional variable importance for random forests. BMC bioinformatics, 9(1), 1-11.

[24] Nembrini, S., König, I. R., & Wright, M. N. (2018). The revival of the Gini importance. Bioinformatics, 34(21), 3711-3718.

Appendix

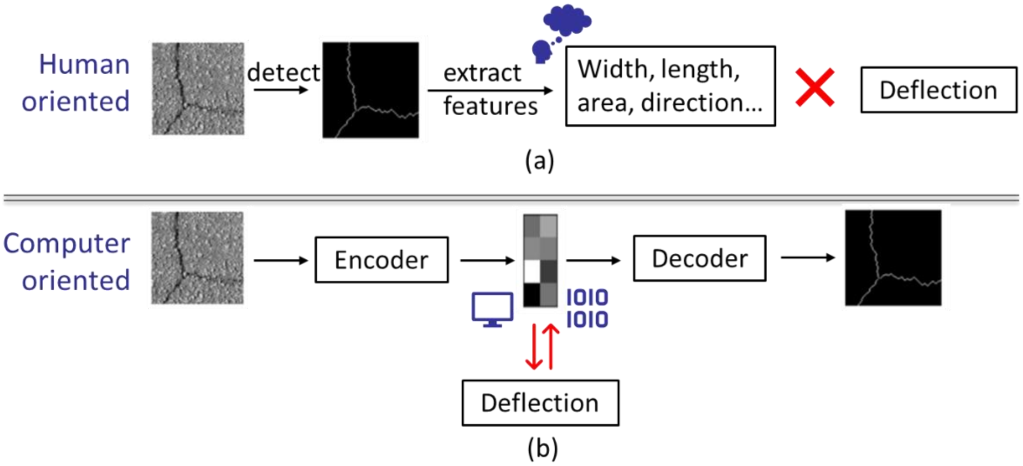

Figure 6-1. Pavement crack evaluation: (a) human-oriented; (b) computer-oriented

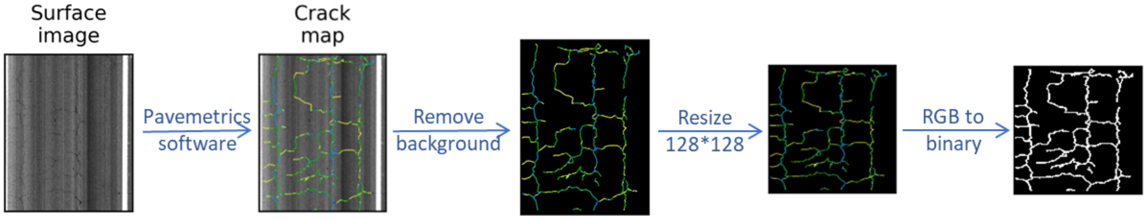

Figure 6-2. Crack image pre-processing

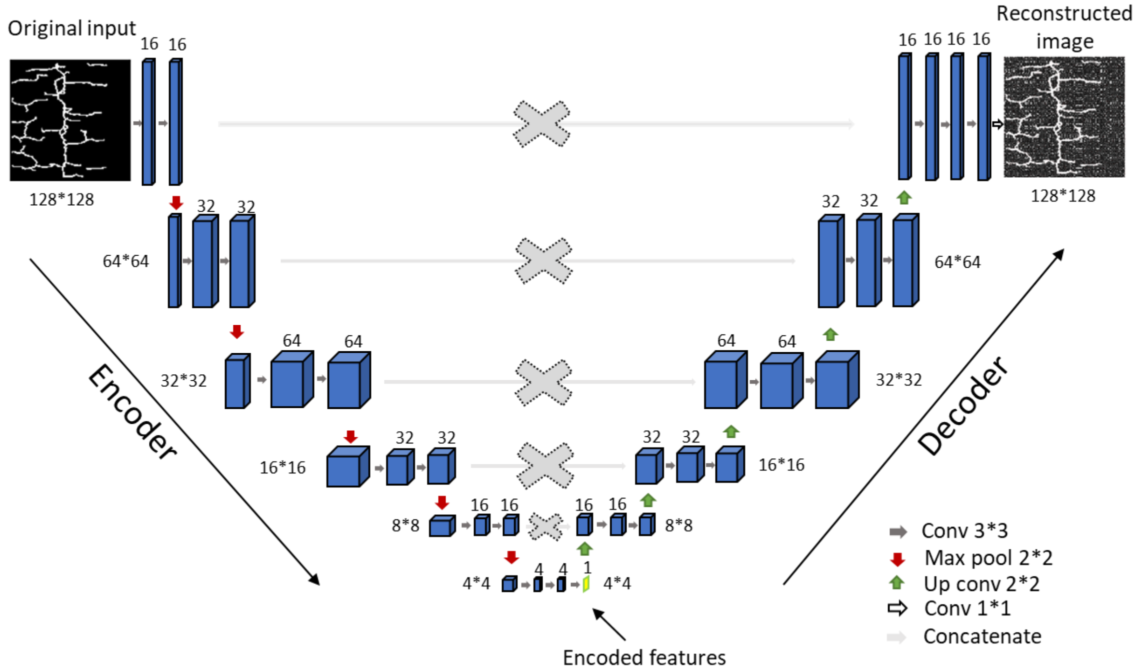

Figure 6-3. Autoencoder architecture

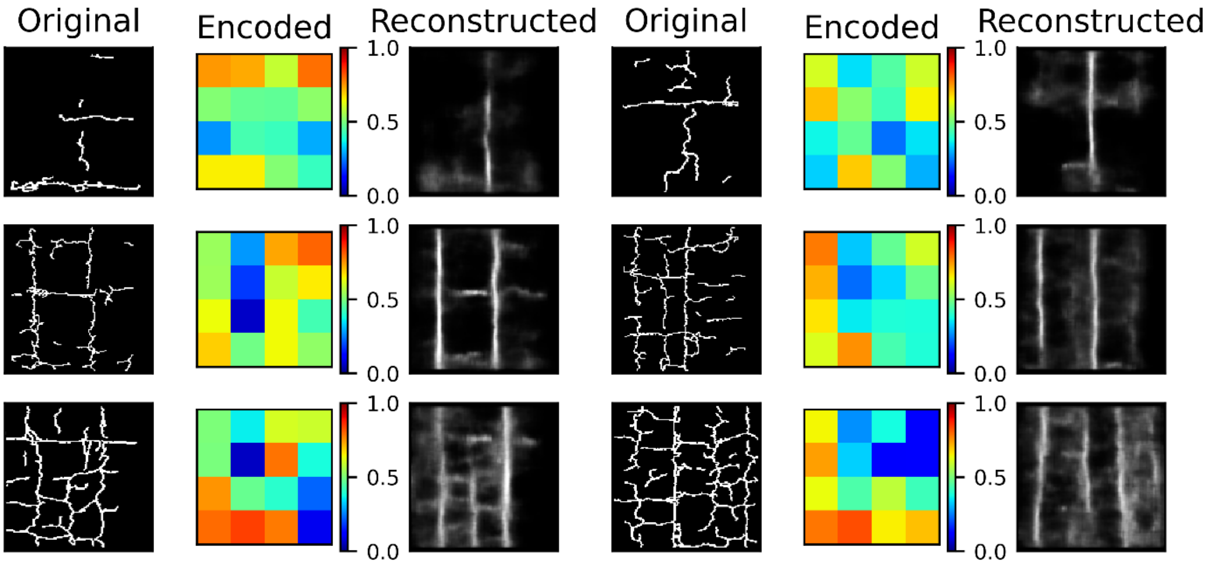

Figure 6-4. Examples of autoencoder evaluation

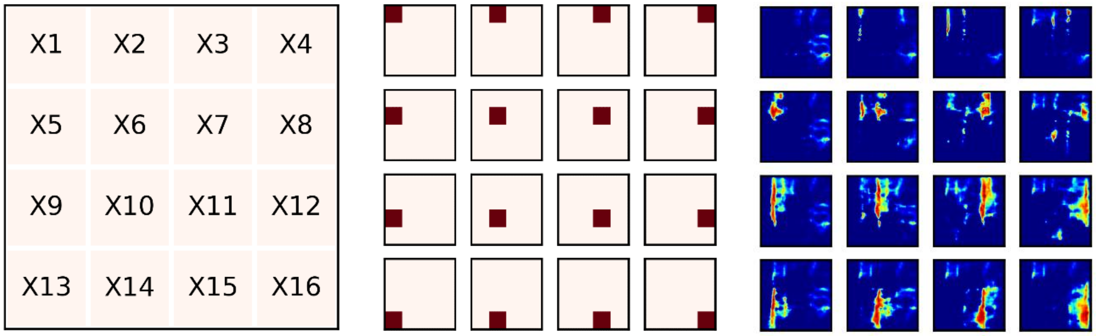

(a) (b) (c)

Figure 6-5. Encoded features: (a) schematic diagram; (b) assumed encoded plots; (c) corresponding reconstructed plots

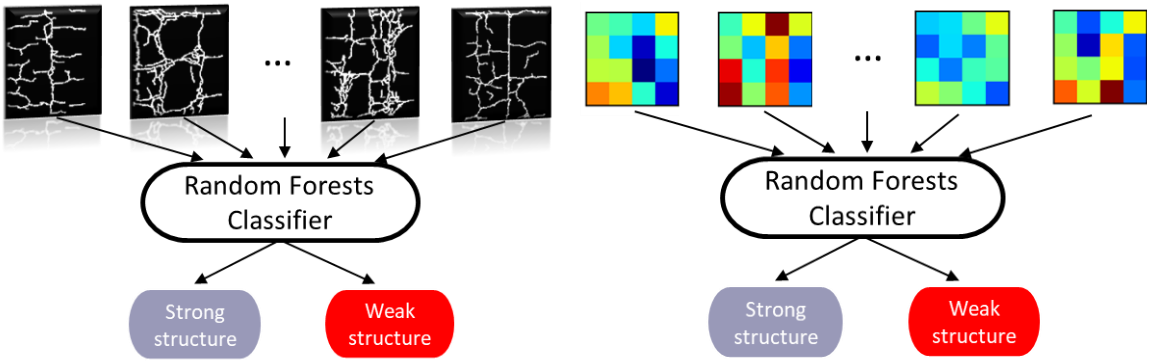

(a) (b)

Figure 6-6. Structure classification of cracks more than 20%: (a) original inputs (128*128 pixels); (b) encoded features (4*4 pixels)

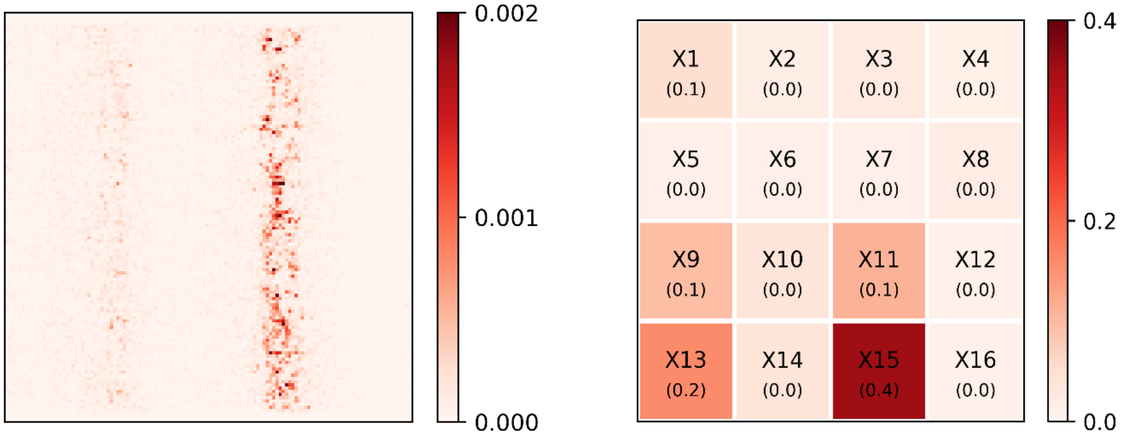

(a) (b)

Figure 6-7. Variable importance of RF classifiers for cracks more than 20%: (a) original inputs (128*128); (b) encoded features (4*4)

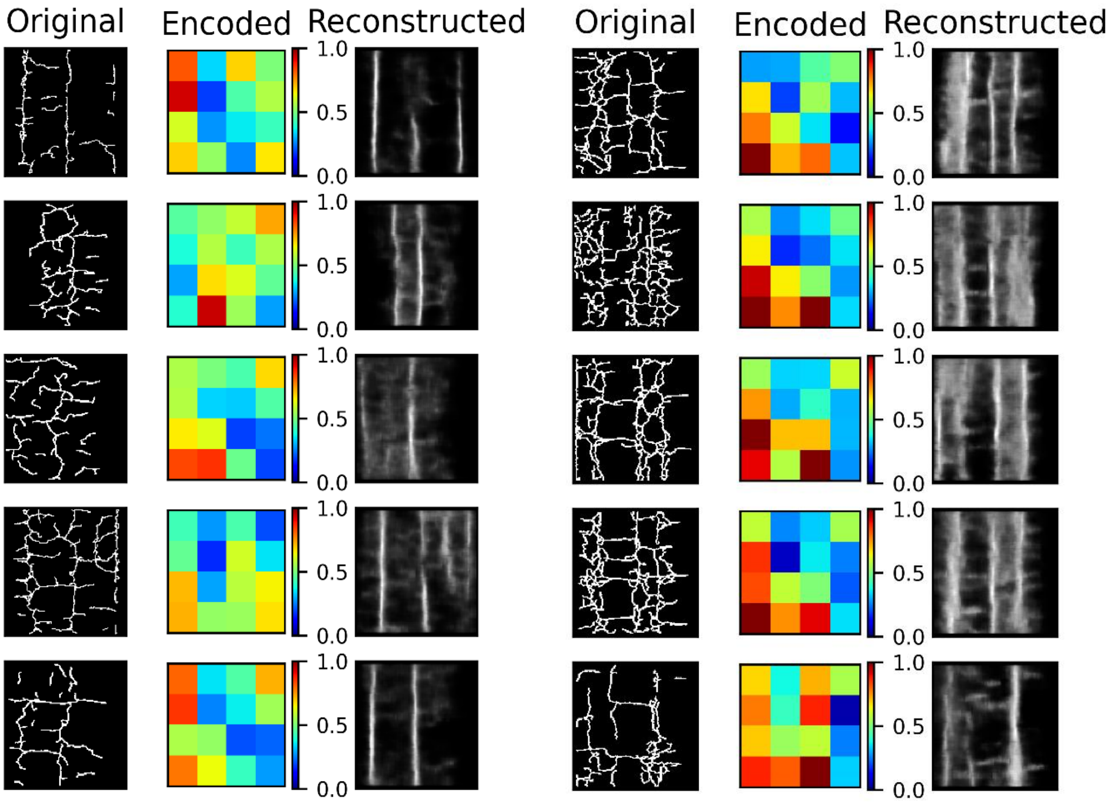

(a) (b)

Figure 6-8. Cracks more than 20%: (a) strong structure; (b) weak structure

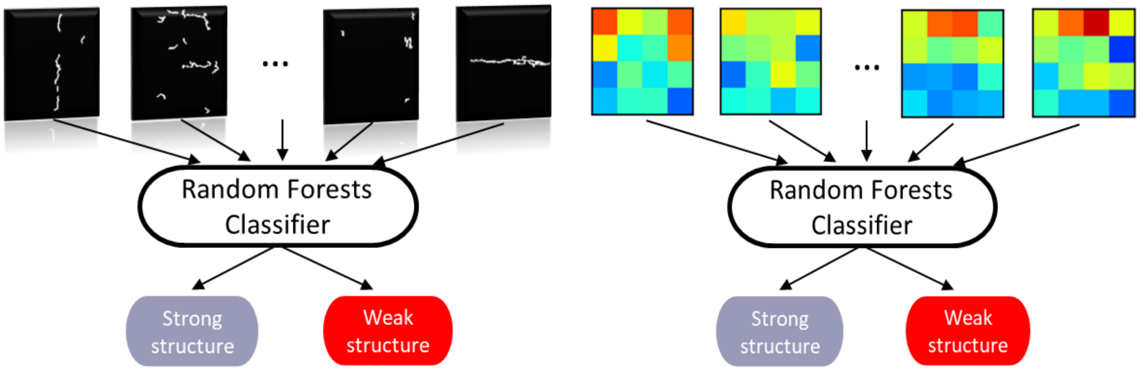

(a) (b)

Figure 6-9. Structure classification of cracks more than 20%: (a) original inputs (128*128 pixels); (b) encoded features (4*4 pixels)

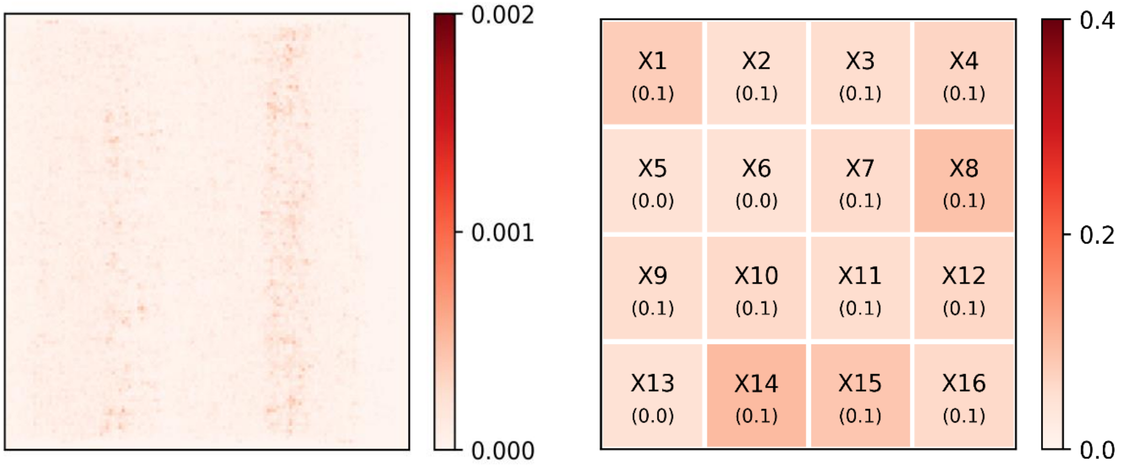

(a) (b)

Figure 6-10. Variable importance of RF classifier for cracks less than 5%: (a) original inputs (128*128); (b) encoded features (4*4)

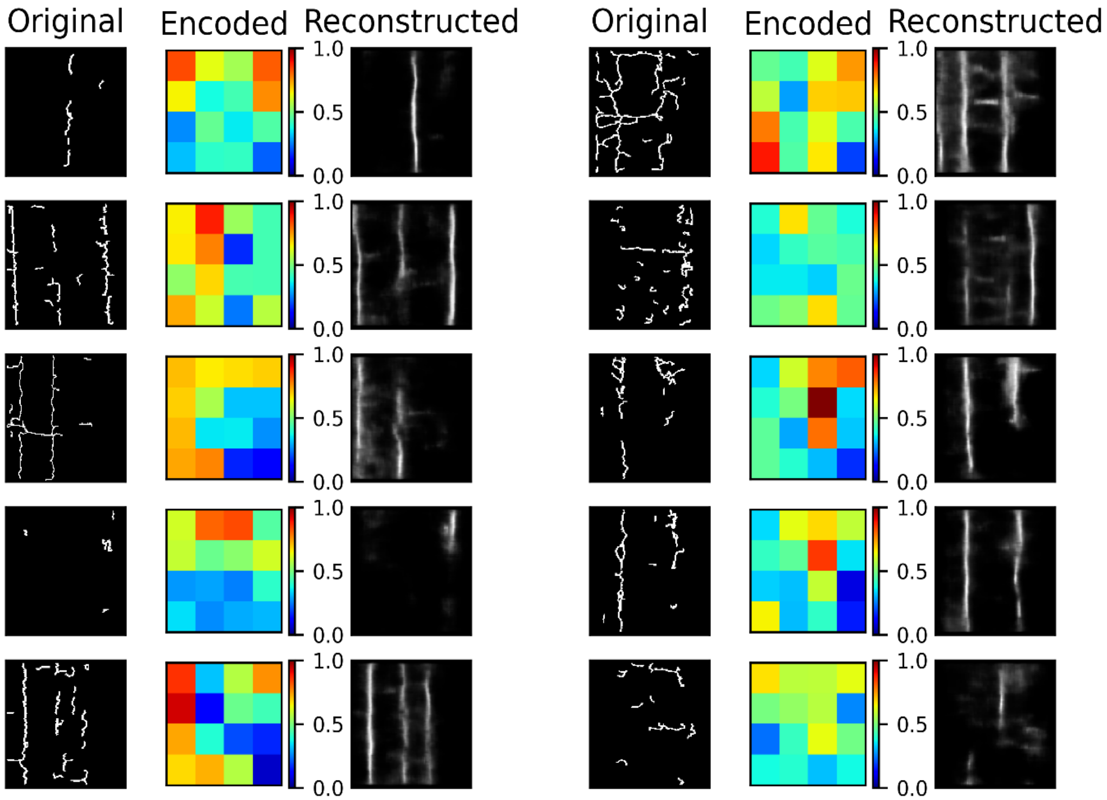

(a) (b)

Figure 6-11. Cracks less than 5%: (a) strong structure; (b) weak structure

Table 6-1. Hyperparameters of RF classifiers for cracks more than 20%

Hyperparameter	Description	Possible values	Optimized values	
			Original inputs (128*128 pixels)	Encoded features (4*4 pixels)
n_estimators	number of trees	50-500	300	250
max_depth	maximum depth of a tree	100-500	260	460
max_features	number of features for split	[log2, sqrt]	sqrt	sqrt

Table 6-2. Performance of RF classifiers for cracks more than 20%

Performance metrics	Original inputs (128*128 pixels)		Encoded features (4*4 pixels)	
	strong structure	weak structure	strong structure	weak structure
Precision	0.92	0.99	0.98	0.96
Recall	1	0.73	0.99	0.92
F-1 score	0.96	0.84	0.98	0.94
Accuracy	0.93		0.97	
Balanced accuracy	0.87		0.96	

Table 6-3. Hyperparameters of RF classifiers for cracks less than 5%

Hyperparameter	Description	Possible values	Optimized values	
			Original inputs (128*128 pixels)	Encoded features (4*4 pixels)
n_estimators	number of trees	50-500	350	300
max_depth	maximum depth of a tree	100-500	500	200
max_features	number of features for split	[log2, sqrt]	log2	log2

Table 6-4. Performance of RF classifiers for cracks less than 5%

Performance metrics	Original inputs (128*128 pixels)		Encoded features (4*4 pixels)	
	strong structure	weak structure	strong structure	weak structure
Precision	0.93	0.80	0.82	0.83
Recall	0.38	0.99	0.52	0.95
F-1 score	0.54	0.89	0.64	0.89
Accuracy	0.82		0.83	
Balanced accuracy	0.69		0.74	

CHAPTER 7

CONCLUSION

Conclusions

The proposed doctoral study investigated the application of TSD deflection in network-level pavement evaluation, and five tasks were included: 1) developed a speed correction method for TSD deflections based on the time and temperature superposition principle; 2) developed a new approach to determine the pavement SN with TSD measurements by modifying the FWD-based AASHTO procedure; 3) explored the potential use of TSD slopes in pavement evaluation, including replacing deflection index, estimating the inflection point location, and calculating the deflection lag distance; 4) investigated the feasibility of assessing pavement fatigue conditions from TSD deflection lag; 5) developed a computer-oriented method for automatic pavement crack detection and structure classification from pavement crack images. The following is a summary of the major findings:

- The effects of speed (loading time) and temperature on TSD deflections are equivalent, so the speed effect on pavement responses can be evaluated by the concept of “pseudo temperature”. TSD deflection is more sensitive to temperature than speed. At normal TSD driving speeds (20-60 mph), a 10 mph increase in speed is approximately equivalent to a 1°C decrease in temperature.
- The loading frequency of a TSD is lower than that of an FWD, and the AC layer exhibits lower stiffness under a TSD. The TSD-based AASHTO SN is generally smaller than the FWD-based SN (error of 0.74). The TSD-based SN can be calibrated by AC thickness.
- Deflection is not directly related to the AC thickness. The introduction of SCI_12 is a good complement to the deflection and can help to identify weak AC layers. However, the deflection slope correlates well with the AC thickness. The TSD slope itself can be used to identify weak asphalt layers and subgrades without introducing additional indices. S5 and S60 (slopes at 5 inches and 60 inches in front of the load center) are recommended to indicate the strength of the asphalt layer and subgrade, respectively.

- The lag distance increases with increasing fatigue levels until fatigue failure occurs. The lag distance is also related to pavement structures, temperature, and speed. For the same pavement structure, it is possible to identify the fatigued section by comparing the lag distance. Fatigue cracking is expected to occur at locations with relatively large lag distances.
- It is recommended to encode the original crack images without loss of crack information, which is beneficial for both data storage and structure classification. For crack images with more than 20% cracks, longitudinal cracks on the wheel path play the most important role in the structure classification, and their presence indicates potential pavement structural weakness.

VITA

Miaomiao Zhang was born in 1993 in Shanxi, China. She initiated her academic studies with a major in civil engineering at Dalian University of Technology, in Liaoning, China, in 2011, where she attained her bachelor's degree in Civil Engineering in 2015. She also acquired her master's degree in the same university starting from 2015 to 2018. She began her studies at the University of Tennessee, Knoxville in 2019 as a Ph.D. student. She will attain her Doctor of Philosophy in Civil Engineering with a focus in Civil Engineering in December 2022. During her time in the University of Tennessee, Knoxville, she extended her research into pavement evaluation using the traffic speed deflectometers and the application of numerical simulation models and machine learning algorithms to solve pavement engineering related problems.